ORNL-3392
UC-20 – Controlled Thermonuclear Processes

THERMONUCLEAR DIVISION

SEMIANNUAL PROGRESS REPORT

FOR PERIOD ENDING OCTOBER 31, 1962

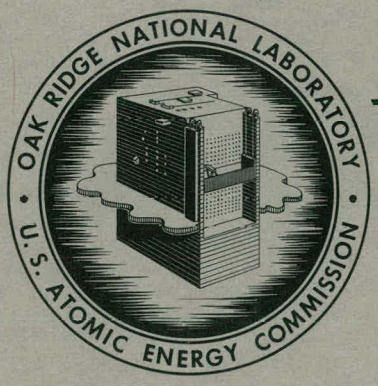

OAK RIDGE NATIONAL LABORATORY
operated by
UNION CARBIDE CORPORATION
for the
U.S. ATOMIC ENERGY COMMISSION

DISCLAIMER

Printed in USA. Price: $2.25 Available from the
Office of Technical Services
U. S. Department of Commerce
Washington 25, D. C.

ORNL-3392
UC-20 – Controlled Thermonuclear Processes

Contract No. W-7405-eng-26

THERMONUCLEAR DIVISION

SEMIANNUAL PROGRESS REPORT

For Period Ending October 31, 1962

DATE ISSUED

MAR 4 – 1963

OAK RIDGE NATIONAL LABORATORY
Oak Ridge, Tennessee
operated by
UNION CARBIDE CORPORATION
for the
U. S. ATOMIC ENERGY COMMISSION

THIS PAGE

WAS INTENTIONALLY

LEFT BLANK

Contents

THIS PAGE

WAS INTENTIONALLY

LEFT BLANK

Introduction

A. H. Snell

The electron-cyclotron heating experiment leapt into prominence during the past summer, when the emission of neutrons was observed when deuterium was fed into the plasma. Foils were activated. The neutron emission was found to be correlated with a regime which was narrowly defined by gas-feed and magnetic-field adjustments, and which was stable as seen by various detectors, x-ray bursts being absent. The story of the episode is told in Sec 3.1.1, which describes rather difficult measurements of the neutron energy that indicated that most of the neutrons do not come from D-D reactions (which was really too much to be hoped for), but can be accounted for on the basis of electrodisintegration of the deuteron. The neutron yield accordingly indicates the presence of electrons of more than 2.2 Mev, in a density of about $10^9/cm^3$. Since the *e*-D cross-section curve has not appeared explicitly in the literature, it was evaluated as part of the investigation, and is given in Sec 6.5. The high beta indicated by diamagnetic measurements (see our last report) still appears valid, so what we apparently have is a steady-state, electron-hot, high-beta plasma that is *stable*. The heating of the ions has to be left as a further exercise, with the question of the maintenance of stability in larger size and in the presence of the hot ions left to be answered by experiment.

The continued high level of performance of the DCX-1 apparatus has permitted a great deal of further productive work, with emphasis on the correlation of rf signals, neutral-particle emission, slow plasma emission through the magnetic mirrors, energy degradation of the stored protons, plasma potential, and plasma decay time. All of this has permitted our understanding of the phenomena of DCX-1 to gain a coherence that it has lacked in the past. The reader should refer to Chap. 1 for details, but a hint of the nature of the processes may be given here. There are various conditions of operation for DCX-1, but one of special interest pertains to the low-pressure range of $\sim 3 \times 10^{-9}$ torr. Under such conditions the proton-cyclotron rf signal often occurs in sharp, separated, regularly spaced bursts, suggesting a relaxation process under which the ions in the storage ring temporarily cluster, and then disperse. The indications are that the process that produces the clustering also transfers energy from the stored protons to electrons; some of the electrons escape endwise, the plasma potential rises, and since some of the protons are degraded in energy, they become more susceptible to charge-exchange loss and accordingly neutralize themselves. It still seems clear that the fast protons are not thrown out directly by the instability.

In our last report we discussed the spreading of the stored proton population in DCX-1, stating that unless the spreading could be controlled, the conditions for exponentiation looked remote. We have now empirically found a way to control the spreading (Sec 1.4). The process is at present only imperfectly understood in terms of an increase in disorder as the result of precessions; it is limited by the operating range of DCX-1, and has to be studied further before we can say whether or not exponentiation has again come within range.

DCX-2 has had further operating experience, the most notable observation being that it so far has been only modestly successful in storing protons. There is apparently a loss of protons from the central region of DCX-2 while the H_2^+ beam is being injected; when injection is stopped, one sees a proton population mainly at the ends, with disappointingly little in the central region of the apparatus. Needless to say this matter is

under intensive investigation; our experience with this device is still young.

Experiments have continued on the confinement of low-energy plasma between magnetic mirrors, with the realization that ion cooling plays an important part in the interplay between charge exchange and scattering into the escape cone (Secs 3.2–3.5). A Snooperscope has been found to be rather readily adaptable for "stroboscopic" visual observation of rapid plasma phenomena (Sec 3.6). Steady-state carbon-arc studies have been continued with measurement, by Doppler broadening, of the temperature reached by ions produced in the arc by cold gas feed; thus He^+ reached 10^6 °K, while N^{2+} and A^{2+}, for example, appear to come into equilibrium with the C^{2+} ions at 2.5×10^6 °K.

The Theory Group was expanded during summer activities, and they have contributed several notes of interest to this report. In Sec 6.1, the suggestion is made that a spread in cyclotron resonance frequencies (as might be expected in the presence of a nonuniform magnetic field or of a mixture of e/m values) would help to suppress the cyclotron (Harris) instabilities at high particle densities. The rather general treatment of stability in terms of Lyapunov functions has been pursued, as summarized in Sec 6.2; stability in the nonlinear case is found to be sometimes a consequence of stability in the linearized case. A criterion against growth of instabilities can be formulated in terms of the Lyapunov function (Sec 6.3) for the case of collisionless plasma.

A small group has been preparing itself for basic studies on superconductors. As a theoretical preliminary, an inquiry is made into the current distribution in proximate superconducting wires, using an electrostatic analogy to solve the problem. A high-field solenoid has been assembled and tested (100 kilogauss), and the first half of an 80-kilogauss coil has been found to perform reliably, yielding by itself 62 kilogauss. Since studies at first will be aimed at the intermediate state of superconductors, of which little knowledge exists, a technique has been developed and tested for holding samples controllably at any temperature in the range 1.5 to 20°K. In addition, a system has been developed for introducing currents of hundreds of amperes into a Dewar environment without intolerable loss of liquid helium. These and other topics in magnetics comprise Chap. 7.

As usual, it is difficult to convey in a progress report the value of support in engineering, electronics, computation, vacuum technology, supply, and business administration that underlie the accomplishment described in these pages. As a final technical note, attention might be drawn to Chap. 9, in which possible advantages are pointed out in the direction of a combination of 3- or 6-Mev H_2^+ injection with 30-kilogauss trapping; the attractive feature is a combination of reduced charge-exchange loss with increased trapping efficiency arising from Lorentz dissociation.

Abstracting Summary

1. DCX-1 PLASMA EXPERIMENTS

The DCX-1 experiments have again been primarily studies of the characteristics of plasma established by low-pressure gas dissociation of the incoming H_2^+ beam.

Measurements of slow plasma currents drifting to insulated end walls positioned outside the throats of the mirror coils indicate that the primary source of these currents is ionization of the background gas by fast trapped protons. Simultaneous measurements have been made of these currents, the intensity of rf activity, the plasma potential (by the lithium beam technique), and signals to neutral-particle detectors (NPD). Coincident with bursts of rf activity there are fluctuations in the electron current out of the mirrors, increases in plasma potential by as much as several hundred volts, and sharp increases in signals to the NPD. At the cessation of the rf activity the current fluctuations cease, the plasma potential drops, and the NPD signals gradually recover to the steady-state values. An explanation is that the heating rate for electrons in the plasma increases with rf activity, the plasma potential then increases in order to balance the rates of loss of slow ions and electrons, the energy-loss rate of the fast circulating protons increases, and these additional losses are reflected in a higher charge-exchange loss rate.

Studies of the various field components of the rf signals confirm the existence of charge clumps rotating with the trapped protons and have also shown, at low pressures, the existence of a repetitive short-burst activity involving purely longitudinal currents or electric fields. Injecting an electron beam into the plasma along field lines causes marked changes in the rf signals and in the energy distributions of the charge-exchange neutrals.

The injection of 400-kev H_2^+ has been coupled with electron-cyclotron heating in the plasma region. Although there is evidence for electron heating, the dissociation of the molecular-ion beam was not enhanced by the modest power levels employed (about 5 w).

2. DCX-2

Experiments with 600-kev H_2^+ injection into DCX-2 with beam current up to 50 ma have yielded plasmas with a nonuniform axial distribution. Densities up to 10^8 fast ions/cm^3 are obtained in the slight field dip at the end of the flat field region, whereas densities of 10^6 to 10^7 are found in the uniform field. The trapped plasma decays with approximately the expected mean life for charge exchange after the injected beam is turned off. The dissociation neutrals show that protons are being produced at the expected rate, but they are disappearing 10 to 50 times more rapidly than expected. The trapped protons may be removed by precession into the injector due to electric fields; by anomalously rapid radial diffusion followed by normal precession into the injector; by unexpectedly high energy-loss rates, resulting in much more rapid charge-exchange rates; or by other unknown processes. Some evidence for anomalous radial diffusion is given by probe measurements showing fast ions at a radius greater than expected. The rather intense, predominantly H^+-ion-cyclotron radiation has been studied, and it exhibits rapid fluctuation of harmonic content and, under some conditions, a random phase relation between probes spaced axially or azimuthally. Evidence for some plasma pumping is found, and probe studies of the cold plasma ejected through the mirrors show only a moderate (<1 kv)

plasma potential and an absence of any appreciable escape of energetic ions axially. The measurements are complicated by clear evidence that a relatively small probe at the mirror maximum affects the electron population seen on a probe close to the flat field region, but along the same magnetic field lines. Further studies of the plasma are under way, and attempts will be made to reduce the instability by electron injection, alteration of the radial electric field, and localized and increased dissociation of molecular ions.

3. PLASMA PHYSICS

The plasma produced by electron-cyclotron resonance in a mirror magnetic field has exhibited interesting new phenomena with a scaleup in applied microwave power above 1 kw. Neutron emission from the deuterium-fed plasma has been observed and validated by foil activation measurements. Further studies have shown that the neutron production rate, the 8-mm microwave noise amplitude, and the axial diamagnetic field increase roughly as the square of the applied microwave power. The maximum microwave noise amplitude and the maximum neutron emission rate are correlated with the microwave heating zones being located near the mirror throats. The maximum neutron emission rate is also correlated with quiescent plasma operation. These neutrons appear to be largely due to the electrodissociation of deuterium by plasma electrons with energies greater than 2.22 Mev.

A theoretical analysis of a plasma which considers only charge-exchange losses, scattering losses, and ion cooling to the temperature of the electron sink has been made. For deuterium plasma whose charge-exchange cross section approaches zero at finite energy, there is shown to be an optimum ion energy near this value for long containment. The plasma decay after source removal has been time-analyzed theoretically, and a decay constant has been predicted. Some experimental observations of a random plasma confined between magnetic mirrors are recorded which seem to confirm the theory. A shift in the resonant frequency of a microwave cavity enclosing the plasma is shown to be a good diagnostic tool for the determination of the plasma decay constant.

An army surplus Snooperscope has been converted to a stroboscopic device for observing periodic fluctuations in plasma light intensity.

4. VACUUM ARC RESEARCH

An analogy to possible fuel-feed heating mechanisms is suggested by continuing studies on the magnetically confined carbon arc. "Fuel" ion temperatures up to 2.5×10^6 °K are reported; the evidence suggests rapid internal electric-field heating transverse to the magnetic flux lines.

5. ION PRODUCTION, ACCELERATION, AND INJECTION

The DCX-2 injection system has been operated at total ion currents up to 150 ma while injecting into the plasma region. The maximum H_2^+ ion current injected into the machine does not increase significantly, however, as the total current is increased above 100 ma. The maximum H_2^+ beam injected has been 50 ma with a total current of 150 ma.

The original accelerator tube developed for high-current injection was replaced with one that has epoxy skirts cast around the porcelain insulators. This tube has operated on DCX-2 at greater than 600 kv, but not reliably above 570 kv. Modifications are being tested which should allow satisfactory operation at 600 kv.

An FM link was developed to transmit current information with time resolution of about 10 μsec from the 600-kv level to ground.

The equipment for doing beam emittance work has been installed at the High-Intensity-Beam Facility, but time has not permitted its use.

The 100-kev neutralized-beam accelerator has been operated in the 10- to 20-kev range with hydrogen, helium, nitrogen, and argon. The hydrogen results are unique in that the injected electron beam may be made to increase, by a factor of 4 to 5, the power delivered to target over that obtained without electron injection. The current equivalent to the measured power on the target is about 18 to 20 ma. The beam is believed to be neutralized because the power on target is independent of whether the target is at ground potential or electrically insulated. In the latter case, the target floats at ground potential.

No significant power increase due to electron injection has been observed with the helium, nitrogen, and argon beams.

6. THEORY AND COMPUTATION

The effect of a distribution of ion cyclotron frequencies on the cyclotron resonance instability is investigated. The dependence of the cyclotron frequency on position in the machine is neglected. A distribution in ion cyclotron frequencies has the same effect qualitatively as a thermal distribution of ion velocities; both tend to stabilize the plasma. If the spread in frequencies is sufficiently great, then the plasma is stable for sufficiently high particle densities.

Stability in the nonlinear case is found sometimes to be a consequence of stability in the linear case. The use of the Lyapunov functions in connection with moment equations and the linearized Vlasov equation suggests a rather general treatment of the problem of stability without the necessity of detailed solution of the equations.

Two topics that are briefly treated are the stability of inhomogeneous collisionless plasma and correlation damping.

The cross section for the Coulomb dissociation of deuterons by electrons has been calculated from the threshold at 2.2 Mev to 6 Mev in the electron energy.

A new code, MADCAP, has been written for the calculation and plotting of single-particle trajectories in electromagnetic fields. By computing the magnetic field by Taylor's series expansion from a stored table of field components and derivatives, a time factor of ~ 6.5 is gained over previous codes. Plots of pertinent physical information are also prepared by the code.

Two codes, one for energy-spectrum analysis and one for containment zones, have been written to facilitate studies of data taken in DCX-1.

The study of the relationship between molecular-ion injection current and trapped-ion density has been continued, treating molecular-ion energy, path length, and an arbitrary enhancement of energy transfer rates as parameters.

7. MAGNETICS AND SUPERCONDUCTIVITY

Two new codes for calculating magnetic properties of current systems are discussed. The first is based on zonal harmonics, and the second is based on Gaussian integration of elliptic integrals.

Three new magnet coils representing advances in dc magnet technology are described: a magnet designed to produce 118 kilogauss (2-in. bore), one coil of an 80-kilogauss pair (7-in. bore), and a 6-kilogauss solenoid wound from flexible cable. The 2-in. magnet has been successfully tested at 104 kilogauss, and during safety tests the other two coils performed as expected at their design current.

An efficient cryostat test cell has been designed and tested. Temperature stability of $\pm 0.01^{\circ}$K throughout the range 1.5 to 20°K facilitates a variety of experiments. More advanced designs are also discussed.

The introduction of large currents into a cryogenic apparatus creates a heat leak problem. Attempts to minimize the heat leak of nitrogen precooling and gas cooling are described. A 50% reduction in vaporized helium was found possible.

The performance of superconducting coils is so complex that it is not yet well understood. One initial step toward reaching a better understanding is a study of the proximity effect displayed by two parallel, infinitely long superconducting wires. For ideal superconductors the magnetic field produced by currents flowing through the wires is calculated on the assumption that the surface layer of each superconductor is superconducting. Preliminary experiments were made to find the critical current strength and to determine the resistance performance in intermediate state. A more complete experimental and theoretical analysis is under way.

8. VACUUM SYSTEMS, TECHNIQUES, AND MATERIAL STUDIES

Vacuum studies have provided data on the sticking factors of various gases in baked systems. Nude-gage calibrations have shown that in systems pumped by oil diffusion pumps, significant discrepancies in pressure readings may exist. Diffusion-pump studies have included development work on a surface-boiling pump in which oil level

appears to play a significant role on the fluid throughput of the pump and on relative pumping speeds for H_2 with respect to air.

9. SPECULATIONS ON THE ATTAINMENT OF A HIGH DENSITY AND LARGE CIRCULATING CURRENT OF VERY HOT PROTONS IN A MAGNETIC-MIRROR DEVICE

Speculation is made on the attainment of a high density ($\gtrsim 10^{12}$ protons/cm^3) and large circulating current of very hot protons in a magnetic-mirror device. Lorentz trapping and exponential growth resulting from injection of 6-Mev H_2^+ into a 30,000-gauss field suggest the possibility of producing a natural plasma configuration in which a closed toroidal magnetic bottle may be developed by the applied mirror magnetic field and the self-field of the azimuthal proton current.

10. DESIGN AND ENGINEERING – SERVICE REPORT

The activities of the Engineering Services Group are generally reported incidentally with the research efforts of other groups of the Thermonuclear Division. The group executes or coordinates engineering design, shop fabrication, building operations, and maintenance.

1. DCX-1 Plasma Experiments

J. L. Dunlap
R. S. Edwards
G. R. Haste
L. A. Massengill
Herman Postma
J. A. Ray
R. G. Reinhardt
W. J. Schill
R. M. Warner
E. R. Wells

1.1 INTRODUCTION

The mechanical configuration of the DCX-1 apparatus during this period was essentially that described in the previous report.[1] Some modifications were made to shields in the intermediate vacuum region for more effective bakeouts. The intermediate-region base pressure was reduced from about 4×10^{-8} torr to 1.5×10^{-8} torr, but the base pressure in the plasma region was not reduced. The longest trapped-proton charge-exchange lifetime is, then, still the 37 sec noted in the previous report.

In the following sections the details are given of several experiments that are continuations of earlier work. In addition two new topics are introduced: studies of the slow plasma drifting out of the mirrors, and the coupling in DCX-1 of hot-ion injection with electron-cyclotron heating.

1.2 DC LEVELS OF SLOW PLASMA CURRENTS AND THE PLASMA POTENTIAL

The average current drifting along field lines out of the DCX-1 mirrors consists of essentially equal flows of ions and electrons. Several reactions contribute to this current, but calculations indicate that ionization of the background gas in the plasma region by fast trapped protons dominates by about two orders of magnitude.

A circular copper plate, separated into a 225° and a 135° sector, was positioned just outside each of the mirrors as indicated in Fig. 1.1. The 225° sectors were mounted on insulators, and leads to the sectors were brought out through the walls of the apparatus so that the plates could be biased to preferentially collect either the ion or the electron component of slow plasma current. Typically, one of the collector plates was grounded, and the other was connected through a variable bias supply and current amplifier to ground. The 135° sectors were grounded, were aligned to intersect the same field lines, and were drilled to allow passage of the lithium-ion beam

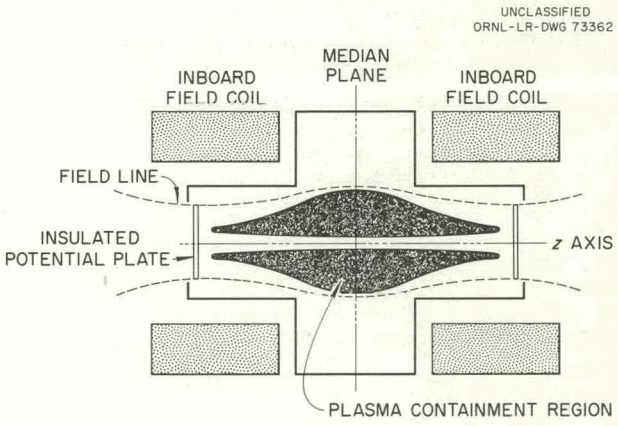

Fig. 1.1. Axial Section of DCX-1, Showing the Position of Insulated Plates Arranged to Collect Slow Plasma.

[1] *Thermonuclear Div. Semiann. Progr. Rept. Apr. 30, 1962*, ORNL-3315, p 1, sec 1.1.

used to probe the plasma potential by the technique previously described.[2]

In this section we discuss the changes with bias voltage of the dc level of the current to the biased collector plate, and the changes with bias voltage of the average value of the plasma potential. Fluctuations of the two quantities were observed to be coincident with coherent rf signals from the plasma; these are described in Sec 1.3.

Calculations of the effects of secondary-electron emission from the collector plates indicate that these effects are primarily quantitative in nature and would not interfere with conclusions based on qualitative features of the bias curves.

Figure 1.2 shows the response of the dc current level to a variation of bias in the range ±400 v.

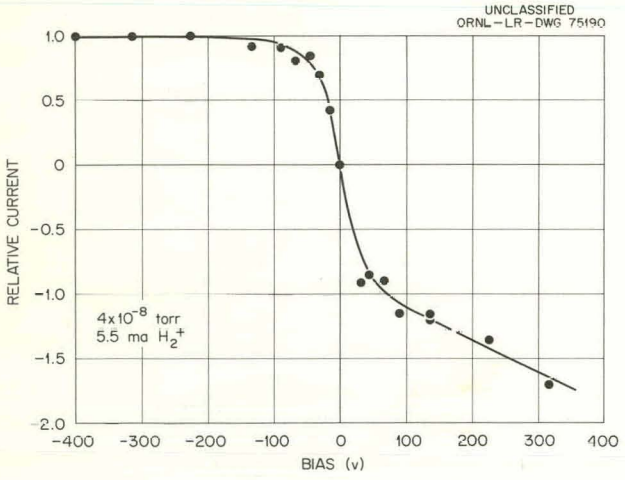

Fig. 1.2. Variation of Collector-Plate Current with Bias.

The dominant features are: (1) zero net current at zero bias; (2) a symmetric current response to the first variations from zero bias; and (3) an asymmetric response to further variations in bias, with a positive current that saturates with increasing negative bias but a negative current that increases with positive bias. The zero current obtained with zero bias obviously indicates a zero net charge flow out of the mirrors. This is expected, since the primary source of the currents, ionization, produces ion-electron pairs; and since secondary electrons, which are confined to magnetic field lines, can contribute no net charge flow. The current variations with bias in the range of about ±100 v are attributed to effects of the applied potential in attracting or repelling the electron component of the slow plasma current, and the variations from +100 to +400 v are attributed to effects of the potential in repelling the ion component.

Under some conditions of operation, the symmetry about zero bias extends to high enough positive bias to show a plateau in negative current before the effects of the applied potential in repelling the ion component become obvious. In one series of experiments under these conditions, the saturation current levels were measured as functions of the injected H_2^+ current and of the neutral-gas pressure in the plasma region. The levels scaled directly with the beam current and, once the pressure was raised significantly above base, directly with the pressure. These observations are those expected for production of the slow plasma through ionization of the background gas by fast trapped protons. The current levels observed, of the order of a microampere, are also appropriate for this ionization as the source.

Figure 1.3 shows the response of the average value of the plasma potential to variations of bias. The potential is a function of bias only for positive bias. Models to account for the qualitative features of Figs. 1.2 and 1.3 are being developed.

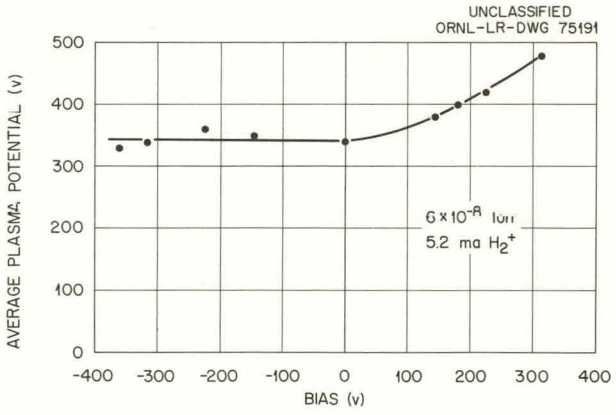

Fig. 1.3. Variation of Average Plasma Potential with Bias.

[2] *Thermonuclear Div. Semiann. Progr. Rept. Apr. 30, 1962*, ORNL-3315, pp 8–10, sec 1.3.

1.3. CORRELATIONS BETWEEN PLASMA PARAMETERS AND COHERENT RADIO-FREQUENCY SIGNALS

Our previous reports have attributed a number of features of the DCX-1 plasma to the effects of an electrostatic instability. At operating pressures in the 10^{-9}-torr range (now almost routinely available), the coherent rf signals, which are taken as indicating the appearance of the instability, occur in short, intense bursts. This aspect of low-pressure operation has permitted studies of the correlations between a number of parameters and the appearance of rf activity, and hence, by inference, studies of these parameters in the presence and in the absence of the instability.

Studies of the slow plasma currents with the experimental arrangement described in Sec 1.2 showed fluctuations in the electron component during periods of rf activity, with an increase in electron current from the plasma at the beginning of the rf burst. Figure 1.4 shows these fluctuations. The rf trace here is the rectified output of a narrow-band amplifier tuned to the proton-cyclotron fundamental, and the probe was a single-turn electrostatically shielded loop mounted in the median plane outside the plasma-confinement region. Fast scans of the current fluctuations show that the periods of excess electron current are typically 2 to 5 msec in duration, and that the periods of deficient electron current are typically 5 to 15 msec in duration.

Figure 1.5 shows variations in the transmitted lithium-ion beam, again with the experimental arrangement described in Sec 1.2. For these particular conditions, the plasma potential was generally below 200 v without rf activity and above 200 v with rf activity.

Under some conditions the neutral-particle detectors show pronounced variations coincident with rf bursts. Figure 1.6 illustrates this. The detector signals rise sharply with rf activity and then begin a slow recovery back toward a steady-state value. This slow recovery indicates that the increases in signal are due to an increased charge-exchange reaction rate and not to fast trapped protons that are driven out to the detectors during rf bursts. This point has been checked by removing the foils from some of the detectors, leaving bare Faraday cups. Signals from these

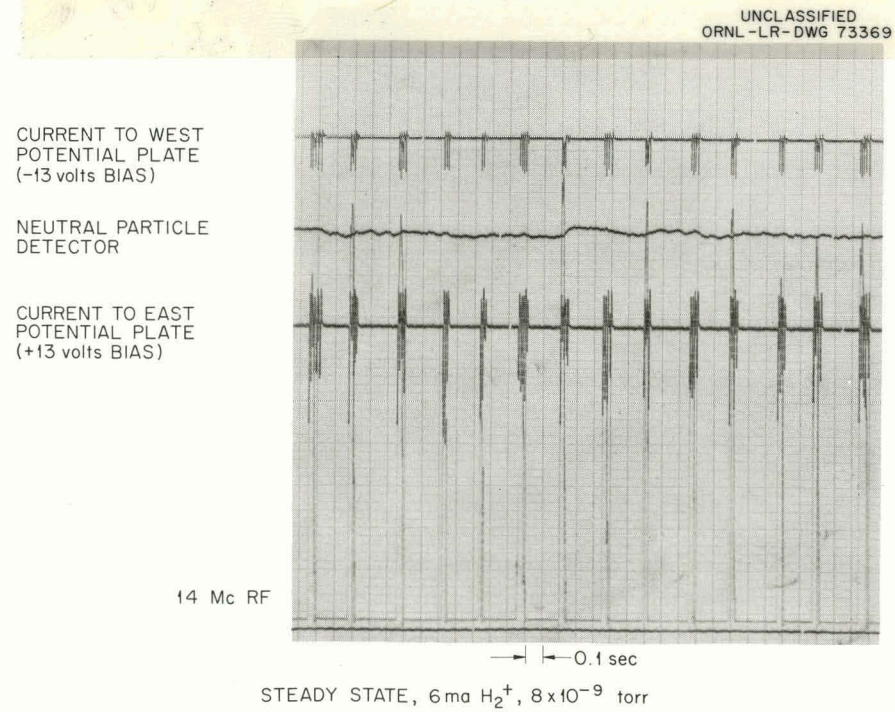

Fig. 1.4. Variation of Potential-Plate Currents with RF Activity. (An upward deflection represents an increase in net positive current.)

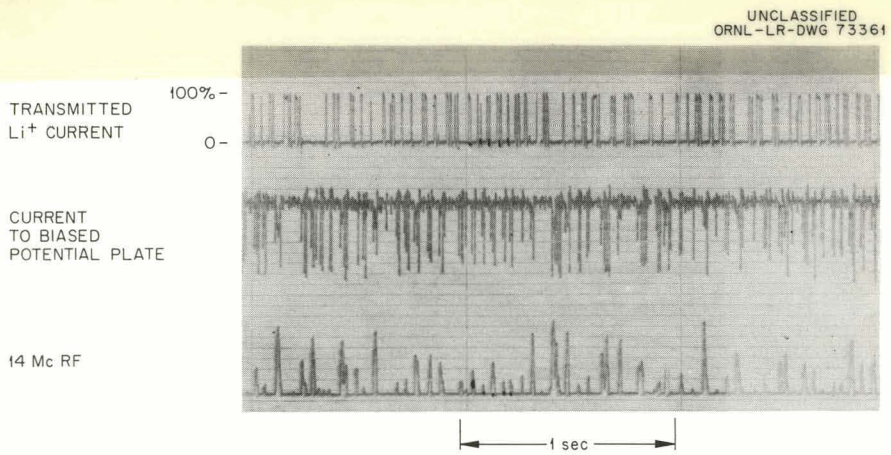

STEADY STATE, 5.3 ma H_2^+, 1.6×10^{-8} torr, Li^+ $V_{ACCEL} \approx 200$ volts, −15 volts PLATE BIAS

Fig. 1.5. Variations of Transmitted Lithium-Ion Beam Current and the Current Collected by a Biased Potential Plate with RF Activity.

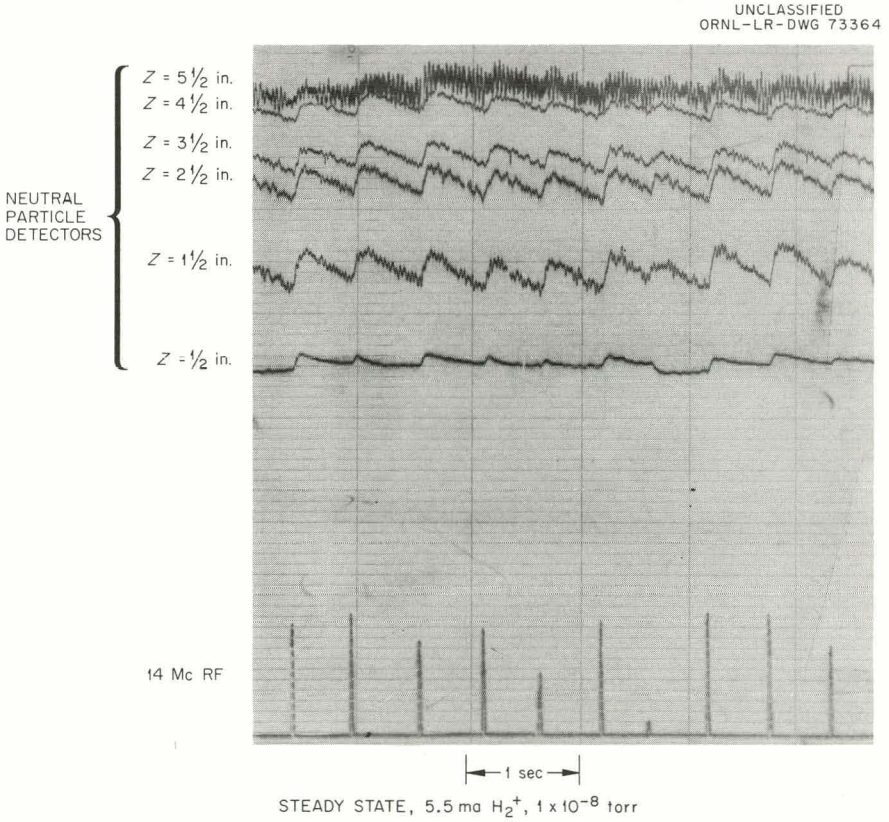

STEADY STATE, 5.5 ma H_2^+, 1×10^{-8} torr

Fig. 1.6. Variation of Neutral-Particle Detector Signals with RF Activity.

cups were observed coincident with rf bursts, but the shapes and amplitudes were proper for the cups to then be acting only as electrostatic probes responding to fluctuations in plasma potential.

In a few cases it has been possible to obtain rf bursts isolated even more completely than shown in Fig. 1.6. The recovery of the neutral-particle detector signals to steady state was then roughly exponential, with time constants about one-fifth the charge-exchange decay time for the steady-state trapped-proton distribution. Using this time constant and the relative increase of the total charge-exchange signal above the steady-state value (about 20% in these cases) suggests that about 4% of the trapped protons were degraded about 75 kev during each of the periods of rf activity, which were about 50 msec in duration. No great accuracy can be claimed for this result, which in any case applies only to a few isolated cases; but the result does serve to indicate the possible effect of the instability on the proton energy distributions. A more accurate and useful approach to the problem of determining this effect is to measure the energy distributions of the fast charge-exchange neutrals in coincidence and in anticoincidence with the rf activity. This work is under way, but the data are insufficient to warrant a description of the results at this time.

A qualitative explanation of these observations can be given with Fig. 1.7. Before the initial burst of rf activity all parameters are in steady state. In particular the electron heating rate and plasma potential are steady, and electrons are drifting out of the plasma at the rate at which they are formed. We assume that the instability responsible for the rf signals also raises the electron heating rate. With the higher rate, the electron current momentarily increases above the steady-state value, so some electrons stored in the plasma are lost and the plasma potential goes more positive. When the rf activity dies away, the electron heating rate drops, the electron current goes below the steady-state value, and electrons are then stored in the plasma until the potential recovers. During the interval of increased potential, the energy-loss rate for trapped energetic protons rises above the steady-state value, and proton energies are degraded. The charge-exchange reaction rate then rises during this interval, and

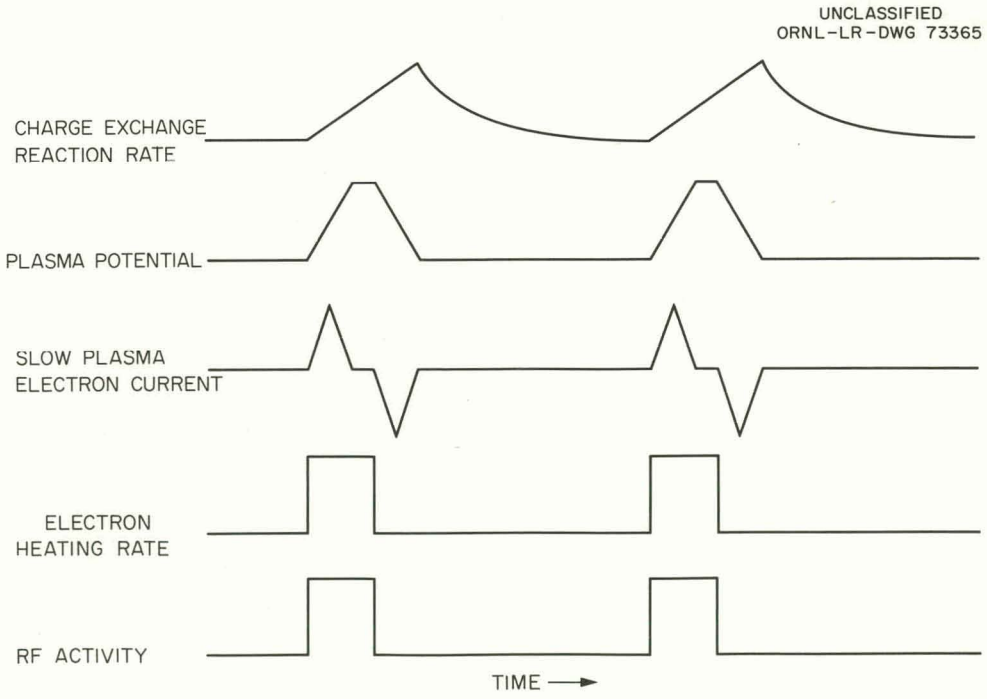

Fig. 1.7. Qualitative Response of Several Plasma Parameters to Intermittent RF Activity.

afterward recovers to steady state with an appropriate time constant.

Simple quantitative checks appear to be in reasonable agreement with this explanation. For a cycle of electron-current fluctuation that begins and ends with the steady-state current, the negative charge lost from the plasma during the interval of excessive electron current is equal to that restored to the plasma during the interval of deficient electron current. The amount of charge removed and then restored is enough to change the plasma potential the several hundred volts observed. The additional energy that has to be supplied to the cold plasma during the interval of increased plasma potential is of the order of the energy loss suffered by the trapped protons during that interval, as estimated from the neutral-particle detector data by the method just described.

The direct association of the electron heating rate and the rf activity employed in Fig. 1.7 is not yet completely justified. As shown in Fig. 1.4, a single burst of rf activity as presently detected can give rise to a number of cycles of electron-current variation. The probe system employed is sensitive to several field components. It is not yet possible to say which of these components is most closely correlated with the individual cycles of current variation.

Figure 1.8 shows the response of a number of parameters during plasma decay and buildup. Here the slow-plasma collector plate has a negative bias strong enough to repel nearly all of the electrons, so the fluctuations in electron current produce only small fluctuations in the current level to the collector. Note that the decay and buildup of the collector current are very much like those of the neutral-particle detector. Both signals respond to variations in the fast-proton density. Also note that rf activity continues for only a short time after the H_2^+ beam is shut off, and that the plasma potential continues to fluctuate with rf activity during that time interval.

By repeating a number of decays and buildups with different values for the acceleration potential of the lithium-ion beam but with other parameters kept constant, the decay and buildup of the plasma potential were determined. The results are presented in Fig. 1.9. For these runs, the charge-exchange decay time for the steady-state proton-energy distributions was about 5 sec, and the plasma potential on steady state fluctuated between 260 and 600 v. A peculiarity of the lithium-ion gun sets a lower limit on the acceleration potential of about 15 or 20 v, so it was not possible to probe for plasma potentials lower than

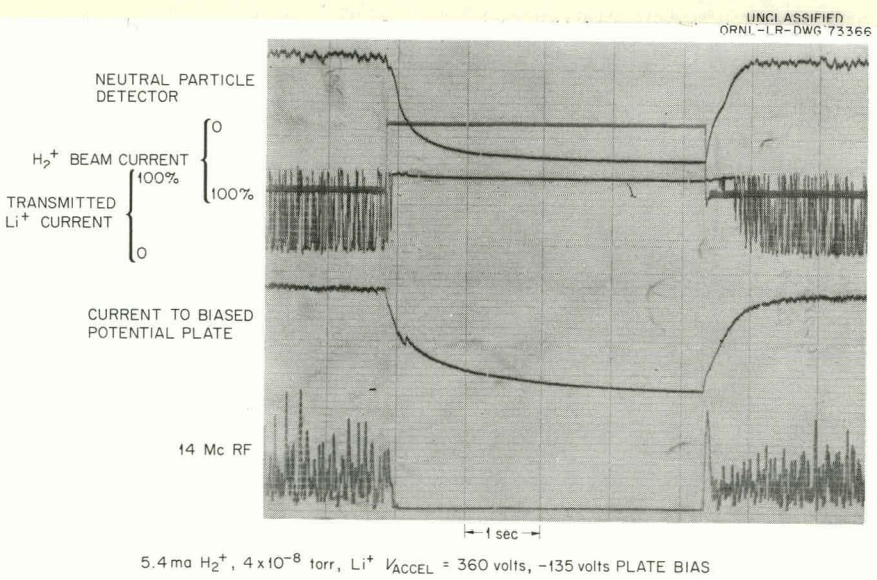

Fig. 1.8. Decay and Buildup Responses of Neutral-Particle Detector, Transmitted Lithium-Ion Beam, Current Collected by a Biased Potential Plate, and RF Activity.

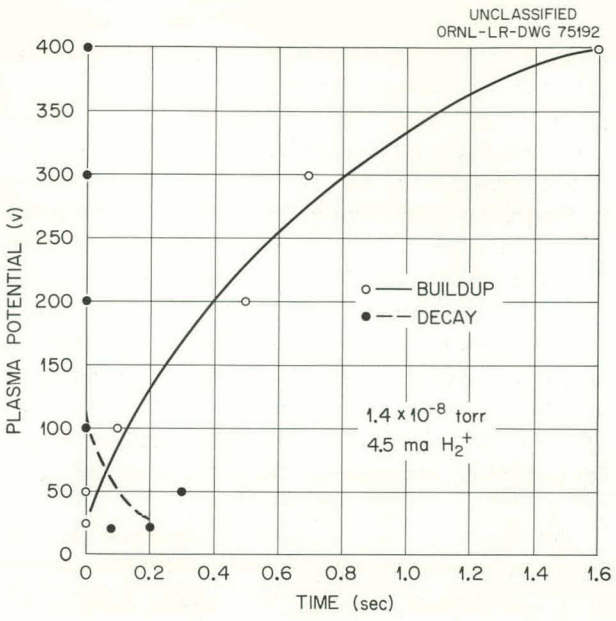

Fig. 1.9. Response of the Plasma Potential During Buildup and Decay Intervals.

this value. Recent calculations[3] indicate that at the low pressures the plasma potential should be below about 30 v if the rate of energy transfer to electrons is that of Coulomb collisions without any collective enhancement.

1.4. EXPANSION OF THE PLASMA VOLUME

The expansion of the plasma to larger volumes as the H_2^+ beam current is increased or as the pressure is lowered has been previously reported,[4] and it has been suggested that the plasma expansion is driven by the charge clumps formed in the circulating proton ring.

Further evidence in support of this suggestion was found in those fluctuations in the neutral-particle detector signals that occur coincident with the intermittent rf activity at low operating pressures. At least in some cases, the relative increases in signal levels are greater for detectors off the median plane than for detectors centrally located.

Studies of the axial distribution of the steady-state charge-exchange signals have contributed further support. The full widths at half maximum (fwhm) of these profiles are generally taken to be the mean Z extent of the plasma. Measurements of the fwhm as functions of pressure and H_2^+ beam current fit fairly well the expression $Z = A(I\tau) + B$, where A and B are constants, I is the H_2^+ beam current, and τ is the measured charge-exchange decay time. If the mean volume of the plasma is then taken as the volume of the containment zone with full Z extent equal to the fwhm of the detector profile, measured profiles can be related to plasma volumes.

It has been found that the low-pressure volumes are reduced by operating at a magnetic field strength somewhat higher than the standard field value, that which produces a 3.25-in.-radius stable orbit for trapped 300-kev protons. Figure 1.10

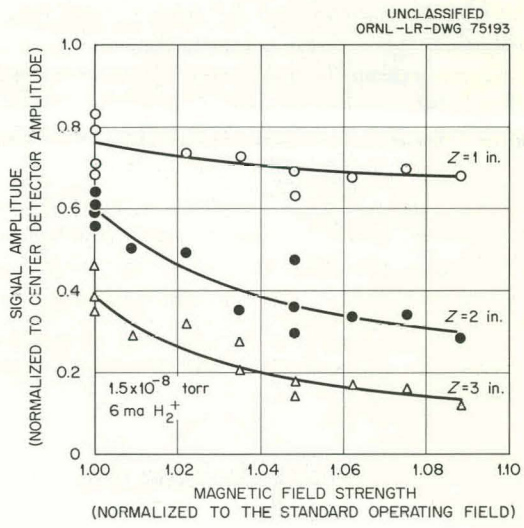

Fig. 1.10. Neutral-Particle Detector Signals as a Function of Magnetic Field.

shows the variation with magnetic field of the relative amplitudes of signals from a set of neutral-particle detectors at different distances from the median plane. The profiles from this set of data, when interpreted in the sense just described, indicate that a reduction in the mean plasma volume from about 2 liters to about 1 was obtained with a 10% increase in magnetic field.

---

[3] T. K. Fowler and Mozelle Rankin, "Plasma Potential and Energy Distributions in High Energy Injection Machines," the *Journal of Nuclear Energy, Part C.*

[4] *Thermonuclear Div. Semiann. Progr. Rept. Apr. 30, 1962*, ORNL-3315, pp 13–14, sec 1.6.

There are some data indicating that reductions in volume are also obtained by operating at reduced field values. Certain experimental difficulties are peculiar to the use of a reduced field and so far have prevented profile determinations of the desired accuracy. That a field reduction decreases the steady-state plasma volume is, then, presented as a tentative conclusion, subject to more thorough studies.

In these experiments, the H_2^+ beam trajectory is first adjusted, while using the standard field value, so as to minimize the initial precession of trapped protons; that is, to inject into the containment geometry protons with the most ordered velocity distributions. The beam trajectory is then not readjusted with changes in the field. Studies of the change in this trajectory relative to the change in the proton stable-orbit radius show that variations from the standard magnetic field result in trapping of protons with progressively more initial disorder.

Disorder in proton motion tends to stabilize against both the negative mass[5] and the Harris instabilities (see Sec 6.1, this report), so an explanation for these observations is that the plasma is partially stabilized against these instabilities by injection with more proton disorder. Changes in the coherent rf signals from the plasma indicate that the charge clumping is affected by changing the field. There is a general trend toward more isolated rf bursts with departures of the field from the standard value. In some cases of extremely low-pressure operation this effect is quite pronounced; the repetition rate of the rf bursts has been reduced a factor of 10 by an increase of 10% in the magnetic field.

1.5. ELECTRON-CYCLOTRON HEATING IN DCX-1

The results of electron-cyclotron heating in the Physics Test Facility (PTF) (see Sec 3.1, this report) have prompted efforts to add such heating to DCX-1. The primary benefit to be expected from providing a dense hot electron gas in the plasma region is increased dissociation of the molecular-ion beam, with an attendant increase in the density of trapped fast protons. Additional benefits may arise from a possible damping of the present instability or a reduction in the plasma potential.

Calculations of the performance of DCX-1 with electron-cyclotron heating have required some assumptions and extrapolations of performance characteristics from PTF data. The calculations indicate that a few watts of power at 26.5 kMc could support a 20-kev electron density of $10^{11}/cm^3$ in the vicinity of the DCX-1 plasma, and that in the presence of these electrons a well-behaved fast-proton plasma would build up to densities of 10^{12} to $10^{13}/cm^3$ with operating pressures and H_2^+ currents well within the present capabilities of DCX-1.

The electrons accumulated in the PTF experiments originate from ionization of the background gas. The low operating pressures desired in DCX-1 will probably require that an additional source of electrons be provided. Calculations indicate that an electron feed rate of 0.1 ma should maintain a steady-state density of $10^{11}/cm^3$. A possible solution to this problem is direct feeding of the resonant regions with a high-current electron beam projected along magnetic field lines. A gun has been designed and tested that provides 500-v electrons in currents up to 500 ma. The electron beam is annular and is projected down the center of the machine. At the midplane the radius of the annulus is 3.25 in. (the 300-kev proton stable-orbit radius) and the width is about 0.1 in.

Microwave power tubes of the desired frequency are not readily available, so the few experiments to date have used about 5 w of 21-kMc power. In order to obtain resonance heating in the plasma region, the magnetic field was reduced and the H_2^+ injection energy was lowered from 600 to 400 kev. There was evidence for electron heating upon application of the microwave power. Without H_2^+ injection, x-ray counts outside the apparatus increased when the microwaves were turned on, and at pressures above about 10^{-5} torr the heating zones glowed. With H_2^+ injection, x rays from the injection system prevented a meaningful measurement of these, but the pressures at which the heating zones glowed with the application of microwave power then extended down to 2×10^{-6} torr. There was no obvious enhancement of the fast-proton trapping rate by the microwaves. The data are such that this rate could not have increased by as much as a factor of 2. Cutting the

[5] T. K. Fowler, *Calculation of the Negative Mass Instability for DCX-1*, ORNL CF-61-7-1 (July 1961).

electron gun on and off appeared to make no difference in the proton trapping rate.

A tube giving several watts at 26.5 kMc is expected shortly, and these experiments will be continued with the full 600-kev injection energy.

1.6. RADIO-FREQUENCY MEASUREMENTS[6]

Although we are not yet in a position to specify precisely what sorts of rf activity are involved in each of these experiments, considerable progress has been made in the development of probes and techniques for isolating the various field components. The observations at high pressure ($>10^{-8}$ torr) do not contradict the explanation previously proposed, that of azimuthal clustering of the circulating protons. As an example of these observations, Fig. 1.11 shows the wave form observed during the initial portion of an rf buildup at high pressures. The wave form is appropriate for a single rotating charge clump. At about the peak of the rf buildup, the harmonic content changes to indicate a splitting of the single clump. The various additional frequencies are near proton-cyclotron harmonics. Then appear beat frequencies that are apparently due to the presence of charge clumps at different magnetic field values. With the pressure high enough to concentrate the plasma near the median plane, the beat frequencies are of the order of 100 kc and a particular wave form will persist for hundredths or tenths of a second. This last observation indicates that individual clumps exist as separate entities for long periods of time. With reductions in pressure into the range where spreading of the plasma occurs, the modulation patterns are much more complex, presumably the results of clumps existing at greater distances from the central stable orbit.

At the lowest pressures there is in addition to these fields a repetitive short-burst activity involving purely longitudinal currents or electric fields and uncorrelated with the azimuthal activity. Figure 1.12 shows how these signals appear on a probe sensitive to longitudinal currents but are absent on one oriented for azimuthal currents. The frequency response of the system extended to about 30 Mc. There are as yet no other data on the frequency composition of the longitudinal signals.

Preliminary studies have shown that marked changes occur in the characteristics of the low-pressure rf activity when it is examined as a

UNCLASSIFIED
ORNL-LR-DWG 73359

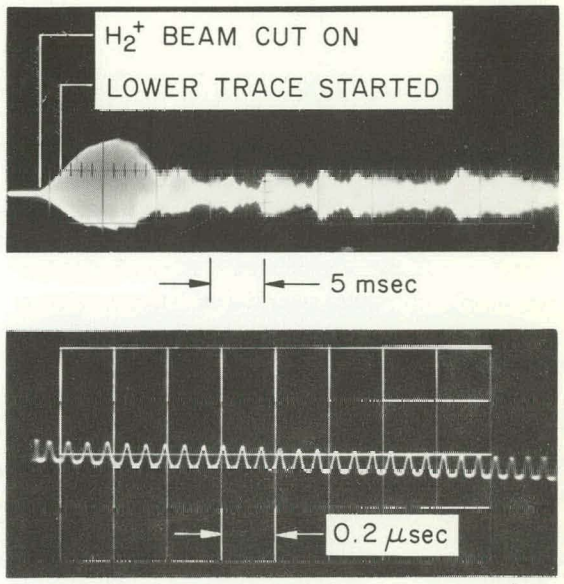

6 ma H_2^+, 4×10^{-7} torr, PROBE I IN A+B

Fig. 1.11. Signals from a Probe System Sensitive to Changes in the Radial Component of *E*.

UNCLASSIFIED
ORNL-LR-DWG 73360

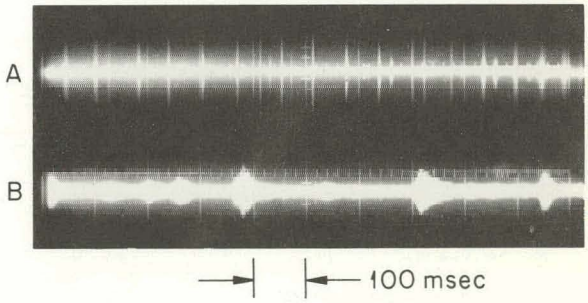

STEADY STATE, 5.3 ma H_2^+, 4×10^{-9} torr, PROBE I IN A-B

Fig. 1.12. Simultaneous Signals from Probe Systems Sensitive to Longitudinal (*A* Trace) and Azimuthal (*B* Trace) Currents.

[6]With C. E. Nielsen, consultant from Ohio State University.

function of current from the electron gun described in Sec 1.5. One such study was done with the broad system used for the data of Fig. 1.12. The electron energy was kept constant at about 500 v. A few milliamperes of electron current (measured to a target after the beam had traversed the plasma) would completely damp out the longitudinal bursts without perceptively affecting any characteristics of the azimuthal activity. With increased electron current, the longitudinal signals reappeared, again sometimes concurrent with azimuthal signals and sometimes when there was no such activity. At some level the indicated electron current would begin to flicker downward and then an additional small increase would drop the current to a steady value. The critical value at which this transition occurred was a function of pressure and H_2^+ beam current, but this dependence has not been explored. For 4×10^{-9} torr and 5 ma H_2^+, it ranged from 200 to 400 ma, and the reduction in current upon dropping to the steady value was as much as 50 ma. Strong longitudinal activity occurred coincidently with the current flickers and became steady and continuous when the electron current dropped to the steady value. The amplitude of this activity would remain constant for long periods of time (for seconds), and at any given time the rf signals were nearly single-frequency (in the range 3.5 to 30 Mc).

A second series of experiments with about 8×10^{-9} torr and 6 ma H_2^+ used a simpler single-loop probe and narrow-band electronics tuned to the proton-cyclotron fundamental, about 14 Mc. The electron beam energy was 320 ev. With zero electron-gun current the rf-burst repetition rate was about 10/sec. This rate was reduced to about 5/sec with 70 ma of electrons and to about 3/sec with 180 ma. With about 200 ma the 14-Mc rf was essentially damped out on steady state. Since no simultaneous broad-band rf measurements were made, there may have been considerable rf activity at other frequencies. These observations, then, do not necessarily contradict the broad-band ones just described, since the current required to damp out the 14-Mc rf activity is about that required to drive the system to steady activity at other frequencies in the first series of experiments.

The few milliamperes of electron current may damp out the longitudinal activity by acting as a sink which prevents the accumulation of energy in that particular mode.[7] A two-stream instability is the most obvious source for the rf signals observed with high electron beam currents.

1.7. ENERGY ANALYSES OF STORED AND EMERGING PARTICLES

The work in progress to measure the energy distributions of charge-exchange neutrals in coincidence and anticoincidence with rf activity was described in Sec 1.3.

Other studies have shown that the energy-loss rate for circulating protons increases in the presence of an electron beam from the gun described in Sec 1.5. There appears to be a current threshold for this effect. In one experiment at 2×10^{-8} torr with 4 ma H_2^+, no changes in the energy distributions were noted for electron currents up to 2 ma; significant degradation was noted for 16 ma of electrons, but the spectra changed very little for further current increases to 400 ma. There is verification for these observations in the charge-exchange decay times for the steady-state proton distributions. Measurements at 8×10^{-9} torr with 6 ma H_2^+ current showed that an electron current of 50 ma reduced the decay times to about one-third those measured with zero current, but there were no further significant decreases for increases in electron current up to 400 ma.

1.8. ACKNOWLEDGMENTS

The authors wish to thank T. K. Fowler, E. G. Harris, and C. E. Nielsen for numerous helpful discussions; R. A. Dandl, H. O. Eason, and the other members of the PTF Group for their continuing assistance on a variety of electronic problems, particularly the application of electron-cyclotron heating to DCX-1; and Mozelle Rankin and D. A. Griffin for their code work on the IBM 7090 and the Oracle.

---

[7] A suggestion made independently by C. E. Nielsen and E. G. Harris. The question is being investigated in detail by Harris and T. K. Fowler.

2. DCX-2

P. R. Bell
J. S. Culver
R. C. Davis
S. M. DeCamp
J. C. Ezell
R. A. Gibbons
G. G. Kelley
N. H. Lazar
O. B. Morgan
J. D. G. Rather
T. F. Rayburn
R. F. Stratton
J. C. Thompson
C. W. Wright
A. J. Wyrick

2.1 INTRODUCTION

The DCX-2 apparatus has been described elsewhere.[1] It is designed to produce an energetic-proton plasma in a mirror magnetic field by dissociation of energetic H_2^+ ions over a long path in the magnetic volume. The device is complete and experiments are under way. All the principal components (the accelerator and injection system, including the shielded injection channel or "snout," the coils producing the tailored magnetic field, and the vacuum system) are operating more or less as expected. The expected plasma behavior as a function of injected ion current has, however, not been observed. In fact, hot-ion densities of only $2 \times 10^6/cm^3$ are seen in the flattest region of the magnetic field. In certain regions of the field, however, the density appears to be as much as $10^8/cm^3$. These plasmas decay following beam turnoff with mean times not inconsistent with charge-exchange losses; however, with the beam on, the losses must increase by a factor of at least 50 to produce the observed results.

These experiments and findings are described in the following sections.

[1] P. R. Bell *et al., Thermonuclear Semiann. Div. Progr. Rept. Apr. 30, 1962,* ORNL-3315, pp 15–20; *Nucl. Fusion: 1962 Suppl., Pt 1,* 251–58; ORNL CF-60-1-73 (Mar. 4, 1960).

2.2 MAGNETIC FIELD

Just after the writing of the last report (ORNL-3315), the magnetic field was rescanned and found to be somewhat nonuniform. Several faults were finally located and corrected. Small sections of the mirror coils which were known to be shorted had been compensated by deliberate shorts in other sections. At an unknown time, some of these accidental shorts had opened, leaving the mirrors unbalanced. It was found, too, that the water-cooled shunts across the sections of the inboard coils were changing in resistance because of electrophoretic deposition on the winding forms. The method of winding was modified to eliminate large voltage drops across small sections of insulator, apparently eliminating this difficulty.

When the work on the magnetic field was stopped to resume the plasma experimentation, some features of the field shape were left unexplained. The inboard coils require especially large deviations from expected values in the provided trimming currents. In addition, the two dips at the ends of the flat region are not symmetrical. The trouble may be due to inaccuracy in location of the inboard coils. The magnetic field in the central region is very sensitive to the position of these coils. Figure 2.1 shows the most recent plot of the magnetic-field strength on the axis. Many individual voltage drops and currents are being monitored to detect changes in the coils.

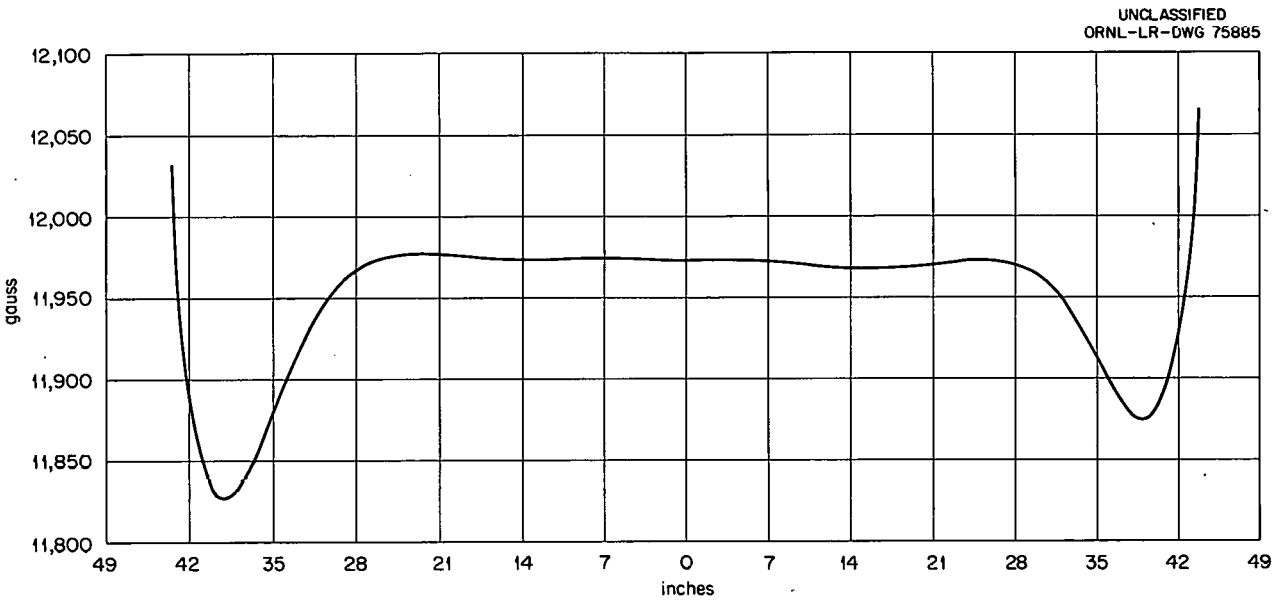

Fig. 2.1. Magnetic-Field Strength on the Axis as a Function of Axial Position.

2.3 BEAM TRAJECTORY

After the field had been adjusted, the beam was found to be spiraling past the center of the machine. A water-cooled probe was inserted from the injector side of the machine to intercept the molecular ions after they passed the midplane (probe No. 8, Figs. 2.2 and 2.3). Power returning to the injector was measured calorimetrically. It was found that when the field was adjusted properly, no current returned to the injector target when the beam was interrupted by the water-cooled probe. At higher currents through the inboard coil sections, the beam could be made to return to the injector in spite of the probe, indicating reflection of the beam before it reached the midplane. The pattern observed on the injector target was consistent with this interpretation. No return beam was visible for low inboard field currents, and when the central field was increased a sharp, well-defined line appeared at the intersection of the target and a cylinder containing the molecular-ion orbit (see Fig. 2.2). When the intercepting probe was removed, two diffuse lines of intersection (apparently produced by orbits of the same diameter) appeared, one bordering the sharp line defining direct return, but spread in the direction of precession, and the other shifted still farther in this direction.

2.4 INJECTOR

The performance of the ion injector for DCX-2 is described in detail in Sec 5.1. Calorimetric measurement of the power deposited on the inside of the injector and on the return beam target gives only rough agreement with total power-supply drain. These figures indicated as much as 50 ma of injected H_2^+ under certain conditions.

2.5 FAST-ION DENSITY

To determine the fast-ion density and time history in the apparatus, the flux of neutral particles emanating from the trapped-ion region is monitored. The fast neutral flux arises from two atomic reactions: (*a*) $H^+ + X^0 \rightarrow H^0 + X^+$ (charge exchange) and (*b*) $H_2^+ \rightarrow H^0 + H^+$. Dissociation of H_2^+ also proceeds by reaction (*c*) $H_2^+ \rightarrow H^+ + H^+ + e^-$, with a probability equal to that of reaction (*b*). Since the liner walls are far from the trapped particles and the orbit diameters are small, it may be assumed that the neutral flux from reactions (*a*) and (*b*) illuminates the liner walls uniformly in azimuth. With this assumption, one may estimate the relative currents of neutrals from reactions (*a*) and (*b*).

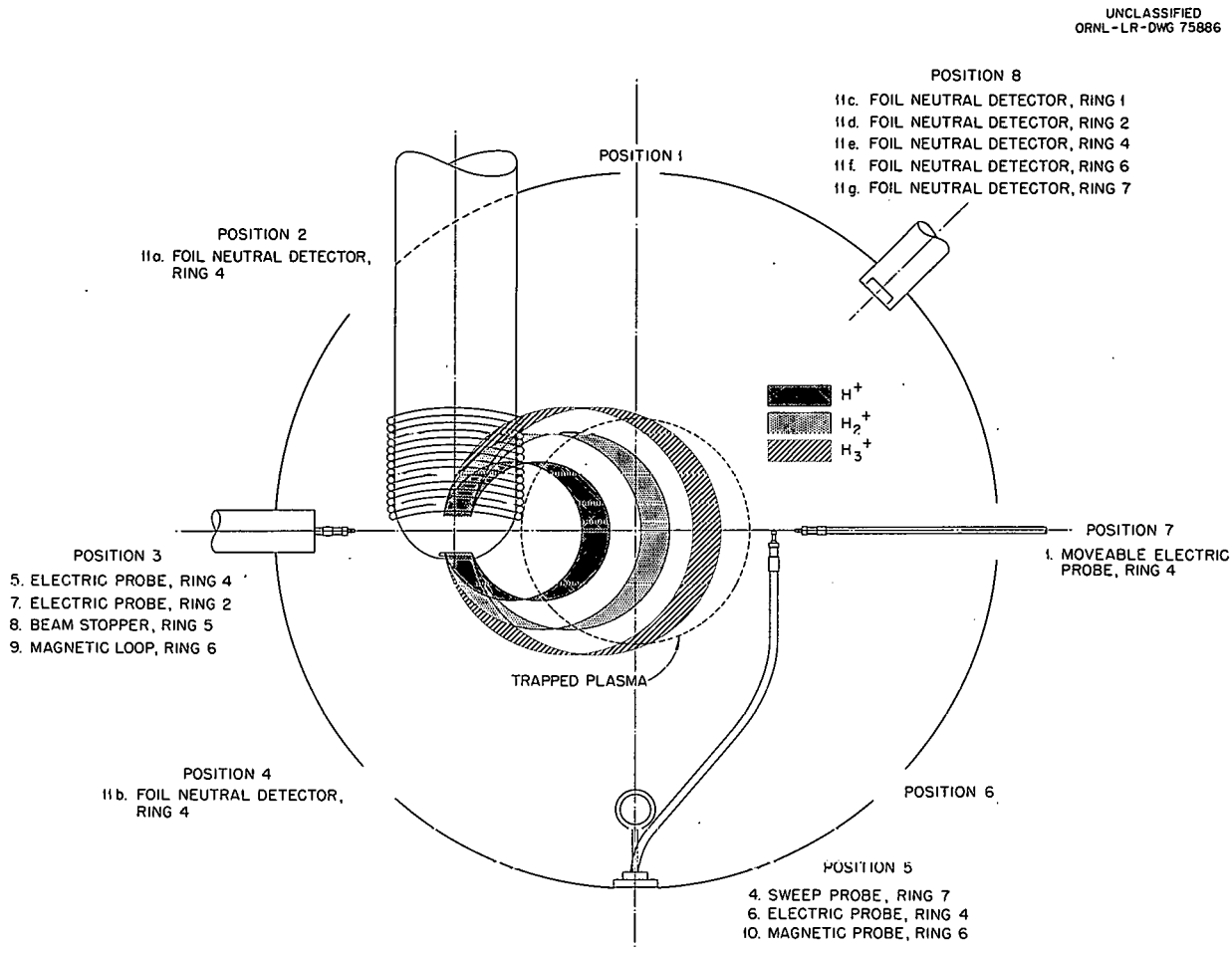

Fig. 2.2. Cross Section of DCX-2, Showing Probe Location and Ion Trajectories. The dotted line shows the expected extent of the permanently trapped H^+ plasma.

Assume that a current, I_D, of H_2^+ is dissociated in DCX-2. Then a neutral current $i_b = \frac{1}{2} I_D$ from direct dissociation will strike the liner walls since reactions (*b*) and (*c*) are equally probable. The current of protons produced will be $\frac{3}{2} I_D$, but only a fraction α of the protons remain in the machine long enough to be lost by charge exchange. They then produce a neutral current $i_a = \frac{3}{2} \alpha I_D$ to the liner walls. The factor α represents the fact that only $\sim\frac{3}{8}$ of the protons are formed in orbits which, upon precession due to the radial magnetic-field gradient, do not intersect the injection snout. It also represents the fact that protons may be lost before charge exchange by other unspecified mechanisms (e.g., instabilities, precession to the walls, etc.). If a neutral current $i_0 = i_a + i_b$ is measured, the fraction of these neutrals due to the charge-exchange protons is $i_a/i_0 = 3\alpha/(1 + 3\alpha)$. For $\alpha = \frac{3}{8}$, $i_a/i_0 = \frac{9}{17}$. Thus, if the beam is turned off, since the molecular-ion lifetime in DCX-2 is ~13 μsec (much shorter than the expected charge-exchange lifetimes), the current of neutrals to the walls after ~30 μsec should drop to approximately $\frac{9}{17}$ of its initial height and should decay at a rate given by

$$i_0 = n_+ n_0 \sigma_x v V ,$$

where σ_x is the charge-exchange cross section, V is the plasma volume, and v is the ion velocity. It must be noted that the neutral-gas and ion densities, n_0 and n_+, are both functions of time

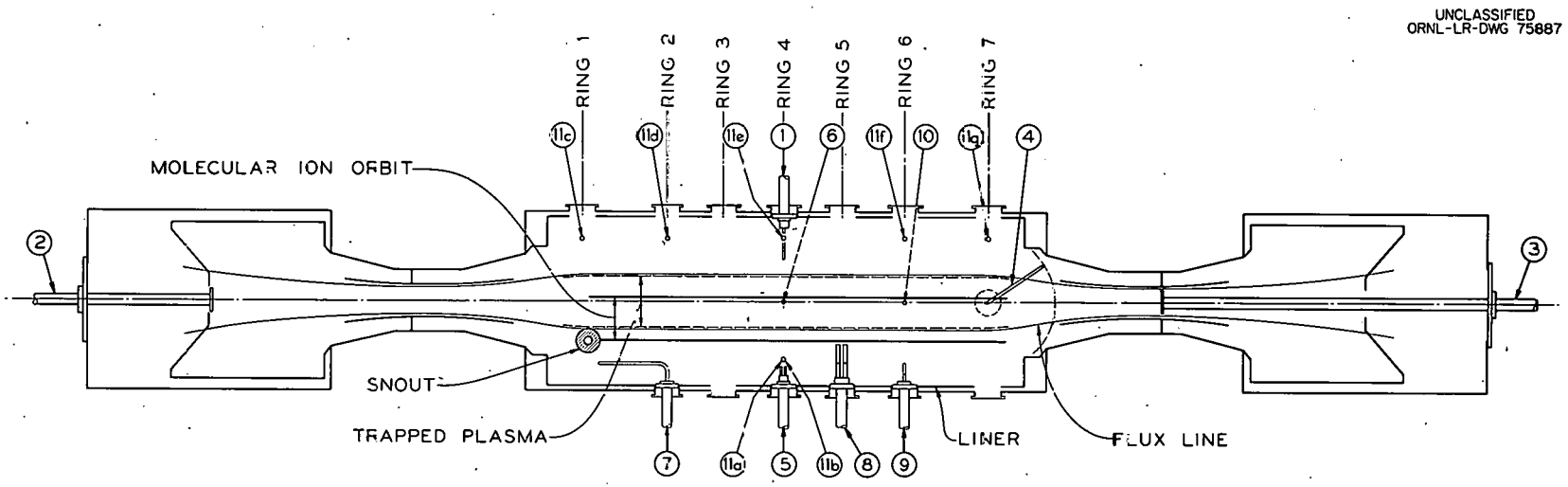

Fig. 2.3. Cross-Sectional View of DCX-2 from Above, Showing the Location of Various Probes. Field lines bounding the plasma region are indicated, as well as the expected region occupied by the molecular ions.

(see Sec. 2.9), and one should not necessarily expect an exponential decay for i_0. The neutral-particle detectors are Faraday cups covered with 10-μin. nickel foils mounted on copper backings photoetched to produce 67% transmission. These detectors are similar to those for use on DCX-1. The current from them is amplified and recorded on the fast-speed multichannel recorder (American Optical Company, Buffalo, N.Y.). The recorder pen speed limits the useful rise time to ~3 milliseconds. The amplifier rise time for the current range in use is ~250 μsec; thus faster information is available by looking at the current signals directly on an oscilloscope. The detectors are mounted close to the liner wall and are distributed parallel to the magnetic axis in the port rings, as shown in Figs. 2.2 – 2.4. Other detectors installed in port ring 4 permit azimuthal correlation of the neutral currents.

A series of runs was made with the coil currents adjusted to produce the magnetic field shown in Fig. 2.1. During these runs the coil current variations due to thermal changes in the generator regulator were monitored and could be limited to ~0.05% (<5 gauss in the "flat" region of the magnetic field). No qualitative variations in the detector currents were seen with deliberate field changes of this magnitude except in ring 7, the farthest probe ring from the injection snout. The beam was keyed on and off, and the currents seen on the various detectors are shown in Fig. 2.5. Upon beam cutoff, a drop in current in the center was seen—obviously much larger than expected. Thus it is immediately apparent that while the beam is on, most of the protons produced are lost from the containment region in a time that is short compared with charge-exchange times. By comparing the initial amplitude of the signal attributed to reaction (*a*) with its expected value, the mean residence time of protons when the beam is on is found to be ~200 μsec. However, soon after the beam is cut off, the loss rate is apparently determined by charge exchange. Experiments are continuing in an attempt to determine the specific mechanism for the proton loss when the beam is on.

From a particle-balance argument, assuming azimuthal symmetry in the machine, the ion density n_+ in the volume viewed by the detector is given by

$$n_+ = \frac{2\pi r_d i_d \tau_x}{A_d A_p},$$

where $\tau_x = (n_0 \sigma_x v)^{-1}$ for neutral-particle density n_0, constant in time, i_d is the current to the detector, r_d is the radial distance to the detector, A_d is the effective area of the detector, and A_p is the cross-sectional area of the plasma.

A typical pulse for a detector in ring 4 yields a density $n_+ \approx 2 \times 10^6/\text{cm}^3$ for an input H_2^+ beam of ~25 ma. The density in ring 7, despite an order-of-magnitude smaller equilibrium signal, is $10^7/\text{cm}^3$. In other cases densities as high as 10^8 have been obtained by slight changes in field.

UNCLASSIFIED
PHOTO 59666

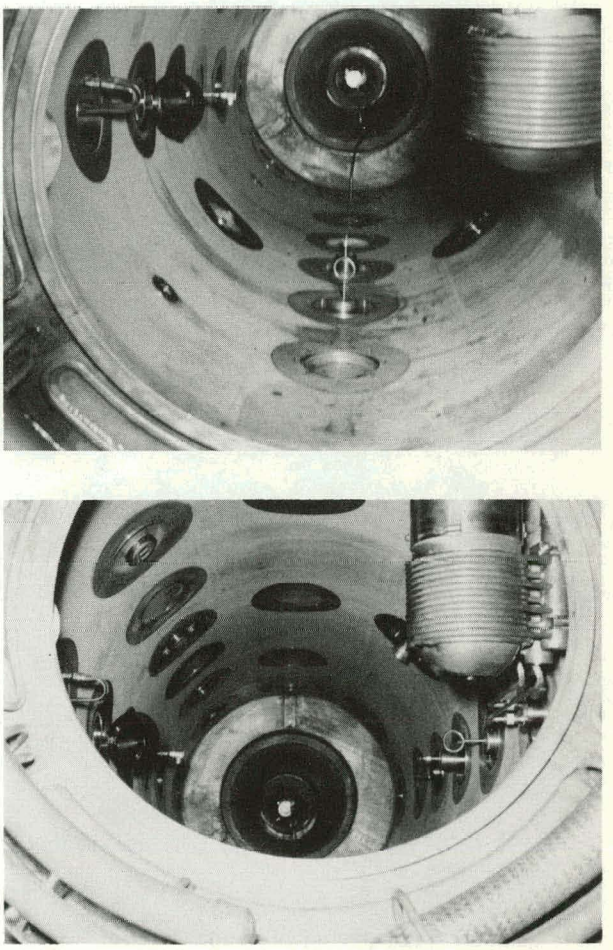

Fig. 2.4. Photographs of the Interior of Central Region of DCX-2.

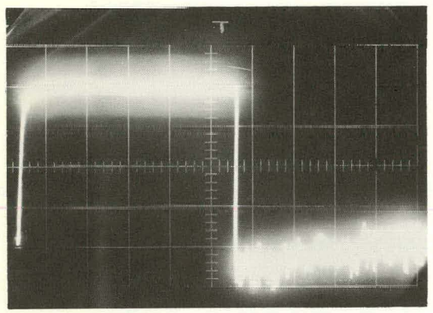

(*a*) RING 1 - 0.05 v/cm

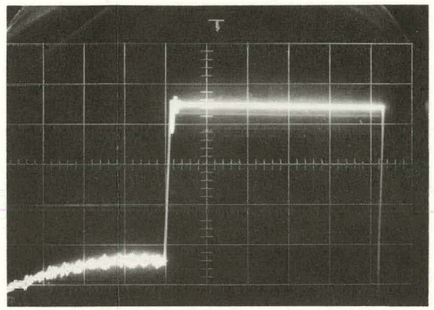

(*c*) RING 2 - 0.5 v/cm

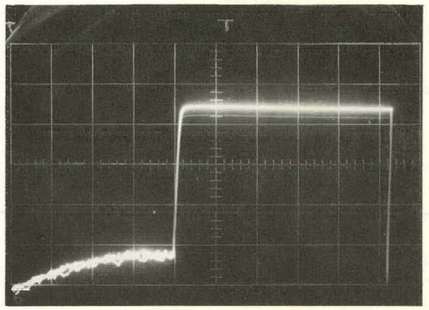

(*d*) RING 4 - 0.5 v/cm

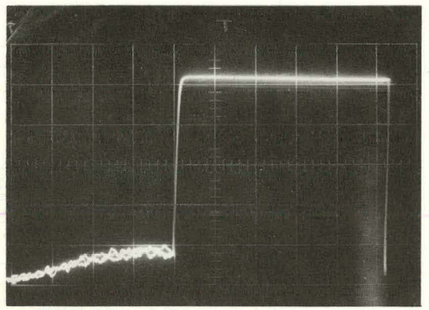

(*f*) RING 6 - 0.5 v/cm

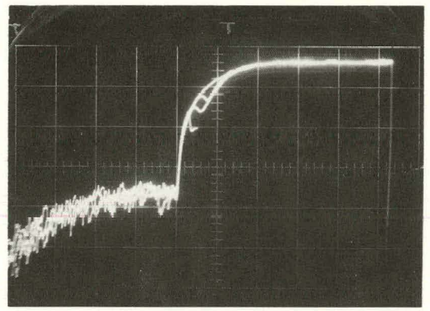

(*h*) RING 7 - 0.1 v/cm

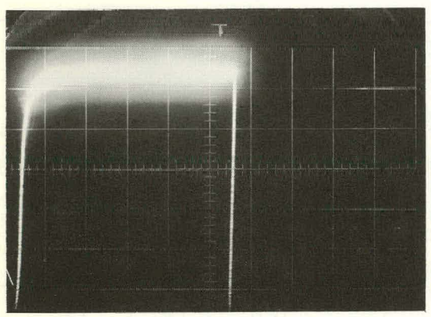

(*b*) RING 1 - 0.01 v/cm

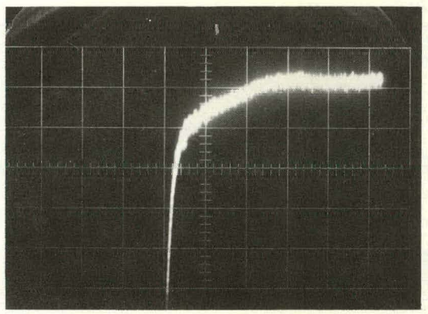

(*e*) RING 4 - 0.01 v/cm

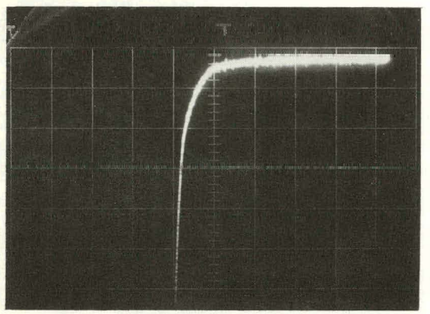

(*g*) RING 6 - 0.01 v/cm

Fig. 2.5. Foil Neutral-Particle Detector Signals at Different Positions Along the Axis of DCX-2. Beam current ~50 ma, pulsed at 10 cps, corresponding to about 10 of the larger horizontal scale divisions; 50% duty cycle. The beam was cut off at the time indicated by the arrows, and the rising traces follow the decay of the signals.

2.6 PLASMA PUMPING

One of the significant features expected upon molecular-ion injection into DCX-2 is the ionization of background gas and the subsequent drift of the cold ions along field lines out of the machine. The pumping speed of fast ions is given by

$$\theta_+ = n_+ \sigma_d v f V ,$$

where θ_+ is in liters per second if V, the plasma volume, is in liters. The factor f is the fraction of ions leaking through the mirrors that do not return to the plasma, and σ_d is the cross section for destruction of neutral gas by fast ions. For orientation, if the background gas were all hydrogen, $\sigma_d = 5 \times 10^{-17}$ cm^2/atom and $\theta_+ = 3.1 \times 10^4$ $(n_+/10^{10})$ liters/sec. This assumes that $V = 100$ liters and $f = 0.8$. For comparison, the conductance for air through the mirrors resulting from the baffles ("venturis") placed along the field lines which just surround the trapped ions was measured as 1500 liters/sec, yielding an inferred pumping speed of 5600 liters/sec for hydrogen.

For the estimates of plasma pumping speed, it was assumed that the electrons produced by ionization are so cold that they add nothing to the ionization rate; this assumption is probably incorrect (see the following).

At the base pressures at which the machine is normally operated, $5–10 \times 10^{-7}$ mm Hg in the liner region, the pressure always rises when a beam is injected. When the beam is pulsed sufficiently slowly, the gas contribution of the beam may be clearly identified from the pressure signal determined by an ion gage whose collector current is amplified and displayed on the multichannel recorder. Unfortunately, it appears that significant amounts of outgassing of the liner, injector duct, target, and probes occur when the beam is turned on. Therefore a measure of ion pumping cannot be simply related to pressure variations at these pressures.

During one run the pressure was raised to a gage value of 5×10^{-6} mm Hg by bleeding air directly into the liner. Upon beam injection (20 ma of H_2^+), the pressure dropped to 3×10^{-6} mm Hg. If it is assumed that the outgassing rate is small compared with the background influx at these pressures, one may obtain an estimate of H^+ density trapped in the machine. Again neglecting electron ionization, $n_+ \cong 10^8/\text{cm}^3$ for a 100-liter plasma volume. For this beam input the foil detectors show a current implying densities of trapped ions of only $2 \times 10^6/\text{cm}^3$. The discrepancy is attributed to ionization by fast plasma electrons.

2.7 RADIO-FREQUENCY SPECTRA

2.7.1 General

The plasma of DCX-2 emits a considerable amount of radio-frequency energy resembling that produced by the DCX-1 and the OGRA plasmas. The radiation consists principally of the harmonics of the molecular- and atomic-ion-cyclotron frequencies. As in DCX-1 and OGRA we interpret the radiation as due to azimuthal clumping of the hot ions rotating in the magnetic field, since the radiation is much too intense to be due to incoherent radiation of ion-cyclotron frequency. A small amount of low-frequency radiation is also emitted, although no strong rotational lines are found (in contrast to OGRA results). Some "white" noise extending above 100 Mc seems also to be present, but the presence of the stronger lines makes the intensity of this radiation less certain.

2.7.2 Ion-Cyclotron Harmonics

The signal received by a short radial probe inserted at any location just inside the wall of the central liner of DCX-2 shows the somewhat complex wave form shown in Fig. 2.6*a*. This, when examined on a faster sweep, is seen to be the proton-cyclotron frequency (18.6 Mc) deeply modulated, although sometimes it is the second harmonic.

A direct examination of the low-frequency content of the probe signal was made by inserting a two-stage RC filter with 2-μsec time constants between the 100-ohm line termination and the oscilloscope. The result is shown in Fig. 2.6*b*. No great regularity of pattern was observed, but the notably spikelike character is clear. When the radial probe was inserted farther into the apparatus, photographs *c* to *f* of Fig. 2.6 were obtained. The direct-current component of these traces is due principally to energetic (hundreds of kev) ions, as shown in Sec 2.8.

The probe signal without the filter was displayed on the same oscilloscope used for the 100-Mc

UNCLASSIFIED
ORNL-LR-DWG 75889

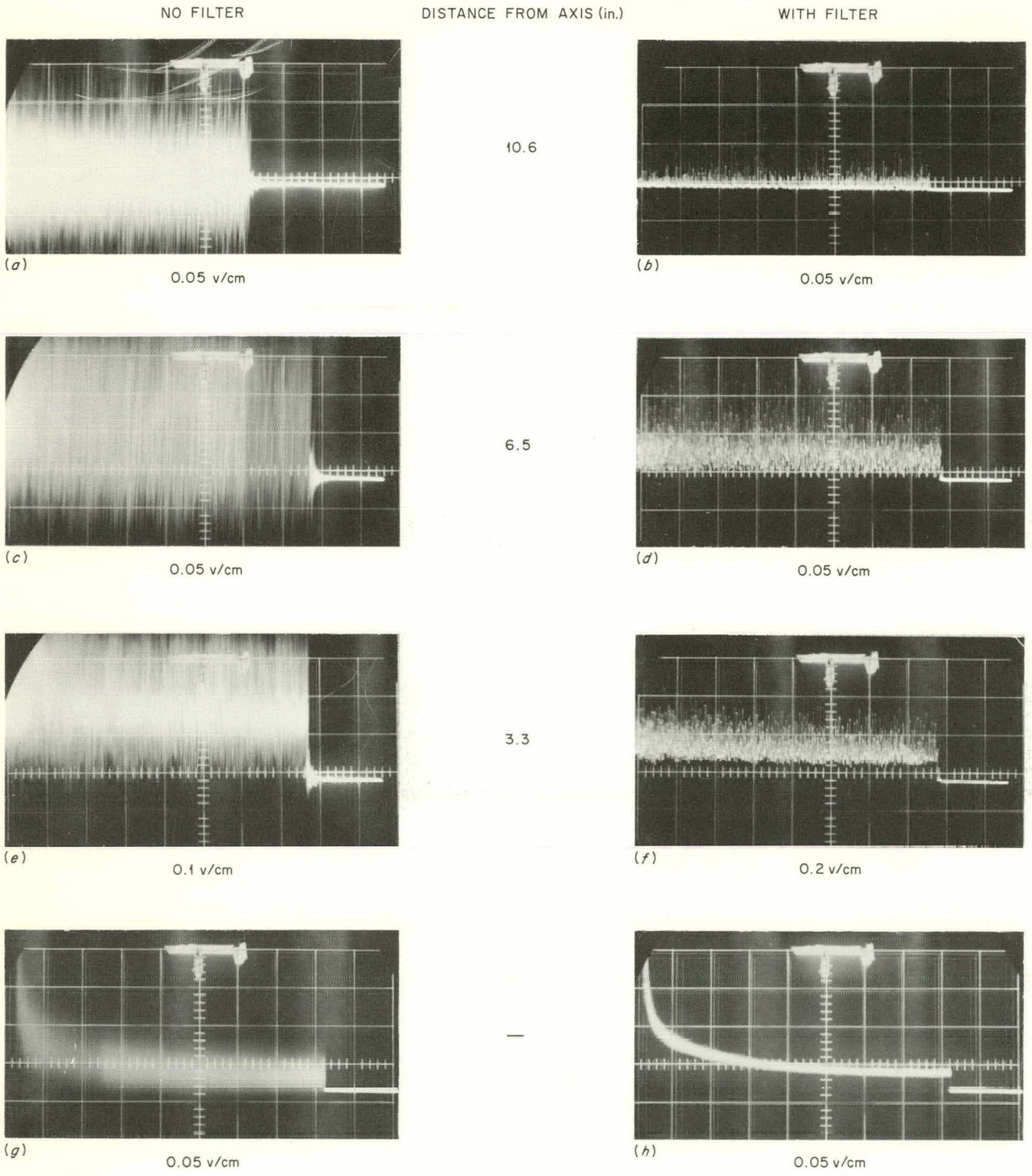

Fig. 2.6. Direct Electric Probe Signals at Various Distances from the Machine Axis, With (*b, d, f, h*) and Without (*a, c, e, g*) Low-Pass Filter. Photographs *g* and *h* are similar traces from a probe in the edge of the molecular-ion beam below the accelerator tube. The H_2^+ beam was turned on at the left-hand end of the trace, left on for 50 msec, and turned off near the right-hand end of the trace.

spectrometer (described below) and photographed with a moving-film camera. This oscilloscope gives 90-μsec sweeps with 10-μsec spaces between, so that almost all of the time scale is seen. Figure 2.7 shows a section of this film just after the beginning of injection. The probe (No. 1) was located with its tip $6\frac{1}{2}$ in. from the axis of DCX-2. At this location none of the trapped H^+ should reach the probe; however, from the measured power and probe characteristics (see Fig. 2.13), it is clear that a considerable number of fast ions do strike the probe. Sweep 2 shows a noticeable current rise for ~50 μsec, although little rf activity has yet become evident. Later the amount of rf energy becomes quite large. Throughout the beam-on interval, strong rises of rf signal, often accompanied by ion current to the probe, can be seen.

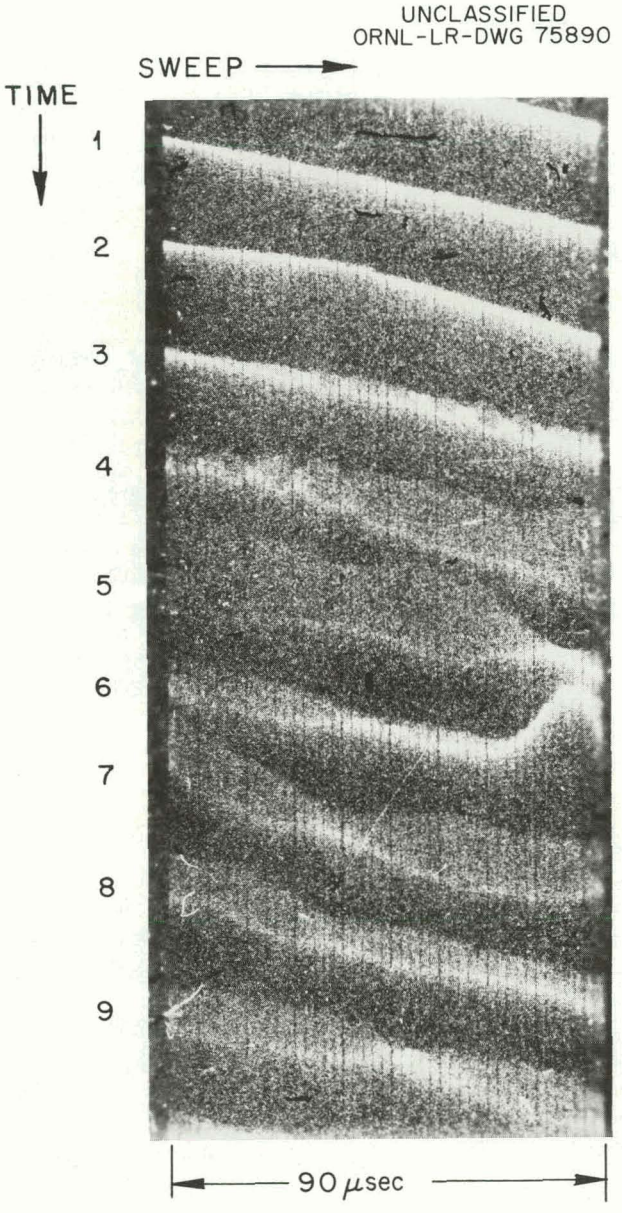

Fig. 2.7. Electric Probe Signals on Moving-Film Camera; Sweep Dead Time About 10 μsec. The low-frequency disturbance that starts on line 4 is typical and is not found if probe is withdrawn to 10 in. from the axis, although the rf signal does not decrease greatly.

The probe signals were analyzed on two rf-spectrum analyzers. A low-frequency analyzer (Panoramic Radio Products, Inc., model SPA-3/25). accepts signals from 0 to 25 Mc with high resolution (bandwidth 1 to 50 kc) and low repetition rate (1 to 60 sweeps/sec).

The spectrum of Fig. 2.8*a*, taken with this spectrometer in the region around zero frequency, shows only a small amount of signal, some of which came from modulation of the injected beam. Figure 2.8*b* shows the most prominent low-frequency line found. This may be due to plasma rotation at 2.2×10^6 rotations/sec but is more likely an impurity ion-cyclotron line, since its frequency is well defined and insensitive to plasma variations. In Fig. 2.8, *c* and *d* show two examples of the (H_2^+) molecular-ion-cyclotron fundamental frequency showing some of its variability; *e* to *g* show similar examples of the H^+-ion-cyclotron fundamental. All these ion lines show width variation from perhaps 12 kc to more than 0.4 Mc. It was noted that the fundamental H^+ line was particularly wide and complex when it was much weaker than its second harmonic.

The second spectrometer is designed to show rapid spectrum variations and can produce a new spectrum every 50 μsec. The coverage is from 10 to 100 Mc with relatively low resolution ($\frac{1}{2}$ to 2 Mc).

Spectra made with this spectrometer from a radial electric probe or an electrostatically shielded magnetic loop with the loop plane perpendicular to the axis of DCX-2 show quite similar features. At high gas pressure (5×10^{-6} mm Hg or more), the spectrum is usually dominated by the second and fourth harmonic of the proton-cyclotron frequency, with a considerable amount of white noise (*a* and *b* of Fig. 2.9). At intermediate pressure, ~ $2–3 \times 10^{-6}$ mm Hg, a variety of spectra can be excited, depending on the beam current and some slight magnetic-field variations.

UNCLASSIFIED
ORNL-LR-DWG 75891

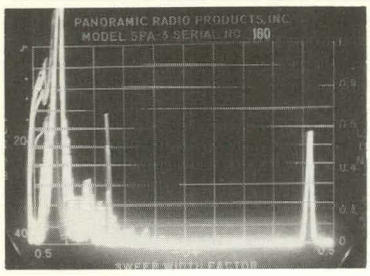

(*a*) 0 TO 0.5 Mc

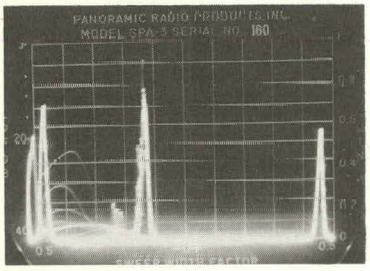

(*b*) 2 TO 2.5 Mc

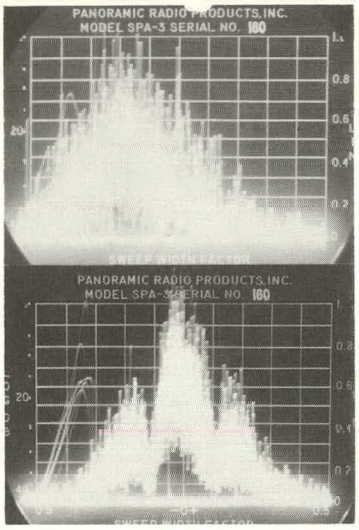

(*c*), (*d*) 3 Mc WIDE NEAR 9 Mc; H_2^+ FUNDAMENTAL

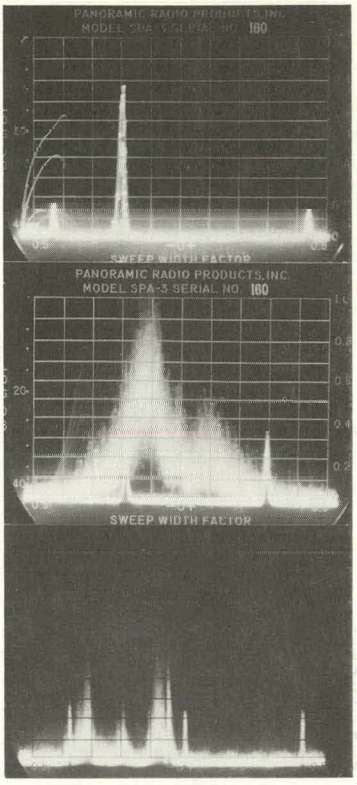

(*e*) 18 TO 18.5 Mc; (*f*), (*g*) 1 Mc WIDE H^+ FUNDAMENTAL

Fig. 2.8. Low-Frequency Spectra. In (*a*) the left peak is a zero frequency; the right is the 0.5-Mc marker; in (*b*) the left and right peaks are 0.5-Mc markers. The small sharp peaks in other traces are similar markers.

UNCLASSIFIED
ORNL-LR-DWG 75892

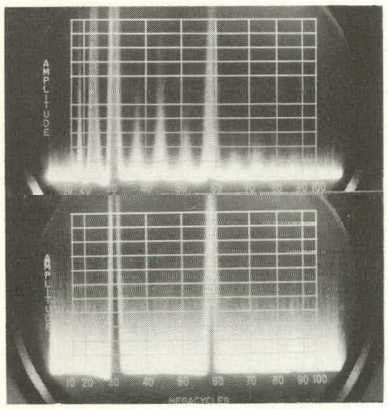

(*a*) 10^{-5} mm Hg
(*b*) 10^{-5} mm Hg

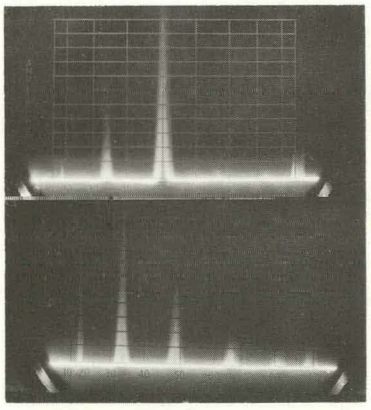

(*c*) 3×10^{-6} mm Hg
(*d*) 3×10^{-6} mm Hg

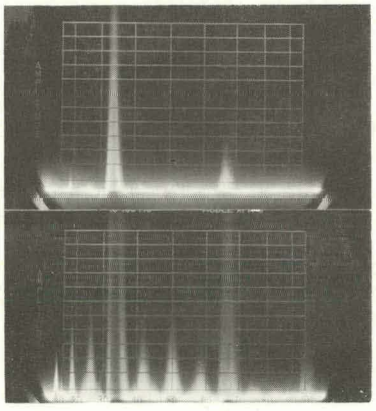

(*e*) LOW GAIN, 3×10^{-6} mm Hg
(*f*) HIGH GAIN, 3×10^{-6} mm Hg

Fig. 2.9. Spectra from 0 to 100 Mc. The amplitude scale is approximately linear. The frequency scale is nonlinear, with vertical lines approximately at each 10 Mc starting at 10 Mc.

Figure 2.9*c* shows a spectrum with the H^+ third harmonic as the strongest radiation; Fig. 2.9*d* shows a regular succession of diminishing intensity of adjacent harmonics, whereas *e* and *f* were taken in rapid succession with a considerable increase of spectrometer gain. This spectrum, like those observed at high pressure, has the H^+ second and fourth harmonics dominant, but the white noise is weak and the other H^+ harmonics are weakly visible. In addition, the odd harmonics of H_2^+ can be seen between the H^+ lines. These odd harmonics of the molecular ion in all the examples studied show a much more regular change of relative intensity vs harmonic number or absolute intensity than do the harmonics of H^+. Although the H^+ lines have the same frequency as the even harmonics of H_2^+, it seems probable that they come largely from a different source (H^+), judging from their generally greater intensity and independent variability.

At gas pressures from 8×10^{-7} to 1.5×10^{-6} mm Hg, the harmonics of H_2^+ are relatively stronger than at high pressures, but they are still ~10–100 times weaker than the H^+ lines. Spectra were taken with various amounts of attenuation between the antenna and the analyzer to make sure that the harmonics were genuine and not generated in the spectrometer converter. It was found that internal generation was small in most cases, but care must be taken, because a harmonic lower than a few percent of a fundamental cannot be trusted without subtraction of internal harmonics. The peaks seen on the spectrometer seem quite steady when the beam is left on continuously. Figure 2.10 is such an example. Note that the space below some of the peaks is dark, showing that the line usually was present whenever the spectrometer swept by this frequency; however, some of the lines are not open below, showing strong modulation.

The moving-film camera was used to photograph the oscilloscope of the 100-Mc spectrometer; a section of this film is shown in Fig. 2.11. Extremely rapid variations of the various lines were observed, showing that the rotating charge clumps are formed often in 100 μsec or less. The lines often show equally rapid disappearance, but this should not be associated with the dissipation of the charge clumps, since it is only necessary for another clump to form in the appropriate place for the reduction or elimination of one of the harmonic lines. When the beam is turned off, the harmonics decay in several hundreds of microseconds.

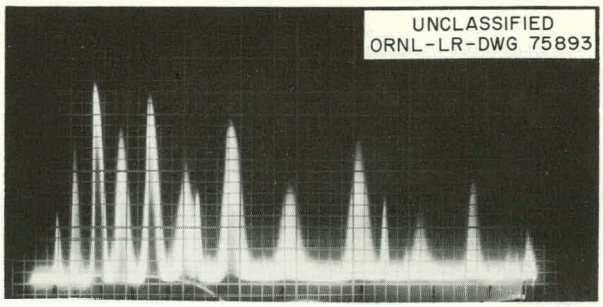

Fig. 2.10. Spectrum (0 to 100 Mc) With Constant Ion Beam. Note that some of the peaks are open below while others are not. The amplitude scale is logarithmic with seven small divisions for a factor of 10, except at small amplitudes.

2.7.3 Phase Relations of the Radio-Frequency Signals

An attempt was made to observe phase relations between the rf signals seen on various probes. An oscilloscope was equipped with *X* and *Y* deflection amplifiers having approximately equal phase shifts from 0 to 40 Mc.

Adjacent probes in the same housing (~3 cm apart) were examined, with the result shown in Fig. 2.12*a*. This is a clear in-phase relation despite the strong modulation of the signals. Figure 2.12*b* shows a similar pattern obtained between a probe near the machine midplane (No. 5, ring 4) and one near the injection snout (No. 7, ring 1). When the injected beam current was increased, the pattern of Fig. 2.12*c* appeared. This pattern could result either from a phase shift of 90°, giving essentially a circular pattern, or from a randomly varying phase relation. A section of cable corresponding to $\frac{1}{4}$ wavelength (90° phase shift) was added to one signal channel. This should have transformed a 90° pattern to a 0 or 180° pattern. No change was obtained, showing that a random phase pattern was occurring. At the same time, rf spectra show a marked increase in the H^+ second and fourth harmonics. Comparison of signals from probe No. 1 on the south side of the axis and probe No. 5 on the north side, both in ring 4, shows the pattern in Fig.

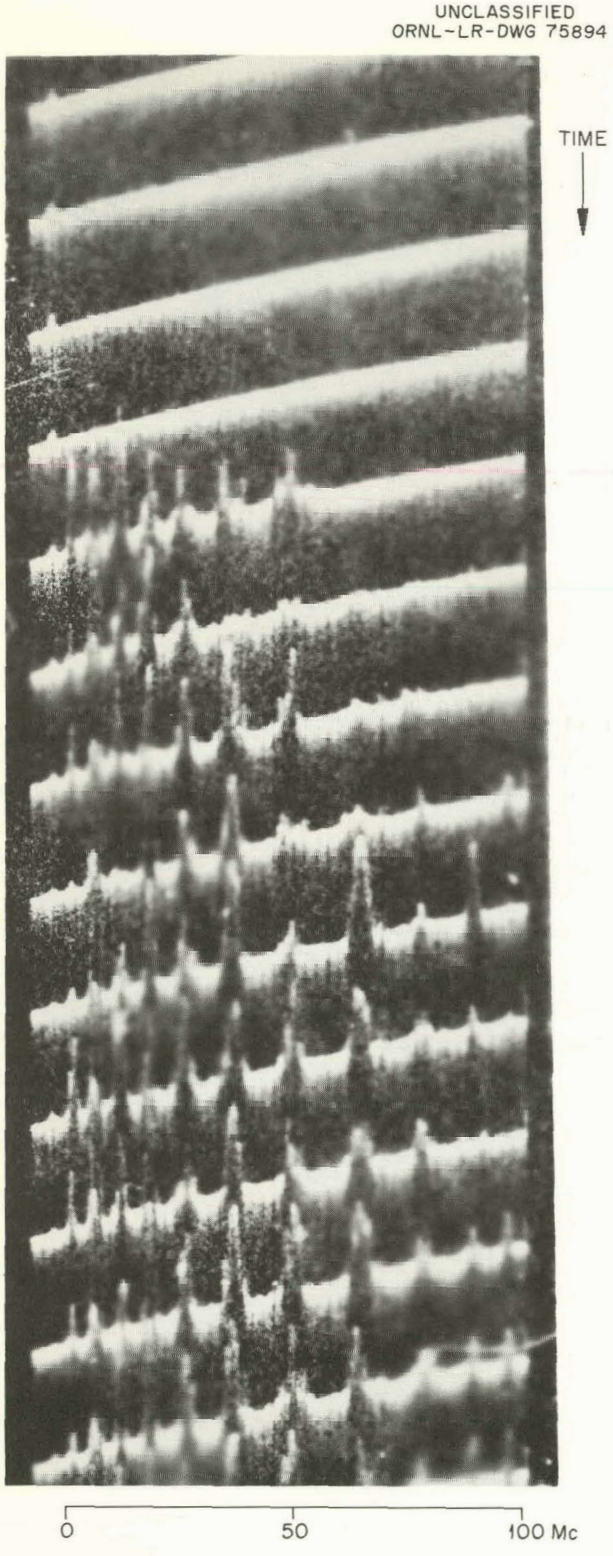

Fig. 2.11. Moving-Film Picture of 0- to 100-Mc Spectrum, Showing Rapid Beginning of RF and Rapid Variation of Harmonic Amplitude.

2.12*d* with the beam current as for Fig. 2.12*a*. This is clearly a 180° pattern, showing alternation or rotation of the charge distribution producing the rf signals.

2.8 PROBE CHARACTERISTICS

A movable probe was used in an attempt to define the radial distribution of the plasma near the midplane (ring 5). Langmuir probe characteristics using up to ~900 v were taken to separate fast-ion and cold-plasma effects. The cold plasma observed on this probe is characteristic of ions and electrons of the order of several hundred electron volts. Also, flow and differential-temperature measurements were made on the cooling water to determine the power input to the probe.

Figure 2.13 shows the probe construction. It may be noted that the current was measured on a region limited to the tip of the probe. However, the same water cooled the entire area of the probe extending into the plasma, and the power incident on the probe could have fallen anywhere on this area.

To estimate the contribution of energetic ions, the current amplitude was measured from the Langmuir characteristic at a voltage presumed to be the floating potential associated with the cold plasma. To establish this point, the probe was moved out sufficiently far radially to reduce the fast-ion current to a negligible amount. The floating potential was determined at this point. The potential was assumed not to vary as a function of radius. This assumption seems reasonable, because no evidence for plasma rotation has been found corresponding to radial electric fields greater than a few volts per centimeter.

Figure 2.14 shows the observed current as a function of radius. The radial limit defined by the injector position is also indicated. It is clear that considerable current is seen outside this radius.

A plot of the power incident on the probe per unit radial distance as a function of radius is also shown in Fig. 2.14. Some of the probe characteristic curves that correspond to the region covered by the current and power plot of Fig. 2.14 are shown in Fig. 2.15.

Probe characteristics were also obtained for probes at each end of the machine beyond the mirrors (Nos. 2 and 3) and for the sweep probe

UNCLASSIFIED
ORNL-LR-DWG 75895

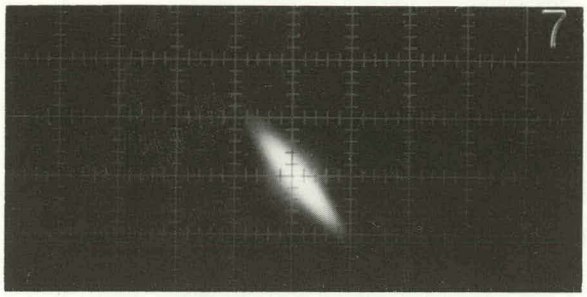

(*a*) ADJACENT PROBES

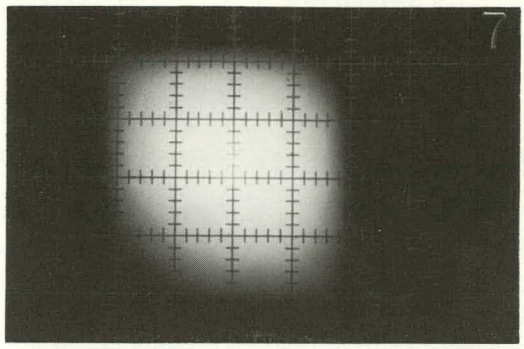

(*c*) SAME PROBES AS (*b*) BUT AT LARGER INJECTION BEAM CURRENT

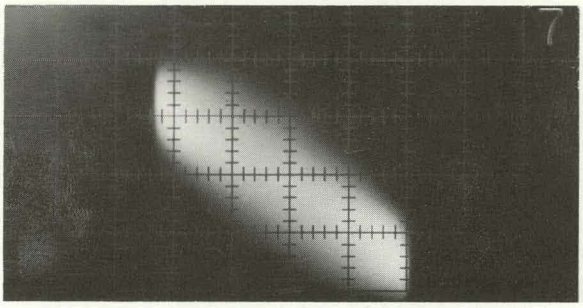

(*b*) PROBE NO. 5 VS PROBE NO. 7 SEPARATED AXIALLY BUT AT THE SAME AZIMUTH

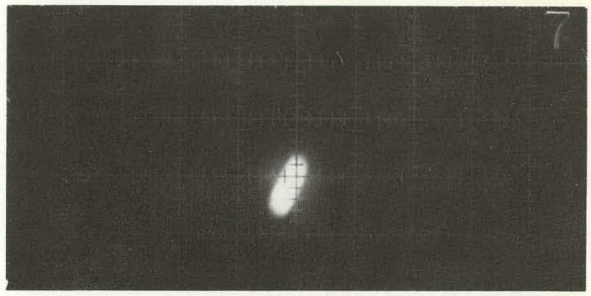

(*d*) PROBE NO. 1 VS PROBE NO. 5 ON OPPOSITE SIDES OF THE PLASMA BUT AT THE SAME AXIAL POSITION

Fig. 2.12. Comparison of Phases of the RF Signals on Different Probes. The pattern of (*c*) is due to randomly varying phase relation and not to a 90° relation.

UNCLASSIFIED
ORNL-LR-DWG 75896

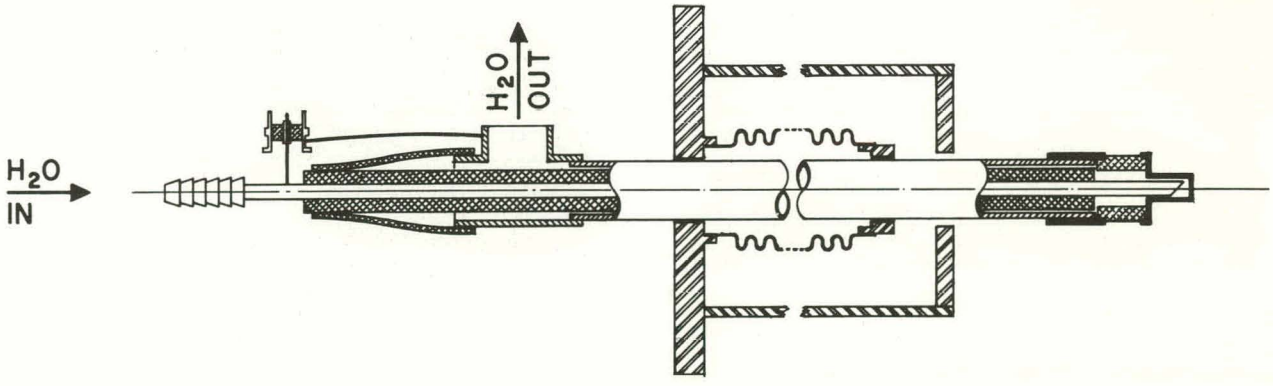

Fig. 2.13. Movable RF Probe No. 1 with Water Cooling.

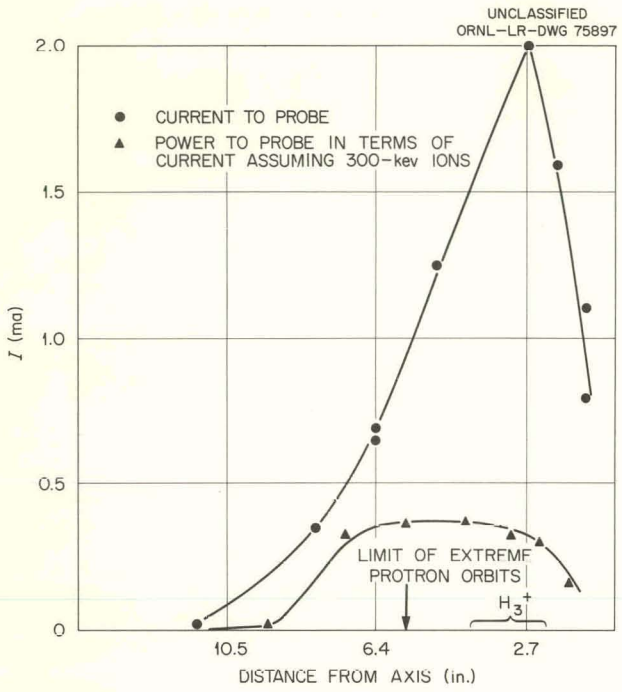

Fig. 2.14. Current to a Probe and Current of 300-kev Particles That Would Give the Measured Power as a Function of Radial Position. The expected edge of the trapped plasma and the zone that would be occupied by the H_3^+-ion beam (if any) are indicated.

(No. 4), which moves in an arc intersecting the machine axis well inside the mirrors but just enough beyond the field dip so that fast molecular ions and protons should not reach it unless they are spread by some mechanism in the plasma. Figure 2.16 shows characteristics from the three probes. The end probes have similar characteristics and show electron and ion "temperatures" of less than 1 kev but not less than a few hundreds of electron volts. Note that the ion and electron saturation currents are about equal, a condition that is expected because cold ions and electrons should be ejected through the mirrors at equal rates, the plasma potential adjusting itself to maintain this condition. This result indicates that no major loss of cold ions and electrons occurs elsewhere unless in balanced numbers. The sweep probe shows a much different result. The low ion and high electron saturation currents resemble an ordinary plasma of very cold ions and electrons of about 160 ev in temperature.

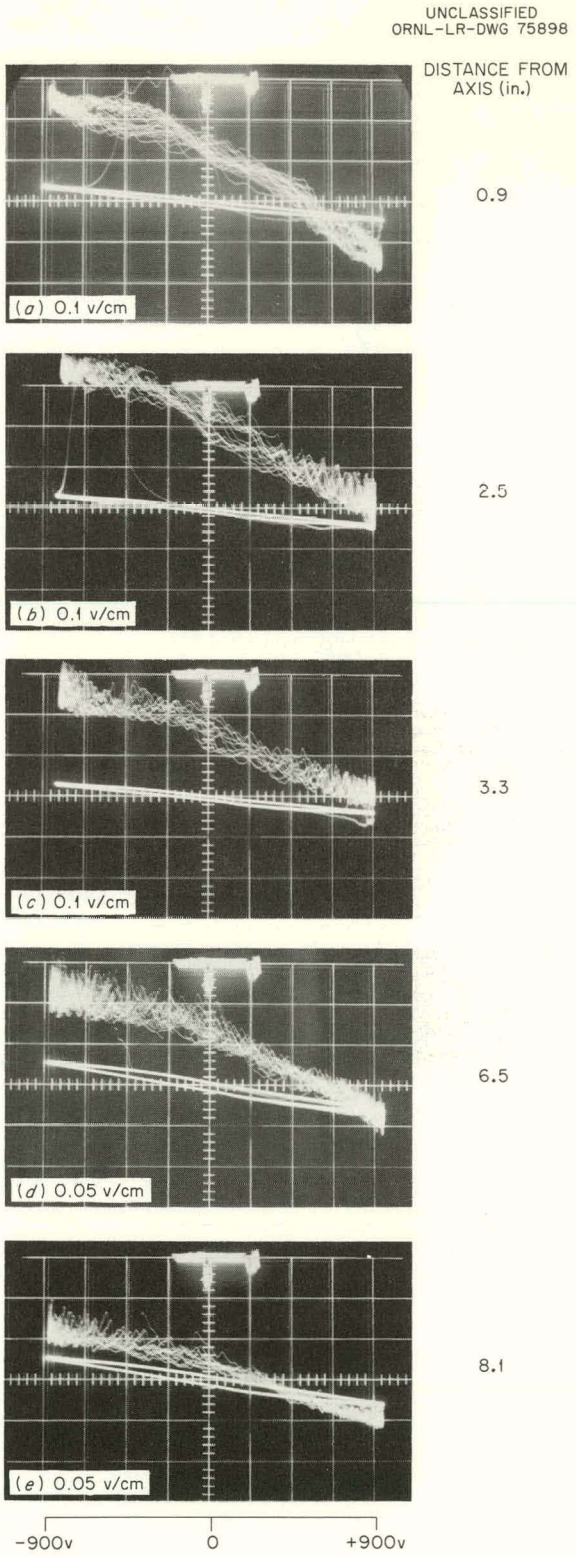

Fig. 2.15. Probe Characteristics at Various Radii. The ion-beam current was 50 ma, and the pressure was approximately 9×10^{-7} mm Hg.

UNCLASSIFIED
ORNL-LR-DWG 75899

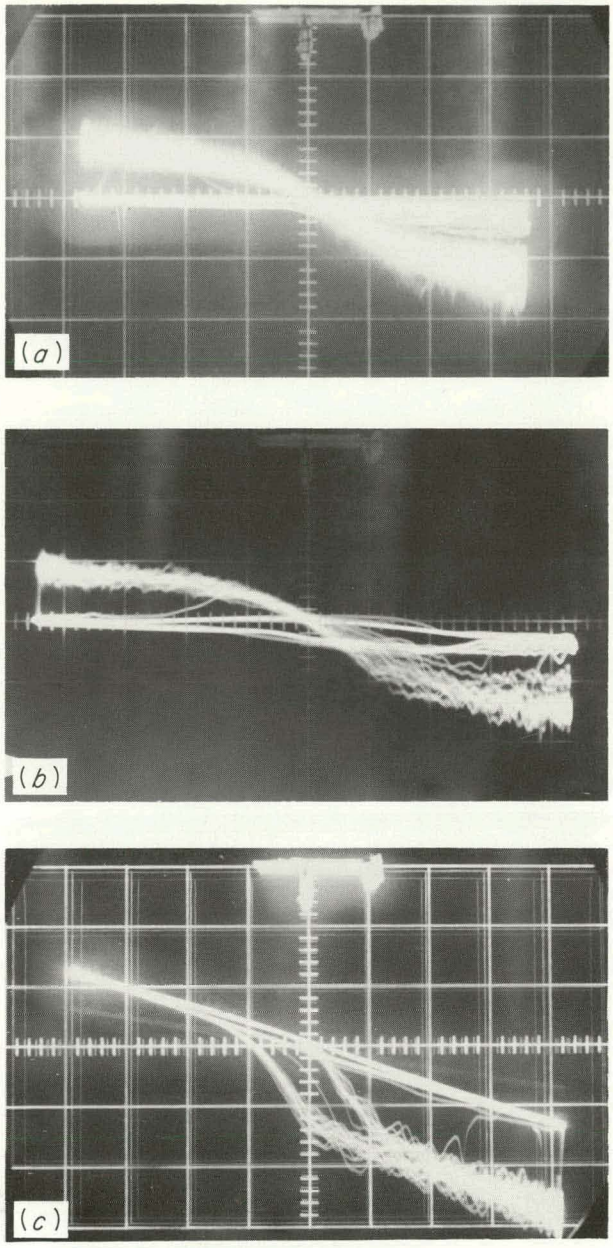

Fig. 2.16. Probe Characteristics. Trace *a* is from the east electric probe, No. 2; *b* is from the west electric probe, No. 3; *c* is from the sweep probe, No. 4. The slanted baseline in this trace results when the beam is turned off and is caused by ohmic leakage in the probe cooling water. The displacement of the two beam-on traces is due to a small phase shift in the applied alternating voltage.

2.9 TIME BEHAVIOR OF FAST IONS

The time behavior of the fast-ion plasma in DCX-2 has been calculated in the regime in which the losses are expected to be limited by charge exchange. It was assumed that the injected current of molecular ions was lower than the upper critical current, I_{uc}, and that the base pressure was sufficiently low to ensure that the principal gas influx arose from the injected beam. The particle-balance equations can be written

$$\Omega \frac{dn_0}{dt} = \Gamma I - n_0\theta_0 - n_0 n_+ \sigma_d v f V , \qquad (1)$$

$$\Omega \frac{dn_r}{dt} = N_r\theta_r - n_r\theta_r - n_r n_+ \sigma_d v f V , \qquad (2)$$

$$\frac{dn_+}{dt} = \frac{I}{V}(\sigma_B \mathfrak{L} n_+ + n_0 \sigma_{B0} \mathfrak{L}) - n_0 n_+ \sigma_x v - n_r n_+ \sigma_{xr} v , \qquad (3)$$

where Ω is the liner volume inside the mirrors, n_r is the residual-gas density, N_r is the residual-gas density with no beam injected, and θ_i represents a pumping speed for the gas component i in the appropriate units. The remaining notation follows that of Mackin:[2] the subscripts B and d refer to breakup of molecular ions and ionization or charge exchange of the gas by atomic ions; V is the plasma volume, v is the ion velocity, and f is the plasma pumping efficiency; Γ represents the number of particles pumped per molecular-ion incident, and $\mathfrak{L}$ is the path length of the molecular ions through the plasma. Upon beam turnoff, the supply terms ΓI in Eq. (1) and I/V $(\sigma_B \mathfrak{L} n_+ + \sigma_{B0} n_0 \mathfrak{L})$ in Eq. (3) are set to zero. Then Eqs. (1) to (3) may be rewritten

$$\frac{d\eta_0}{dt} = -\eta_0\eta_+ \frac{1}{\tau_0} - \eta_0\left(\frac{\theta_0}{\Omega}\right), \qquad (4)$$

$$\frac{d\eta_r}{dt} = -\eta_r\eta_+ \frac{1}{\tau_r} - \eta_r\left(\frac{\theta_r}{\Omega}\right) + \frac{1}{\tau_r} + \left(\frac{\theta_r}{\Omega}\right), \qquad (5)$$

$$\frac{d\eta_+}{dt} = -\eta_+\eta_r \frac{1}{\tau_{xr}} - \eta_+\eta_0 \frac{1}{\tau_{x0}} , \qquad (6)$$

[2] R. J. Mackin, Jr., *Nucl. Fusion* **1**(2), 131 (1961).

where the η_i are the respective densities relative to their values at beam turnoff (time zero),

$$\tau_0 = \frac{\Omega}{n_+(0)\sigma_{d0}vVf} = 70 \text{ milliseconds for } n_+(0) = 10^{10}/\text{cm}^3 ,$$

$$\tau_r = \frac{\Omega}{n_+(0)\sigma_{dr}vVf_r} = 23 \times \left(\frac{f}{f_r}\right) \text{milliseconds} ,$$

$$\frac{\Omega}{\theta_0} = 560 \text{ milliseconds} , \qquad (7)$$

$$\frac{\Omega}{\theta_r} = 2100 \text{ milliseconds} ,$$

$$\tau_{x0} = (n_0(0)\sigma_{x0}v)^{-1} = 250 \text{ milliseconds} ,$$

$$\tau_{xr} = (n_r(0)\sigma_{xr}v)^{-1} = 6900 \text{ milliseconds} .$$

The cross sections were taken from ORNL-3113[3] at the energies appropriate to the DCX-2 experiment. The residual-gas cross sections were taken for CO. The plasma volume V was taken as 100 liters and the liner volume Ω as 2100 liters. The pumping speed θ_0 was taken as 4000 liters/sec and θ_r as 1000 liters/sec. The measured pumping speed quoted earlier was carried out with slightly larger isolation tubes (venturis) in the mirror throats than originally designed. The value of $n_r(0)$ corresponds to the residual-gas density at beam cutoff for a base pressure of 10^{-7} mm Hg.

Equations (4) to (6) may be combined to yield the time behavior of η_0, η_+, and η_r by examining three parts of the decay, in each of which some of the quantities may be neglected. For example, immediately following beam turnoff, because of the higher ionization cross section for residual gas other than hydrogen and the assumed initially lower residual-gas density, one may neglect the residual gas contribution to charge exchange. Then, combining Eqs. (4) and (6) and integrating, one obtains

$$\eta_0 = \left(1 - \frac{\tau_0}{\tau_{x0}}\right) \frac{e^{-[(1/\tau_0)-(1/\tau_{x0})]t}}{1 - \frac{\tau_0}{\tau_{x0}} e^{-[(1/\tau_0)-(1/\tau_{x0})]t}} , \qquad (8)$$

[3] C. F. Barnett, W. B. Gauster, and J. A. Ray, *Atomic and Molecular Collision Cross-Sections of Interest in Controlled Thermonuclear Research*, ORNL-3113 (1961).

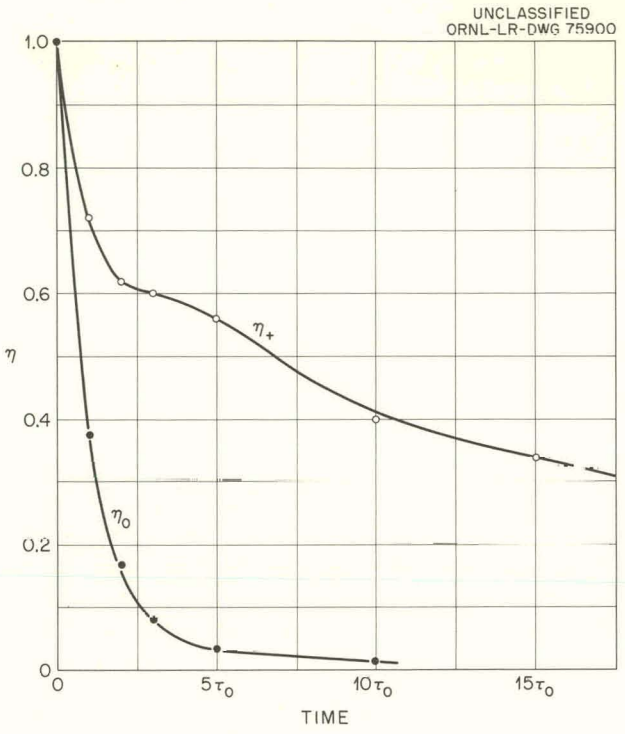

Fig. 2.17. Decay of the Normalized Fast-Ion Density (η_+) and the Normalized Hydrogen Gas Density (η_0) as a Function of Time (in Units of the Time Required To Pump Out the Hydrogen at the Initial Rate) After Beam Turnoff.

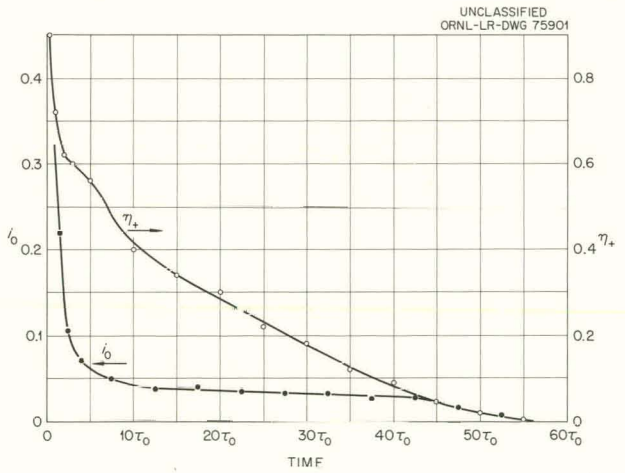

Fig. 2.18. Decay of the Normalized Fast-Ion Density (η_+) and the Fast Charge-Exchange Neutral-Particle Flux (i_0) as a Function of Time After Beam Turnoff.

$$\eta_+ = \left(1 - \frac{\tau_0}{\tau_{x0}}\right) \frac{1}{1 - \frac{\tau_0}{\tau_{x0}} e^{-[(1/\tau_0)-(1/\tau_{x0})]t}} . \quad (9)$$

The current of charge-exchange neutrals is

$$\eta_+ \eta_0 \frac{1}{\tau_{x0}} = \frac{d\eta_+}{dt} = \frac{1}{\tau_{x0}} \left(1 - \frac{\tau_0}{\tau_{x0}}\right)^2 \times \frac{e^{-[(1/\tau_0)-(1/\tau_{x0})]t}}{\left(1 - \frac{\tau_0}{\tau_{x0}} e^{-[(1/\tau_0)-(1/\tau_{x0})]t}\right)^2} . \quad (10)$$

Similarly, after a sufficient number of decay constants of η_0, one may neglect the hydrogen contributions to the charge-exchange loss and combine Eqs. (5) and (6) to obtain $\eta_r(t)$ and $\eta_+(t)$. The intermediate region, where the residual-gas and hydrogen contributions to charge-exchange losses must both be considered, has been solved by stepwise integration of Eqs. (4) to (6) and joined onto the other regimes. The overall results are shown in Figs. 2.17 and 2.18. The results are plotted for the set of parameters given in Eqs. (7) and for a current and path length to yield the ion density of $10^{10}/cm^3$ at beam turnoff.

The experimental results show, as mentioned earlier, a plasma density lower than the value expected for a charge-exchange-dominated loss mechanism. However, since the time behavior following beam turnoff shows no unexpected losses, the theory may be applied. The regime exhibits an initial density sufficiently low that $1/\tau_0 \ll \theta_0/\Omega$. Therefore,

$$\eta_0 = e^{-(\theta_0/\Omega)t} . \quad (11)$$

Equation (6) may be integrated to yield

$$\ln \eta_+ = -\int \eta_r \frac{dt}{\tau_{xr}} - \frac{\theta_0/\Omega}{\tau_{x0}} e^{-(\theta_0/\Omega)t} . \quad (12)$$

This reduces to

$$\eta_+ = e^{-[(1/\tau_{x0})+(1/\tau_r)]t} , \quad (13)$$

if the time dependence of η_r may be neglected and $\theta_0 \ll 1/\tau_{x0}$. These conditions correspond to the situation in DCX-1 and to the operating regime in DCX-2 in which the plasma density is sufficiently low that it does not result in significant plasma pumping by ions. The approximate exponential fall of the current to the foil detectors reflects the fact that the plasma pumping speed is small, which sustains the argument for the enhanced rate of loss of fast ions when the beam is being injected.

3. Plasma Physics

3.1 ELECTRON-CYCLOTRON HEATING IN THE PHYSICS TEST FACILITY

3.1.1 Neutron Production from a Steady-State Electron-Heated Deuterium Plasma

W. B. Ard — H. O. Eason
M. C. Becker[1] — A. C. England
R. A. Dandl — R. J. Kerr

In previous semiannual reports,[2-4] experiments have been described in which microwave power sources have applied up to 1 kw continuous wave of power to a plasma at 2.4 and 9.2 gc (gigacycles). The power has been applied to a cavity in a magnetic-mirror geometry at the electron-cyclotron frequency. During the period of this report, a continuous-wave microwave power source capable of applying up to 5 kw of 10.8-gc microwave power to the plasma became available. Figure 3.1 shows the current experimental arrangement of the Physics Test Facility (PTF).

With the application of 2 kw of power, neutron emission from the plasma was observed with deuterium-gas feed and validated by foil activation measurements. With the plasma adjusted for

[1] Instrumentation and Controls Division.

[2] *Thermonuclear Div. Semiann. Progr. Rept. Jan. 31, 1961*, ORNL-3104, sec 3.1.

[3] *Thermonuclear Div. Progr. Rept. Oct. 31, 1961*, ORNL-3239, sec 3.1.

[4] *Thermonuclear Div. Semiann. Progr. Rept. Apr. 30, 1962*, ORNL-3315, sec 3.1.

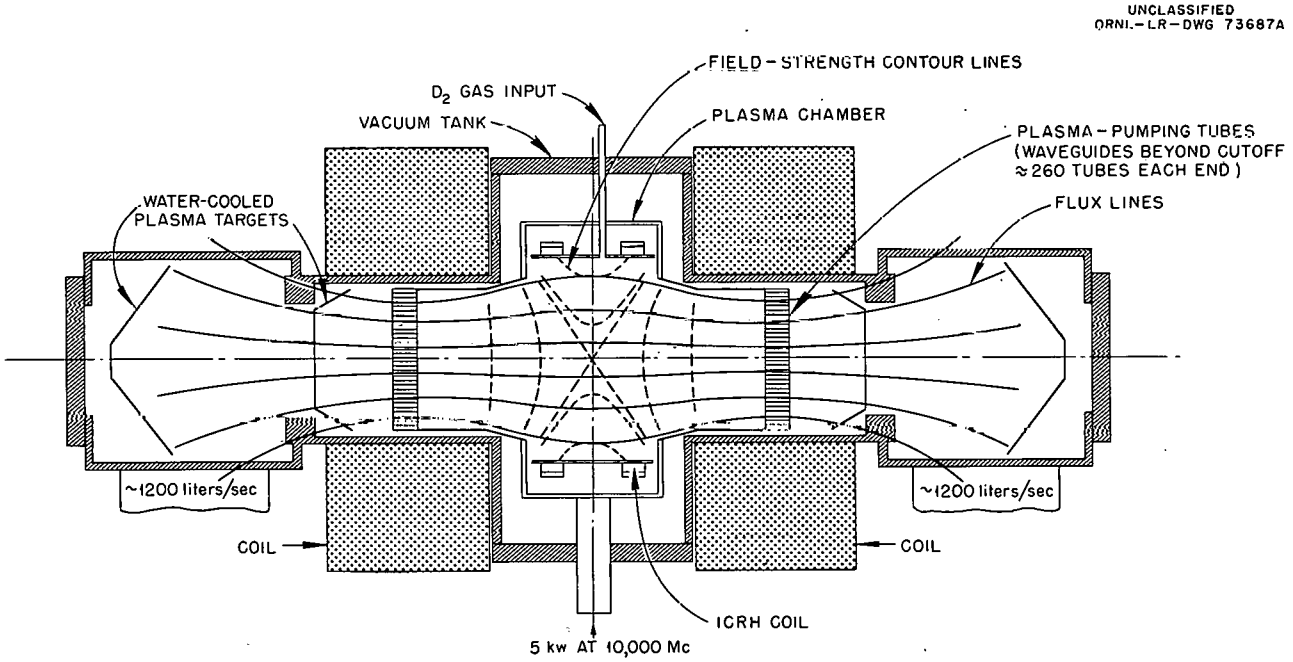

Fig. 3.1. Schematic Diagram of Electron-Cyclotron Heating Experiment.

quiescent steady-state operation, the neutron production rate is also optimum. With the plasma adjusted for noisy unstable operation, the neutron production rate is sharply decreased.

The initial determination of the source strength of the neutrons was made with a U^{235} fission chamber. This detector indicated a source strength of $\sim 10^5$ neutrons/sec at 2 kw of microwave power when calibrated against a known Am-α-B neutron source. Further checks with an He^3 proportional counter showed that the neutron source strength increased roughly as the square of the applied microwave power, as shown in Fig. 3.2. (The

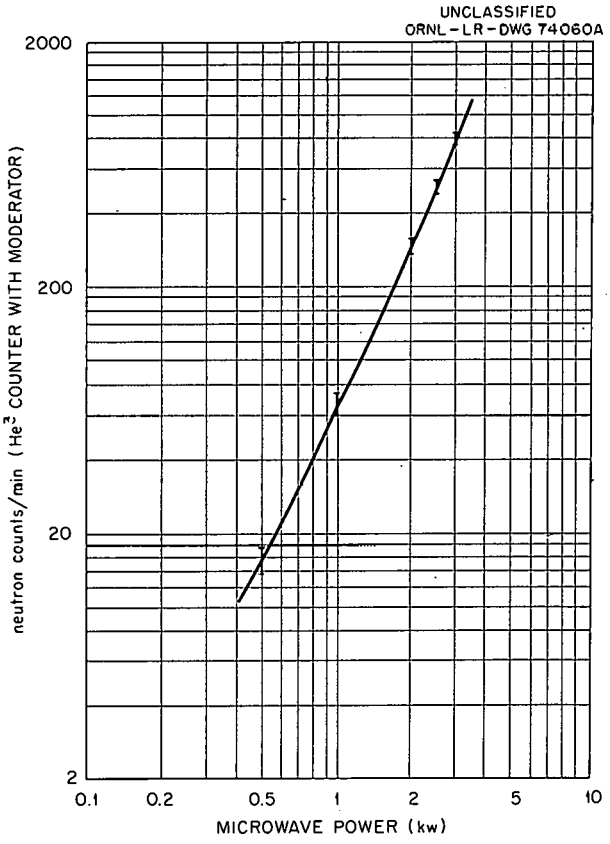

Fig. 3.2. Neutron Counting Rate as a Function of Microwave Power.

He^3 counter detects neutrons through the reaction $He^3(n,p)T$ with a Q of approximately +770 kev.)

Measurements of the 8-mm microwave noise amplitude and diamagnetic signal from an axial Hall probe showed a similar dependence on microwave power, as shown in Fig. 3.3. The neutron

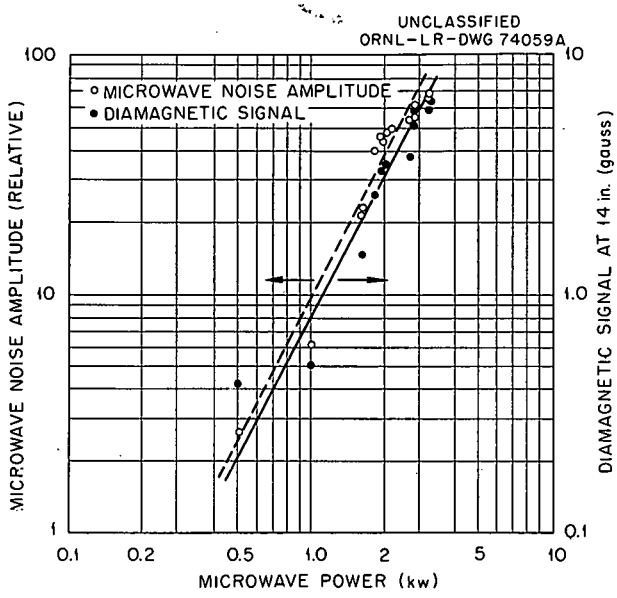

Fig. 3.3. Eight-Millimeter Microwave Noise Amplitude and Diamagnetic Signal as a Function of Microwave Power.

production took place only in a fairly narrow range of magnet current variation. Figure 3.4 shows the neutron counting rate and 8-mm microwave noise amplitude as a function of magnet current. The region of enhanced neutron emission and maximum

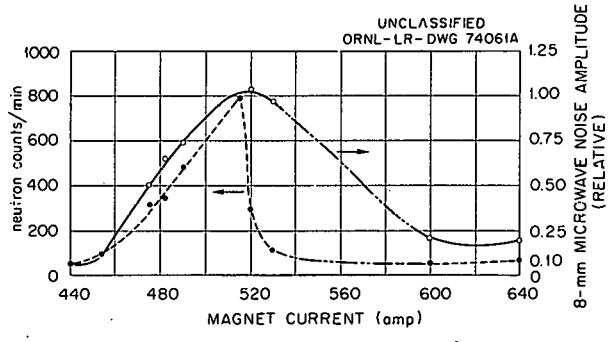

Fig. 3.4. Neutron Counting Rate and 8-mm Microwave Noise Amplitude as a Function of Magnet Current.

noise amplitude is correlated with the microwave resonant-heating-zone positions near the mirror throats.

Four methods were used to obtain a rough determination of the energy spectrum of the neutrons.

This spectroscopy was performed to find the fraction of neutrons from electromagnetic processes [e.g., (γ,n) and (e,ne) processes], which have kilovolt energies, as opposed to the neutrons from nuclear processes (e.g., D-D reactions), which have million-electron-volt energies. The first method was to attempt to produce P^{32} from the reaction $S^{32}(n,p)P^{32}$. This reaction has a neutron threshold at about 1 Mev. The measurement consists in exposing a large quantity of sulfur to the neutron flux from the PTF, extracting the P^{32} by chemical methods, and measuring the total activity produced.[5] Another determination of million-electron-volt neutron flux was made by counting recoil proton tracks in Eastman NTA emulsions. Neutrons of 2.45 Mev will produce recoil proton tracks up to 70 μ in length in this emulsion, with the shortest detectable track (3 grains or 7 μ) corresponding to a minimum neutron energy of 250 kev. Emulsion exposed to a known flux of neutrons from an Am-α-Be source and unexposed emulsion were processed along with those exposed to radiation from the plasma. The number of tracks in films irradiated by the plasma were then compared with the number in calibrated films. Unexposed films allowed subtraction of "background" tracks.

The third method was to attempt to observe the reaction $He^3(n,p)T$ in a 10-atm He^3 proportional counter. Because of wall effects in the counter, it was impossible to unambiguously detect this reaction with 2.45-Mev D-D neutrons; however, He^3 recoils from elastically scattered million-electron-volt neutrons were observed. Figure 3.5 shows a calibration pulse-height-analyzer spectrum

[5]We gratefully acknowledge the supporting effort of W. S. Lyon and co-workers of the Analytical Chemistry Division for the chemical processing and low-level activation measurements.

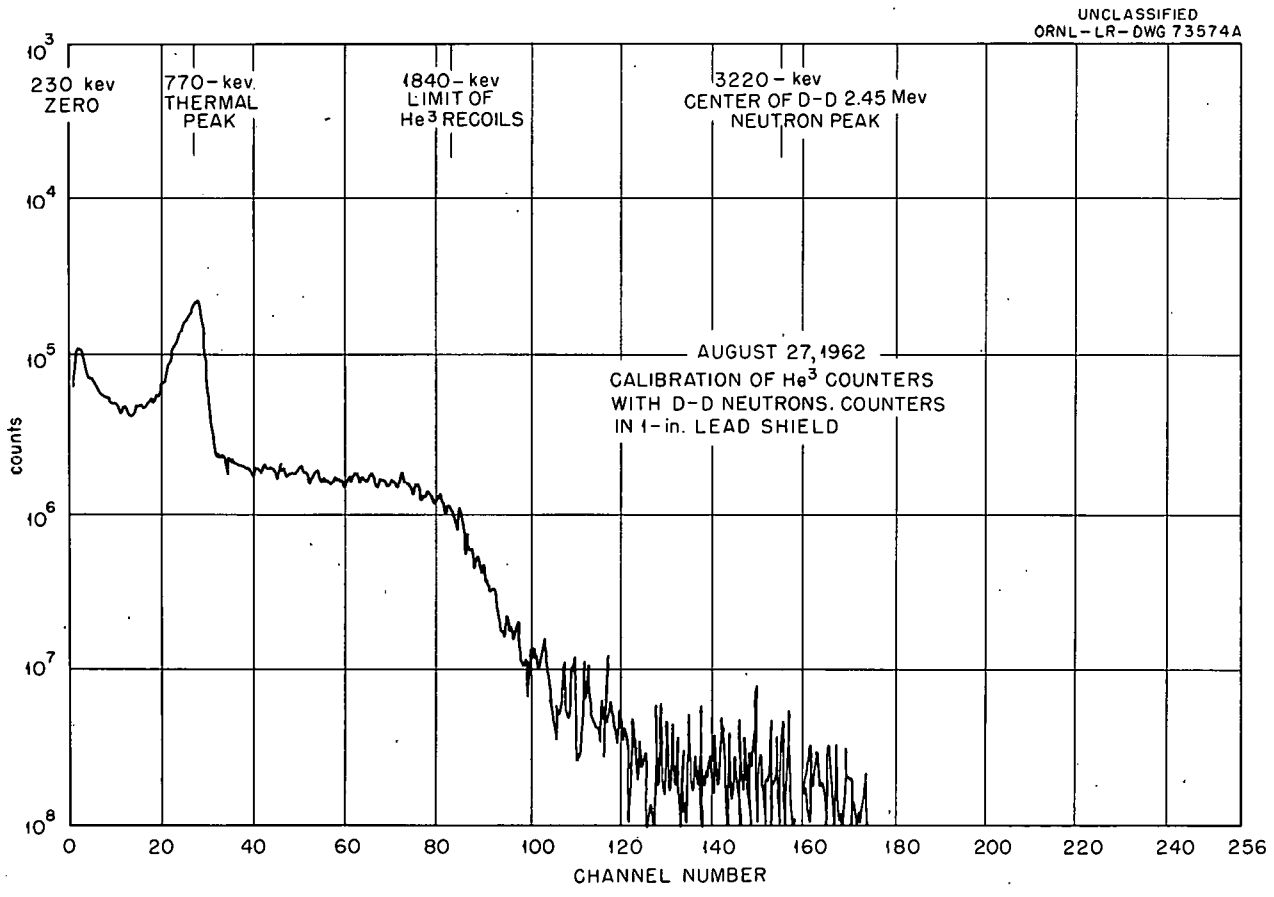

Fig. 3.5. Calibration Pulse-Height-Analyzer Spectrum of D-D Neutrons in He^3 Counter.

of the counter exposed to 2.45-Mev neutrons, and Fig. 3.6 shows the pulse-height-analyzer spectrum of neutrons from the PTF. The fourth method was to measure the complete spectrum of the neutrons emitted from the PTF by a "Bonner Sphere" spectrometer.[6] Briefly, this spectrometer moderates neutrons in several spheres of polyethylene and detects the thermalized neutrons in an Li^6I crystal scintillator with a multiplier phototube. Each sphere has a different moderating efficiency for a given neutron energy. A computer analysis of the counting rates due to the different spheres is required to determine the spectrum.[7]

The results of the four measurements were in essential agreement, although all suffered large statistical errors because of the low source strength of the neutrons and the poor geometrical solid angle available. All measurements showed that between 10 and 40% of the neutrons had energies greater than 1 Mev. Between 60 and and 90% of the neutrons had energies in the kilovolt range.

The most reasonable explanation of the large flux of kilovolt neutrons from the electron-cyclotron plasma (ECP) appears to be coulomb- or electrodissociation of deuterium by high-energy electrons (i.e., $e + D \rightarrow e + n + p$). Electrons with energies greater than the binding energy of deuterium have been postulated previously in the ECP, since x rays with several million electron volts of energy have been observed.[4] There is an insufficient amount of D_2 or beryllium in or near the PTF to produce the neutrons by (γ,n) processes, and all

[6]R. T. Bramblett, R. I. Ewing, and T. W. Bonner, *Nucl. Instr. Methods* 9, 1 (1960); *Neutron Phys. Div. Ann. Progr. Rept. Sept. 1, 1962*, ORNL-3360, sec 8.4.

[7]We gratefully acknowledge the loan of the Bonner spectrometer from the Neutron Physics Division and the aid of W. R. Burrus in analyzing and reducing the data.

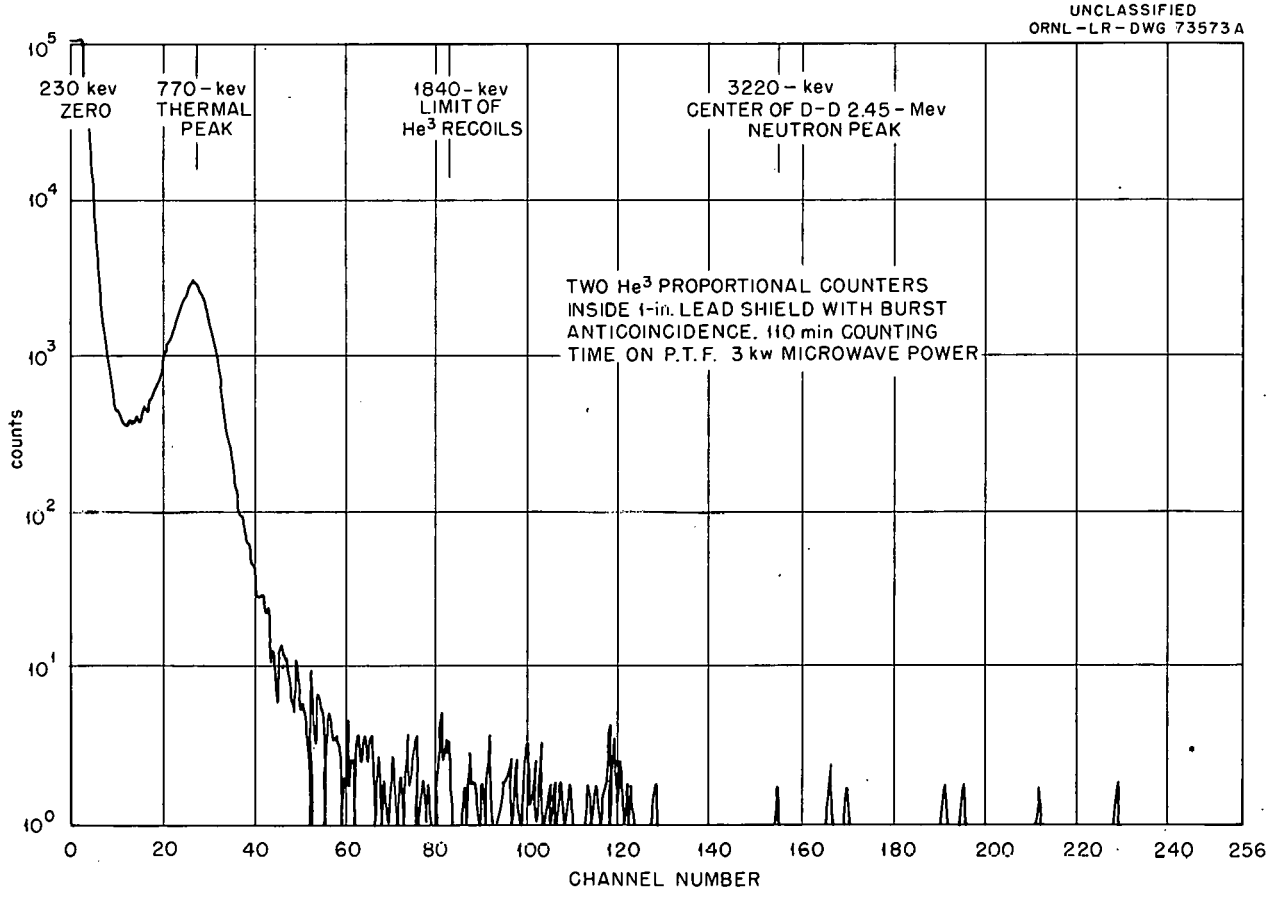

Fig. 3.6. Pulse-Height-Analyzer Spectrum of PTF Neutrons in He^3 Counter.

other materials have too high a (γ,n) threshold to produce the observed neutron flux.

Calculations by Soper,[8] based on the formulas of Guth and Mullin,[9] show that the cross section for electrodissociation at 3 Mev is $\sim 10^{-30}$ cm^2. A measurement by Paul[10] at an electron energy of 3.8 Mev estimates the cross section to be in the range 10^{-31} to 10^{-30} cm^2, which is in substantial agreement with the above calculation.

On the basis of this cross section and a plasma volume of 10^4 cm^3, it is estimated that a high-energy ($\gtrsim 3$ Mev) electron population of $\sim 10^9$/cm^3 is required for the observed neutron emission rate. As the plasma density is $\sim 10^{12}$/cm^3, this requires only a small fraction of the electrons to be in the energy group which produces the neutrons and is in substantial agreement with the observed x-ray flux measurements previously reported.[11]

3.2 AN OPTIMUM ENERGY FOR PLASMA CONFINEMENT

Igor Alexeff R. V. Neidigh

The study of plasma containment in a simple magnetic-mirror system is important to controlled-fusion work. In this section, we point out that the loss rates from ion-neutral multiple scattering and for charge exchange can be made quite low for deuterons in deuterium by choosing the ion energy properly. The combined ion loss rate by the above two processes produces a decay constant τ of about 20 msec for a residual gas pressure of 2×10^{-5} torr. This loss rate is sufficiently low that other interesting processes such as plasma instabilities and ion cooling by plasma electrons should be easily studied under conditions of relatively poor vacuum in modest apparatus.

Loss rates from a deuterium plasma and from a helium plasma are contrasted in Fig. 3.7. Consider the lower curves where the τ values (in seconds) for the loss of trapped helium ions by 90° multiple scattering on neutral helium atoms

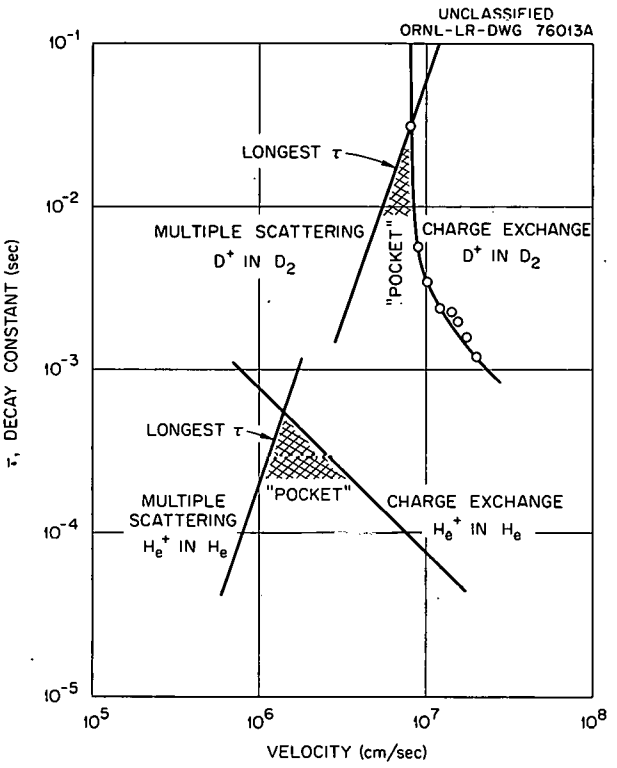

Fig. 3.7. Plasma Decay Constant τ for Charge Exchange and for Ion-Neutral Scattering-Loss Processes. The gas pressure assumed to compute each curve is 2×10^{-5} torr for D_2 and 5.5×10^{-5} torr for He. These values correspond to experimental pressures which are frequently used.

and for the loss by charge exchange are plotted separately. The scattering τ is calculated from classical particle-scattering laws.[12] The charge exchange τ is simply $1/\sigma_{cx} n v$, where for He^+ in He, the charge-exchange cross section σ_{cx} (cm^2) is almost independent of ion energy.[13] In this formula, n is the neutral atom density (cm^{-3}), and v is the ion velocity (cm/sec). At velocities below about 10^6 cm/sec, most of the ion loss will be due to scattering; above that velocity, most of the loss will be due to charge exchange. At the intersection of the two curves, there is an energy group of particles which has a maximum

[8] G. K. Soper, "Coulomb Dissociation of Deuteron by Electron," this report, sec 6.6.

[9] Eugene Guth and C. J. Mullin, *Phys. Rev.* **76**, 239 (1949).

[10] W. Paul, *Naturwissenschaften* 1, 31 (1949).

[11] *Thermonuclear Div. Semiann. Progr. Rept. Apr. 30, 1962*, ORNL-3315, sec 3.1.

[12] J. Orear, A. H. Rosenfeld, and R. A. Schluter, *Nuclear Physics*, p 34, University of Chicago Press, 1951.

[13] S. N. Ghosh and W. F. Sheridan, *J. Chem. Phys.* **26**, 480 (1957).

containment time. The corresponding He^+ energy is 7 ev, and the longest τ value that can be expected from this model is less than a millisecond.

The upper pair of curves pertains to deuterium, where the scattering now is that of D^+ on D_2 and yields a τ curve for loss by scattering that is qualitatively like that for helium. A major distinction between deuterium and helium arises in the τ curve for loss by charge exchange. For D^+ in D_2 in this energy range, the cross section decreases rapidly with decreasing energy. The published[14,15] charge-exchange data in the 0 to 400 ev energy range is given in Table 3.1. As σ_{cx} approaches zero, τ will approach infinity. The charge exchange curve in Fig. 3.7 is plotted from the data of Table 3.1. In the figure, the

Table 3.1. Charge Exchange Cross Sections for D^+ in D_2

Energy (ev)	α_I (cm^{-1})[a]	σ_{cx} (cm^2/atom)
0–50	0	0
65	0.1	0.0283×10^{-16}
80	0.5	0.141×10^{-16}
100	0.74	0.21×10^{-16}
150	0.86	0.243×10^{-16}
200	0.79	0.224×10^{-16}
250	0.81	0.229×10^{-16}
300	0.93	0.263×10^{-16}
400	1.05	0.297×10^{-16}

[a]The conversion from $\alpha_I(cm^{-1})$ to $\sigma_{cx}(cm^2/atom)$ may be obtained from the relation $3.536 \times 10^{16}\, \sigma_{cx} = \alpha_I$ (see ref 15).

σ_{cx} values were adjusted to cm^2/molecule. At the intersection of the charge exchange and scattering curves is a region of ion energy (about 70 ev) having a decay constant τ of about 20 msec. This longer containment time should allow mechanisms of plasma loss other than ion-atom scattering and charge exchange to be studied at the relatively high pressure of 2×10^{-5} torr.

Note that one need not fill the apparatus with deuterium ions of exactly 70 ev. If the ions are injected with a considerable energy spread, those faster and those slower than 70 ev will be rapidly eliminated during the subsequent plasma decay. Thus a decaying deuterium plasma should tend to become monoenergetic, and exhibit quite well-defined values for the decay constant, etc.

Preliminary experiments with a small magnetic mirror apparatus at ORNL seem to support the above picture. The τ of a decaying deuterium plasma has been measured both by collecting ions on an end collector and by microwaves. The data yields a τ of about 20 msec at a gas pressure of 2×10^{-5} torr. The initial plasma density is not yet known unambiguously, but lies in the range of 10^9 to 10^{11} ions/cm^3. Preliminary experimental results for helium indicate a much shorter τ value than for deuterium in agreement with theory.

Thus there are some experimental data supporting the theoretical conclusion that operating a deuterium plasma in a mirror machine at about 70 ev ion energy leads to the longer plasma lifetime. The advantage of being able to operate a plasma research device at the relatively high pressure of 2×10^{-5} torr is obvious.

The authors wish to thank C. F. Barnett for checking this manuscript and for calling our attention to the charge exchange cross-section data of Cramer and Marcus.

3.3 DECAY OF A PLASMA DOMINATED BY ION COOLING

Igor Alexeff R. V. Neidigh

In Sec 3.2 the only plasma ion losses considered are charge-exchange and ion-neutral multiple scattering. However, cooling of the ions by interactions with cold plasma electrons should greatly increase the ion loss rate.[16] The loss rate is increased because the cooler ions suffer from more multiple scattering. In this section, the effect of ion cooling on the decay of a plasma is computed quantitatively.

[14]W. H. Cramer and A. B. Marcus, *J. Chem. Phys.* **32**, 186 (1960).

[15]W. H. Cramer and J. H. Simons, *J. Chem. Phys.* **26**, 1272 (1957).

[16]Lyman Spitzer, Jr., and T. Stix, private communication.

In the case of interest – deuterons in deuterium gas – the charge-exchange ion loss need not be considered. Charge-exchange losses appear to become negligible[17] below 70 ev, and the effect of ion cooling is to move ions rapidly away from the charge-exchange energy region. Thus the only losses considered here are ion particle losses due to ion-neutral multiple scattering, and ion energy losses due to ion cooling by electrons.

The equation of ion-neutral multiple scattering is easily derived from the multiple-scattering formula in Fermi's nuclear physics notes.[18] The time τ_S required for multiple scattering of deuteron ions to reduce the plasma density by a factor of e^{-1} in a mirror machine is approximately given by the formula:

$$\tau_S = \frac{\pi m^2 v^3}{32\, N e^4 \ln (mv^2/2)\,(a/e^2)},$$

where

τ_S = plasma decay constant, sec,

m = deuteron mass, g,

v = ion velocity, cm/sec,

N = density of deuteron *atoms* present as neutrals in the system, cm^{-3},

e = electron charge, esu,

a = radius of a deuteron molecule, cm.

The formula shows that the time constant τ_S varies during the plasma decay, because the ion energy is decreasing and the ion velocity v is becoming smaller. To simplify the mathematical discussion, the slow variation of the logarithmic term is ignored.

In the equation for ion cooling by plasma electrons, two assumptions are made. First, the temperature of the plasma electrons is assumed to be a constant during the plasma decay. This assumption could correspond to the electrons being at room temperature, or to the electrons being heated but remaining below an easily excited energy level in the neutral gas. A second assumption is that the initial ion temperature is near 70 ev. Under the above assumptions, the ion-cooling formula takes a more simple, but approximate form:[19]

$$\tau_c = 5.87 \frac{AA_1}{n \ln \lambda}\left(\frac{T}{A}\right)^{3/2},$$

where

τ_c = cooling time (sec) for the average ion energy to drop a factor of e^{-1},

A = electron mass in proton mass units,

A_1 = deuteron mass in proton mass units,

T = electron temperature in °K,

n = electron density (cm^{-3}).

The ion density is also n, as charge neutrality in the plasma is assumed, and $\ln \lambda$ is a slowly varying function of electron energy and density which can adequately be approximated by the number 20. In the above form, the equation shows that the time constant τ_c varies during the plasma decay because the ion density n is decreasing.

The two above equations can be used to obtain the following equation, which describes the decay of the ion density trapped between magnetic mirrors:

$$\frac{n}{n_0\left(1+\frac{2}{3}\frac{\tau_e}{\tau_S}\right)-n} = \frac{3}{2}\frac{\tau_S}{\tau_c}\, e^{-[(3/2)(1/\tau_c)+(1/\tau_S)]t}.$$

In this equation n is the ion density at time t, n_0 is the ion density at $t = 0$, and τ_c and τ_S are the cooling and scattering time constants, respectively, evaluated at $t = 0$.

The above equation agrees quite well with the intuitive idea of how the plasma should decay. A graph of the decay curve is shown in Fig. 3.8. Initially, the ions have not had time to cool and are lost at the slow multiple-scattering rate given by τ_S. Thus, near $t = 0$, the graph has a small slope. Later, as the ions cool appreciably, the multiple-scattering losses greatly increase. Thus, at intermediate values of t, the slope of the graph increases. Finally, when many ions and electrons are lost, the ion-cooling process ceases to be effective. Thus, for t large, the multiple-scattering time constant becomes independent of t, and the graph shows an exponential decay.

---

[17] See preceding section.

[18] J. Orear, A. H. Rosenfeld, and R. A. Schluter, *Nuclear Physics*, p 34, University of Chicago Press, 1950.

[19] Lyman Spitzer, Jr., *Physics of Fully Ionized Gases*, p 80, Interscience, New York, 1956.

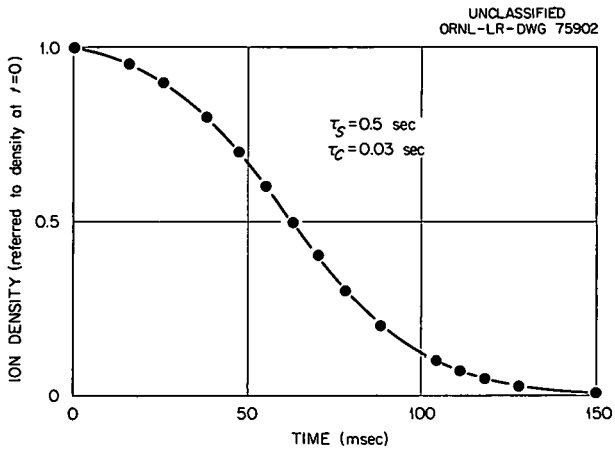

Fig. 3.8. Ion Density as a Function of Time.

An experimental study of the plasma decay does not show the initial slow decay and subsequent drop in the decay curve in any clear-cut manner. However, this lack of experimental agreement with theory is not surprising, since the theory assumes that the ions at $t = 0$ are monoenergetic, which is almost surely false. The initial ion energy distribution is probably quite broad, as the ion-cooling mechanism is probably always at work in the steady-state operation preceding a decay in the apparatus.

The important conclusions of this discussion are as follows: First, in a plasma dominated by ion cooling by cold electrons the decay curve finally does become an exponential. Second, if $\tau_c \ll \tau_s$, the final decay constant is $\frac{2}{3}\tau_c$, where τ_c is the cooling-time constant evaluated at $t = 0$. Third, measuring the final decay constant $\frac{2}{3}\tau_c$ allows one to get a better idea of the initial plasma electron density n and the electron temperature T, because these quantities are the only variables present in τ_c.

3.4 CONFINEMENT OF A DEUTERIUM PLASMA BETWEEN MAGNETIC MIRRORS

Igor Alexeff R. V. Neidigh

Experiments with the small magnetic-mirror apparatus at the Arc Research Facility seem to support the decay constant vs energy picture of the preceding section. The τ of a decaying deuterium plasma has been measured both by collecting ions on an end collector and by microwaves. The data yield a τ of about 15 msec at a gas pressure of 2×10^{-5} torr, which agrees well with the theoretical value of 20 msec. The initial density is not yet known unambiguously, but lies in the range of 10^9 to 10^{11} ions/cm^3. Preliminary experimental results for helium indicate a much shorter τ value than for deuterium, in agreement with theory.

The apparatus is shown in Fig. 3.9. Removable coils shape the magnetic field to form two mirrors within the more extensive uniform magnetic field of 30 × 30 in. iron pole pieces. The field strengths are 5000, 1400, and 5000 gauss on the coil axis. The pressure gradient arc[20] (mode II) with its associated secondary plasma is formed between the mirrors by feeding deuterium gas into the anode – the restricted opening in one mirror coil. Electrons are accelerated from the filament, which is biased several kilovolts negative as indicated. The filament is covered with a shield at its bias potential except for a portion which "sees" through the anode. Magnetic-field lines which terminate on the filament do not intersect the anode but pass through the restricted mirror opening. The anticathode, which is electrically insulated, reflects the primary electron stream. For measurements of the decay of the plasma a pneumatically operated shutter closes the restricted opening in the coil throat in 2 msec. The shutter removes the primary electron stream and the neutral gas input from the plasma region between the coils. It also shields the plasma from the negatively biased hot filament. The pneumatically driven shaft which closes the shutter subsequently removes the bias from the hot filament.

Measurements of lifetime and density of the plasma have been made by the method of the "plasma sweeper."[21] Briefly, the shutter is closed, which removes the source of plasma in about 2 msec. Plasma within the escape cone of the mirrors rapidly moves out, and is not studied

[20] R. V. Neidigh, *The ORNL Thermonuclear Program*, ORNL-2457, pp 55–59, 164–65 (1958); R. V. Neidigh, *The Effect of a Pressure Gradient on a Magnetically Collimated Arc*, ORNL-2288 (1957).

[21] Igor Alexeff and R. V. Neidigh, "A Way to Measure Plasma Density – The 'Plasma Sweeper,'" to be published in the *Proceedings of the Third Annual Symposium on the Engineering Aspects of Magnetohydrodynamics, University of Rochester, Rochester, New York, March 28–30, 1962.*

UNCLASSIFIED
ORNL-LR-DWG 74424A

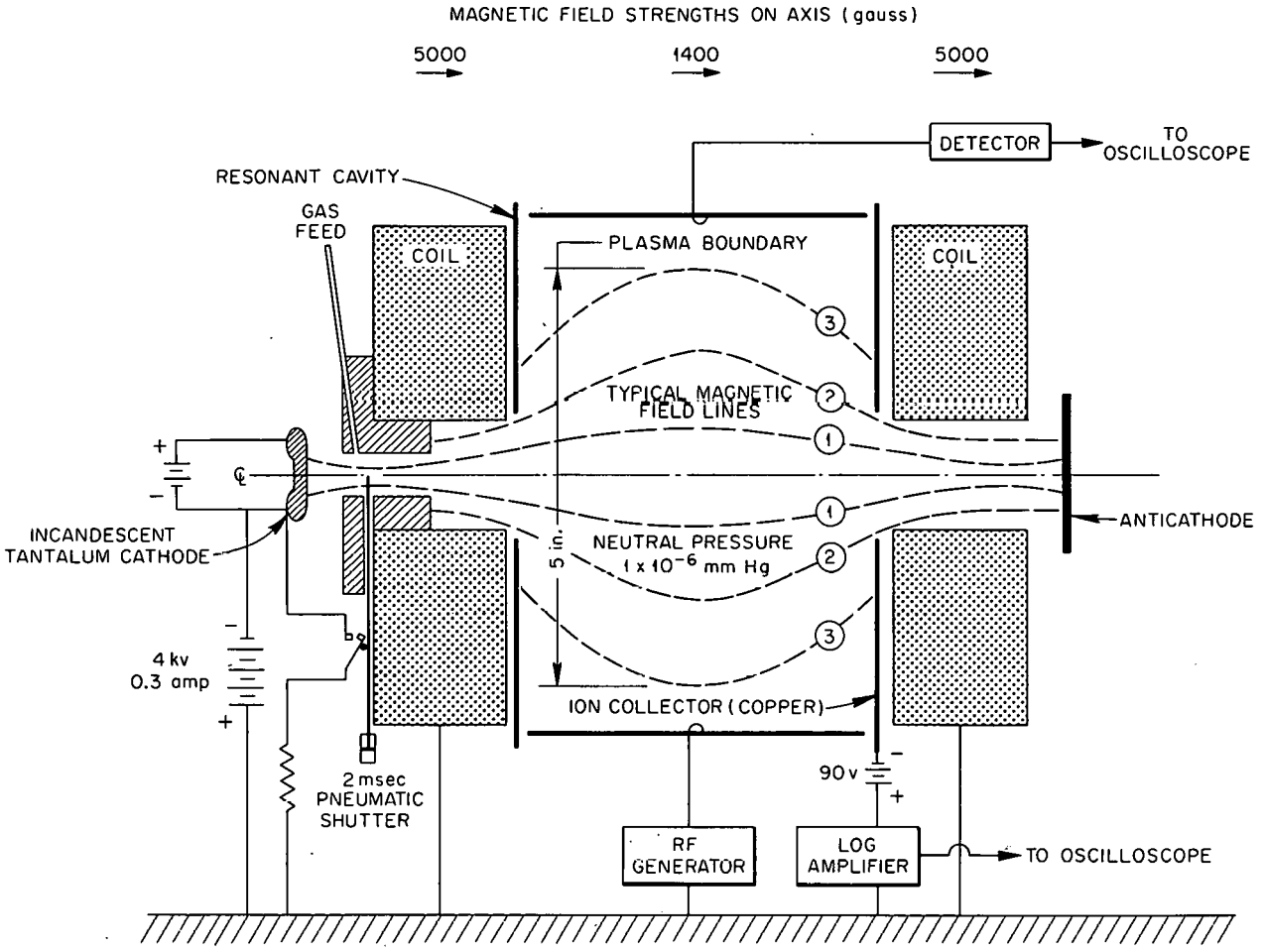

Fig. 3.9. Schematic Diagram of the Small Magnetic-Mirror Apparatus.

here. Ions, of primary origin, formed by oscillating electrons in the potential well of the plasma, or formed by charge exchange, drift longitudinally, and half of those occupying the zone between lines 2 and 3 are collected on the biased (−45 v) annular collector shown in the figure. Intermittent application of the sweeper bias makes the ion current correspondingly intermittent but does not alter the τ or the area under the curve. Other tests of the sweeper[22] have shown that the presence of this biased collector does not appreciably affect the behavior of the plasma, and that its electric field is apparently shielded from the plasma by a sheath; it collects only the ions that drift to the sheath. The ion current is fed into a logarithmic amplifier and the output is time analyzed on one-half of a dual-beam oscilloscope.

Simultaneously with this measurement another measurement of the plasma decay is made. The plasma region is within a microwave cavity, as shown in the figure. The resonant frequency of the cavity in the TM 010 mode is 763 Mc. A modulated microwave signal at about this frequency is fed into the cavity from the generator as shown in the figure. The signal is similarly removed from the cavity, detected, and the amplitude of the modulation is time analyzed on the other beam of the dual-beam oscilloscope. When the plasma is present, the cavity is detuned so that no signal

[22] Igor Alexeff, R. V. Neidigh, and E. D. Shipley, *J. Nucl. Energy: Pt C:* 4, 263–66 (1962).

appears in the output. As the plasma dissipates, the amplitude of the output signal increases until the full amplitude is reached.

The type of data obtainable is shown in Fig. 3.10. Note that for two different plasma adjustments both the plasma sweeper and the microwave measurement of τ agree. The observed τ is in the range of tens of milliseconds in agreement with theory. The longest τ observed for a deuterium plasma has been 40 msec.

It has been shown[23] that there should be a cooling of the ions in the plasma by the electrons. This is not a direct loss mechanism, but it should tend to decrease the value of the τ expected from the theory as depicted in Fig. 3.10, since ions colder than about 70 ev will be scattered and lost rapidly. Indeed, in some cases the cooling τ may set the upper limit for the decay τ once the losses come to equilibrium. In the upper photograph of Fig. 3.10 the applied filament bias is 2 kv, while in the lower photograph it is 1.5 kv. The implication is that the electron temperature to which the ions are cooled is greater in the plasma of the upper photograph than it is in the plasma of the lower photograph,

[23] Lyman Spitzer, Jr., *Physics of Fully Ionized Gases*, pp 76–80, Interscience, New York, 1956.

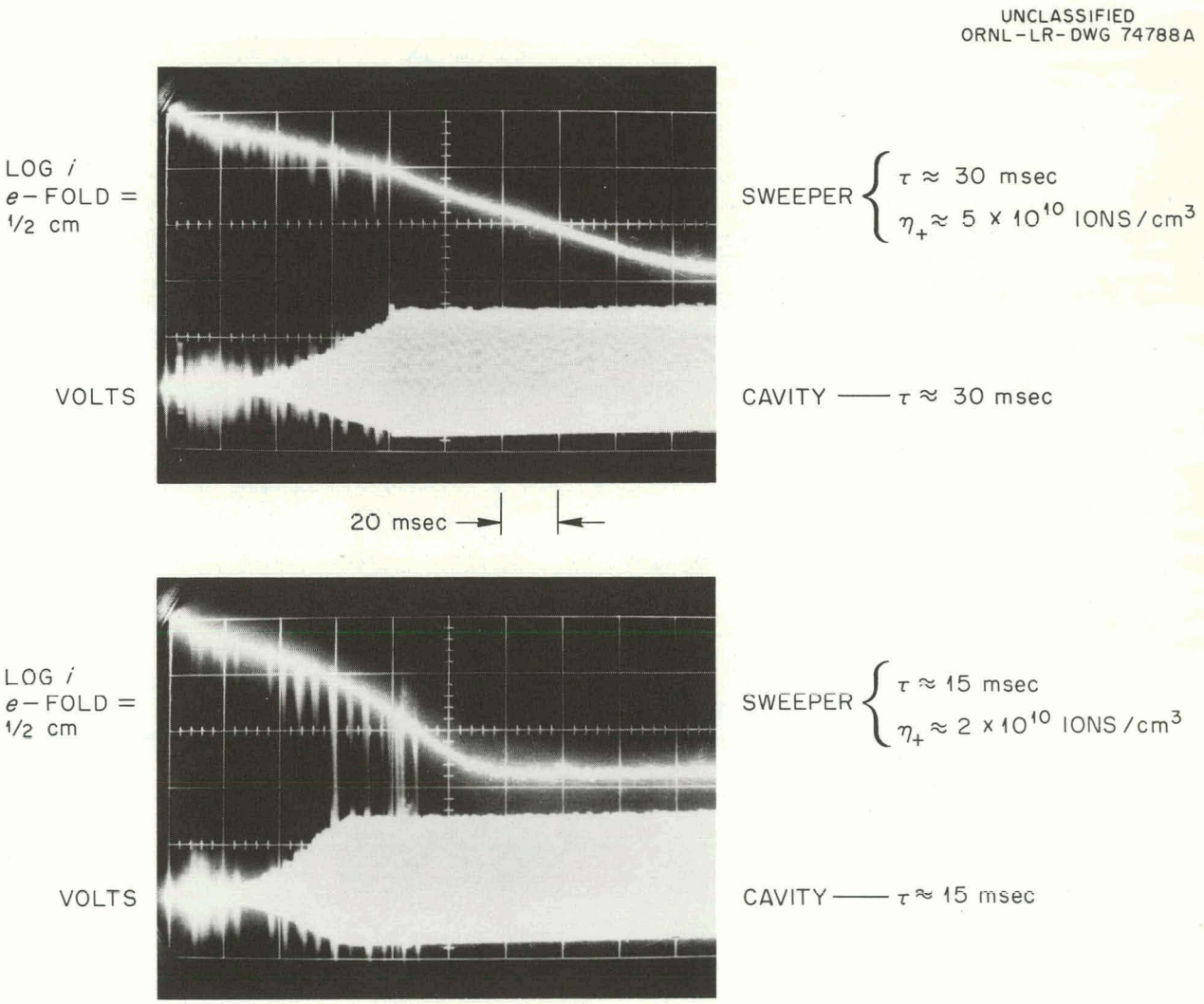

Fig. 3.10. Plasma Sweeper and Microwave Transmission Data from the Decaying Plasma. The upper photograph with the longer decay constant was from a plasma which had been adjusted for greater filament bias voltage.

because the τ is longer. For example, a 15- and 30-msec τ corresponds to a cold electron sink of about 10 and 16 ev electrons respectively.

3.5 MEASUREMENT OF PLASMA DECAY TIME AND DENSITY WITH A CAVITY RESONATOR

Igor Alexeff R. V. Neidigh

In measuring the plasma properties discussed in Sec 3.4, microwave cavity measurements were used. The advantage of microwave cavity techniques over the collection of escaping charge – the plasma sweeper[24] – is that microwaves should measure the plasma density present *in the apparatus*, while the plasma sweeper merely measures the rate at which plasma *escapes from the apparatus*. Thus the density measurements obtained by use of microwaves are more direct. Also, using a second technique to measure plasma density is a check on the first technique.

The choice of using a resonant cavity over a microwave interferometer was made after careful discussions with W. B. Ard, R. A. Dandl, and H. O. Eason. Briefly, the cavity method was chosen because it seems to be more sensitive for plasma densities of about 10^8 ions/cm^3, and the apparatus is much easier to construct.

A diagram of the experimental apparatus is shown in Fig. 3.11. The cavity is a copper cylinder 6 in. in radius and 6 in. deep. Plasma is injected into the cavity from a mode II source.[25] Gas produced inside the cavity is pumped out through $\frac{3}{4}$-in. holes. The cavity is actually made in three pieces, the end plates being electrically insulated from the central portion. With the end plates insulated, they can be used to measure the escaping plasma flux by means of the plasma-sweeper technique.

Although the ends of the cavity are insulated from the central section for direct current, at microwave frequencies the cavity behaves as if it were a closed box. The microwave radio energy can flow freely from one end of the cavity to the other because large flanges at the ends, insulated by sheet Teflon, act as bypass capacitors. These capacitors work quite well, and the Q of the cavity at 763 Mc is experimentally found to be approximately 1000.

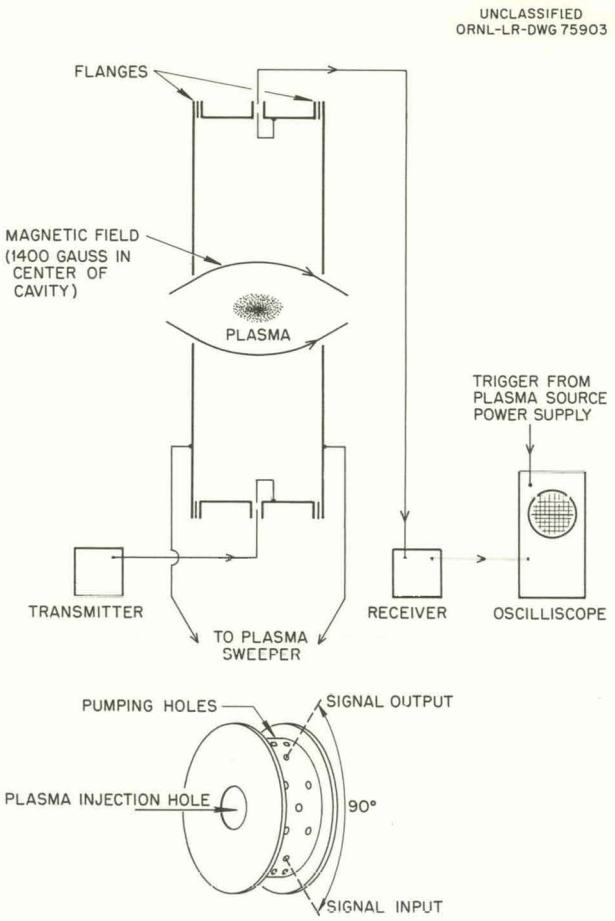

Fig. 3.11. Resonant Cavity and Associated Apparatus.

The cavity is excited by a magnetic loop, and the output signal is picked up by a second loop oriented at right angles to the first loop. The cavity is excited in the TM 010 mode. In this mode, the electric field is parallel to the axis of the cavity, is a maximum on the axis, and goes to zero at the outer wall without passing through any zeros. The resonant frequency of this mode is 763 Mc when no plasma is present.

If plasma is placed in the cavity, the resonant frequency is shifted, and the shift in frequency provides a measure of plasma density. The plasma density is given by the following formula:[26]

---

[24]Igor Alexeff and R. V. Neidigh, *Thermonuclear Div. Semiann. Progr. Rept. Apr. 30, 1962,* ORNL-3315, pp 38, 41.

[25]*Ibid.*, p 41.

[26]S. C. Brown and D. J. Rose, *Massachusetts Institute of Technology Technical Report 230* (May 6, 1952).

$$n = 0.269\left[\left(2\pi\frac{m_e}{e^2}\right)(\nu\Delta\nu)\left(\frac{v}{\Delta v}\right)\right] .$$

In this formula, n is the electron density (cm^{-3}), 0.269 is a constant arising from a Bessel function, m_e is the electron mass (g), e is the electron charge (esu), ν is the resonant frequency of the cavity when no plasma is present (sec^{-1}), $\Delta\nu$ is the shift in the resonant frequency caused by the plasma (sec^{-1}), v is the volume inside the cavity (cm^3), and Δv is the volume occupied by the plasma (cm^3). For this formula to be valid, one must have $\Delta\nu \ll \nu$ and $\Delta v \ll v$. Also, the plasma must be located near the axis of the cavity.

The above formula for frequency shift is not valid if a magnetic field impedes the electron motion induced by the radio transmitter. Therefore, in this work the oscillation mode of the cavity resonator was chosen so that the rf electric field is roughly parallel to the magnetic field. If the two fields were completely parallel and if the magnetic field were uniform, then the magnetic field would not affect the above formula for frequency shift.[27] However, in this experiment the two fields are only *approximately* parallel, and the magnetic field is *not* uniform. Therefore, deviations from the formula for frequency shift might be expected.

Even if the frequency-shift formula is *not* valid, one can still obtain the plasma decay time constant. This is possible because one expects small shifts in the cavity resonant frequency to depend *linearly* on plasma density. Thus, measurements of the frequency shift at various times during a plasma decay yield relative plasma densities, and a decay curve may be plotted in relative units.

The technique of measuring a plasma decay curve is as follows: First, the response curve of the empty cavity as a function of transmitter frequency is experimentally measured as shown in Fig. 3.12. Thus, if the transmitter frequency is shifted by 1 Mc from 763 Mc, the receiver output voltage drops by a factor of 7.

Next, one notes that adding plasma to the cavity shifts the cavity response curve to a higher frequency. This curve displacement is shown graphically in Fig. 3.13. Note that shifting the response curve up in frequency by $+\Delta\nu$ causes the radio

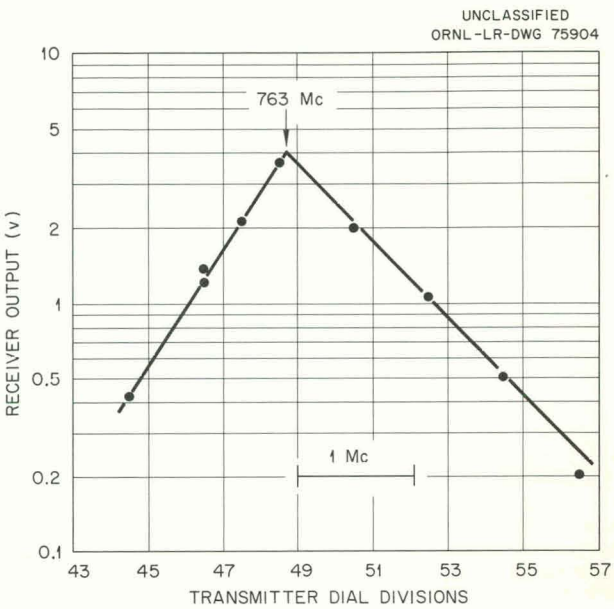

Fig. 3.12. Experimentally Measured Cavity Response Curve. The sides of the curve are approximated by straight lines for computing purposes.

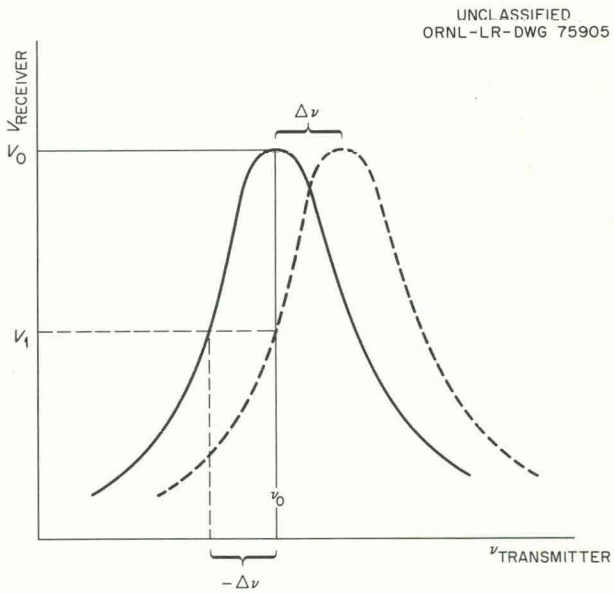

Fig. 3.13. Effect of Plasma on Receiver Output Voltage. The figure illustrates that shifting the cavity resonant frequency upward by $+\Delta\nu$ has the same effect on receiver output voltage as lowering the transmitter frequency by $-\Delta\nu$.

[27] Lyman Spitzer, Jr., *Physics of Fully Ionized Gases*, sec 4, Interscience, New York, 1956.

receiver output to change by the same amount as occurs by dropping the transmitter frequency by $-\Delta\nu$.

To measure plasma properties during a plasma decay, one merely measures the output voltage of the radio receiver as a function of time. For each value of the output voltage, one projects back along the cavity response curve and obtains a frequency shift, $\Delta\nu$. Plotting $\Delta\nu$ as a function of time on a semilogarithmic graph yields a time constant for plasma decay. This is true because $\Delta\nu$ is assumed proportional to the plasma density n.

The values of cavity resonant frequency shift vs time can be used to compute plasma density by means of the previously discussed formula. The resulting values of plasma density vs time can be extrapolated back to $t = 0$ and thus can yield the steady-state plasma density.

Experimental measurements of plasma properties are shown in the oscillograms of Fig. 3.14. The oscillograms represent envelopes of a 1000-cycle modulation signal on the radio transmitter signal. The modulated signal is easier to study than a dc signal. The noise spikes on the envelopes

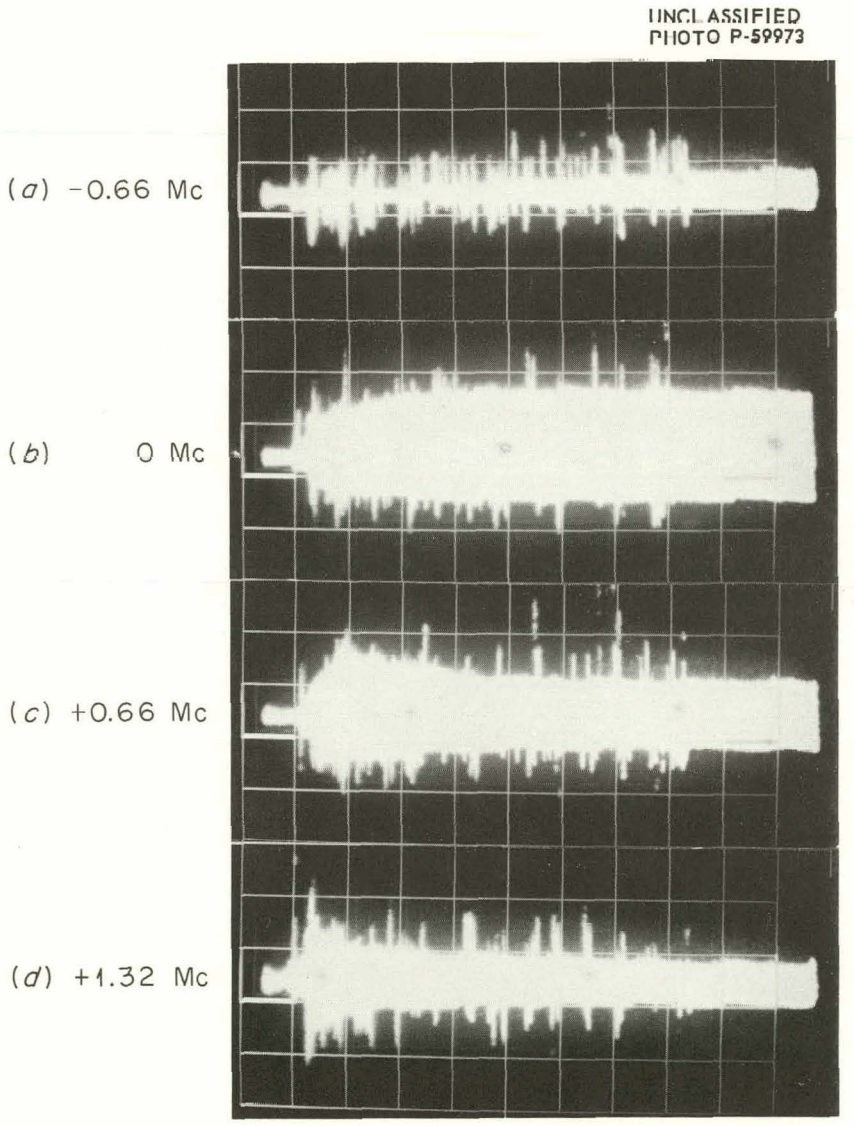

Fig. 3.14. Receiver Output Voltage vs Time: Horizontal Scale 10 msec/division, Vertical Scale 2 v/division. Frequency shift of transmitter relative to resonant frequency of empty cavity.

are due to noise generated in the apparatus by an extraneous high-voltage discharge.

The decay envelopes support the previously discussed technique of measuring plasma decay. For a transmitter frequency below the resonant frequency ν_0 of an empty cavity, the receiver voltage rises with plasma decay. However, the voltage never reaches the high value obtained at resonance. At ν_0 the voltage rises smoothly to a high value. Above ν_0 the voltage peaks, then decays. Further above ν_0, the voltage peaks earlier, corresponding to a higher plasma density required for resonance.

Another important observation obtained from the curves of Fig. 3.14 is that the plasma does not absorb much radio energy. The resonance peaks for the envelopes *b*, *c*, and *d* are all of the same height, although each peak corresponds to a different plasma density in the cavity.

A curve showing the plasma decay is given in Fig. 3.15. This curve is obtained from the envelope of Fig. 3.14*c*. This curve yields a time constant of 12 msec, in excellent agreement with the value of 15 msec obtained with a plasma sweeper. The two decay measurements were made simultaneously. Unfortunately, the measurements of ion density made by the two methods disagree by a factor of 37. At $t = 0$, $n_{rf} = 1.8 \times 10^8$ ions/cm^3, and $n_{sweeper} = 6.6 \times 10^9$ ions/cm^3.

Further experiments show that the two observations above are true in general. The time constant of a decaying plasma is the same when measured by the resonant cavity and by the plasma sweeper, but the ion density measured by the resonant cavity is much lower than the density obtained by the plasma sweeper.

The reason for the discrepancy in the ion-density measurements is not known. However, as previously discussed, the cavity measurements may yield a low value because a mirror magnetic field is present. If the magnetic field impeded the oscillatory motion of the electrons, they would cause a smaller frequency shift than expected, and the density measurements would be low. On the other hand, the plasma-sweeper values may be high. For example, the amount of charge collected might be high because an electrical discharge was induced by the electric field of the plasma sweeper. Attempts to resolve the discrepancy will be made in future work.

However, the agreement between the values of plasma decay time obtained by the two methods is encouraging. As previously discussed, the cavity value of the decay constant may be correct even if the cavity value of the ion density is incorrect. Thus the plasma decay constants found in earlier experiments with the plasma sweeper alone are probably valid.

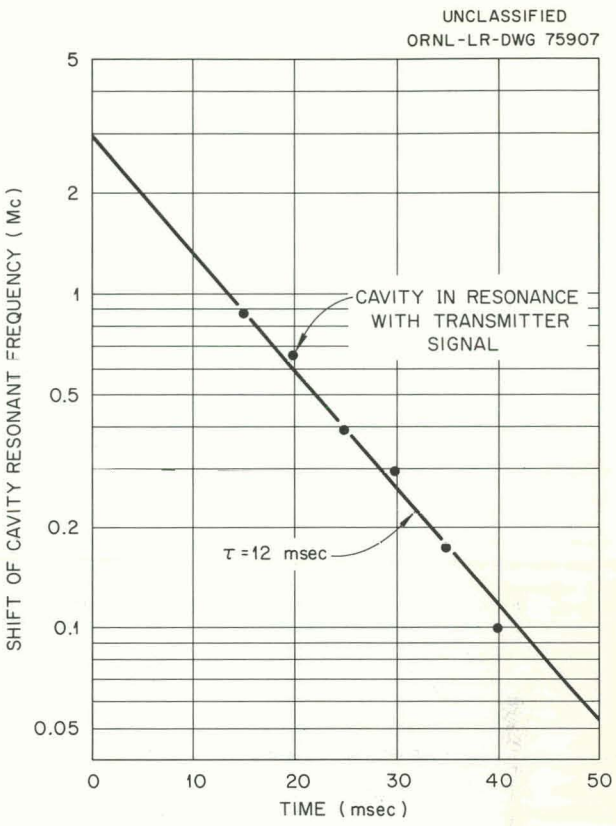

Fig. 3.15. Plasma Decay Curve. Data obtained from oscillogram of Fig. 3.15*c*.

3.6 A STROBOSCOPIC SHUTTER FOR VISUALLY STUDYING PLASMA OSCILLATIONS

Igor Alexeff R. V. Neidigh

A military surplus Snooperscope (ref 28) has been converted into a stroboscopic shutter for the study of plasma oscillations. Some modification of the surplus item plus the adaptation of commercially available electronic gear has given

[28]The Snooperscope is obtained from Edmund Scientific Co., Barrington, N.J. The catalog number is 80,098.

a device with which periodic fluctuations in the light output of a plasma in the frequency range 10^3 to 10^6 cps can be stroboscopically "stopped" and studied. The electronic circuits permit a "lock on" to a reference signal obtained from the plasma. In this fashion, the stroboscopic shutter will operate even though the oscillations in the plasma have a frequency jitter of as much as 10%.

The following are characteristics of the converted Snooperscope. It utilizes the visible light from the plasma efficiently by an extremely efficient Schmidt light-gathering system. The electronics permit a 10% or higher duty cycle; that is, it accepts light for 10% or better of the observing time. Because the image is conveyed by electrons, it can be gated rapidly *on* and *off* by low voltages applied to the electrostatic lenses of the image converter tube. In particular, the gating voltage is applied to the cathode end of the image converter tube. A gating voltage of 250 v is sufficient, even though the image converter tube is operating at 2000 v. Finally, the unconverted Snooperscope is at present an inexpensive military surplus item.

A photograph of the modified Snooperscope is shown in Fig. 3.16. It is compact and portable.

UNCLASSIFIED
PHOTO P-59974

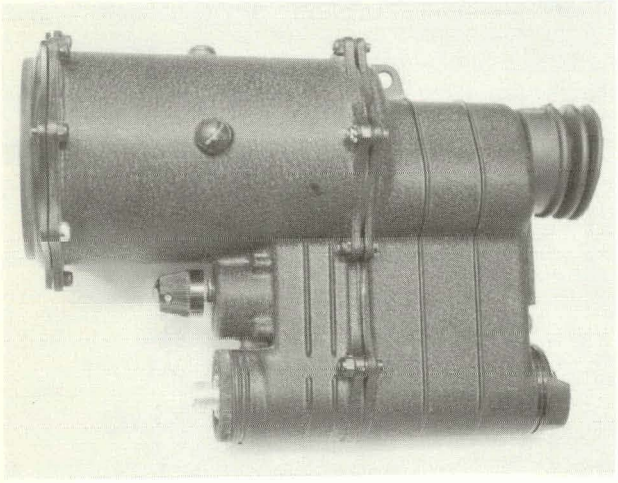

Fig. 3.16. Photograph of Snooperscope. The objective is at left, the eyepiece at right.

One cable is required to attach it to the associated electronics. The principle of operation is shown in Fig. 3.17. Light from the plasma under observation is collected by an efficient Schmidt optical

UNCLASSIFIED
ORNL-LR-DWG 75909

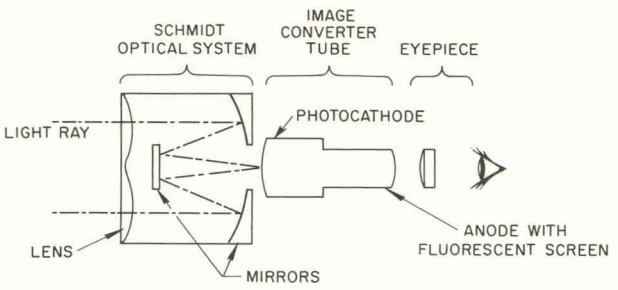

Fig. 3.17. Schematic Diagram of Snooperscope.

system and focused on the cathode of an image converter tube. Electrons emitted from a given illuminated spot on the photocathode are focused by electrostatic lenses, accelerated, and produce a corresponding spot of light at the anode by bombarding a fluorescent screen. Thus the image under observation is converted from a light picture to an electron picture and back to a light picture.

A block diagram of the apparatus is shown in Fig. 3.18. A reference signal is obtained from the oscillating plasma. The reference signal may be electrical (obtained from a probe) or optical (obtained from a photomultiplier tube). This reference signal is displayed on an oscilloscope which is internally triggered or externally locked to it. The oscilloscope supplies a positive gate pulse which is used to actuate the electronics. The gate pulse is attenuated to about a volt; then its phase is inverted by a simple, commercially available amplifier.[29] Next, the pulse is used to trigger a General Radio unit pulser,[30] which serves to provide a delayed pulse by means of its "delayed pulse" output. The purpose of this pulser is to provide a variable time delay between the time of triggering of the oscilloscope and the gating *on* of the modified Snooperscope. A delayed gate from an oscilloscope with this type of circuitry would serve the same purpose. From the first General Radio unit pulser,[30] the

[29]The amplifier is obtained from Kane Engineering Laboratories, 845 Commercial Street, Palo Alto, Calif. The catalog number is C-5A.

[30]The General Radio unit pulser is obtained from the General Radio Co., West Concord, Mass. The catalog number is 1217-B. This device requires an additional General Radio power supply, number 1201-B.

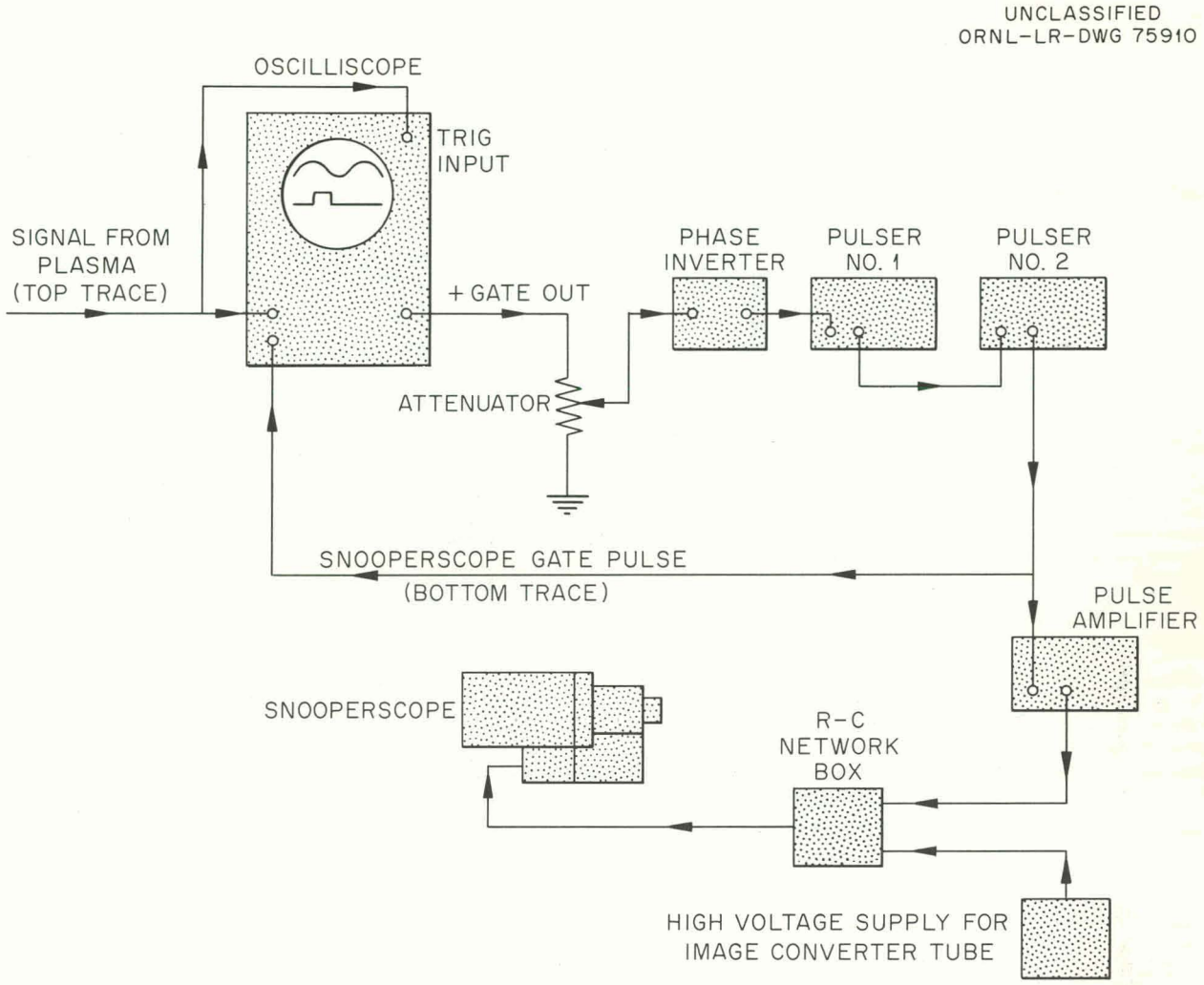

Fig. 3.18. Block Diagram of Electronics Used with Snooperscope.

delayed pulse goes to a second General Radio unit pulser.[30] This second pulser then provides the actual gate pulse, variable in length, which activates the image converter for an adjustable period of time. The second pulser does not provide enough voltage to activate the image converter directly; so the pulse is first amplified by a General Radio unit pulse amplifier.[31] The output of this amplifier now provides a negative pulse of 250 v, adjustable in duration and delay, for the control of the image converter tube.

A reference signal is also taken from the second General Radio unit pulser and is displayed on the triggered oscilloscope. This reference pulse indicates the period in which the Snooperscope is active relative to the reference signal obtained from the oscillating plasma.

The details of using the final pulse to operate the image converter are shown in Fig. 3.19. The negative pulse is fed to the tube by the same cable which conducts the high voltage. The negative pulse is isolated by a simple RC network, and the proper dc level is restored by a dc restorer of four germanium diodes. The dc pulses are placed on the photocathode, where they

[31]The General Radio unit pulse amplifier is obtained from the General Radio Co., West Concord, Mass. The catalog number is 1219-A. The power supply is self-contained.

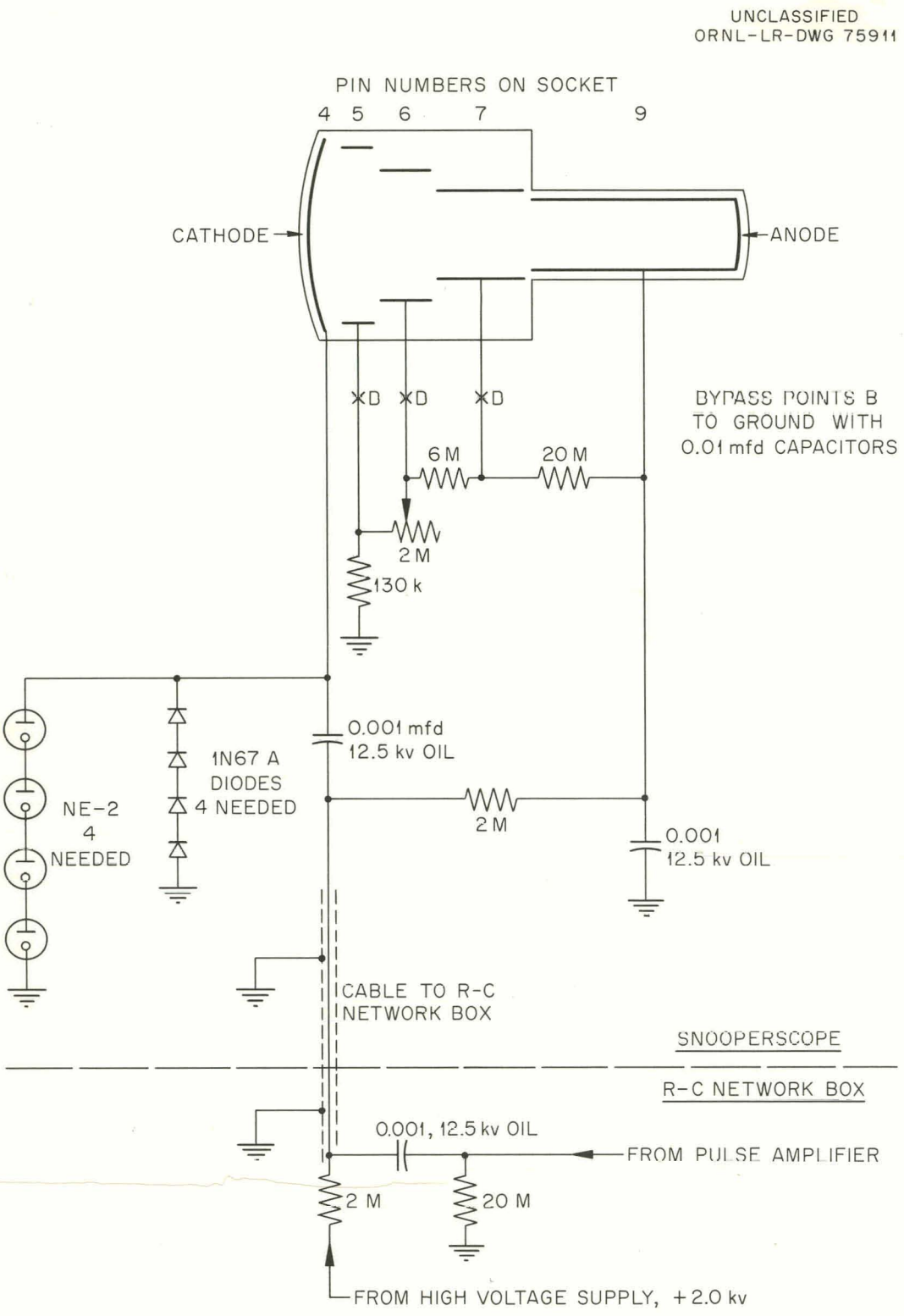

Fig. 3.19. Wiring Diagram of Snooperscope and of Associated RC Network Box.

drive it to ground. When the dc pulses are *not* present, the photocathode is at +250 v relative to the electrostatic lenses adjacent to it, and the tube does not conduct – no image is transmitted.

The following modifications were easily made on the surplus Snooperscope. The RC pulse separation network and the dc restorer replaced the built-in vibrator high-voltage power supply, and segments of the image tube voltage divider were bypassed with capacitors.

An example of the performance of the device is shown in Fig. 3.20. In the top half of Fig. 3.20 it is looking at a negative pulse on an oscilloscope screen. In the bottom half of Fig. 3.20 the picture is the same except that it is gated *on* only during the negative pulse. Only the negative pulse can be seen. The duration of the negative pulse is about 10 μsec. Tests of the device in observing discharge-tube plasmas

UNCLASSIFIED
PHOTO P-59975

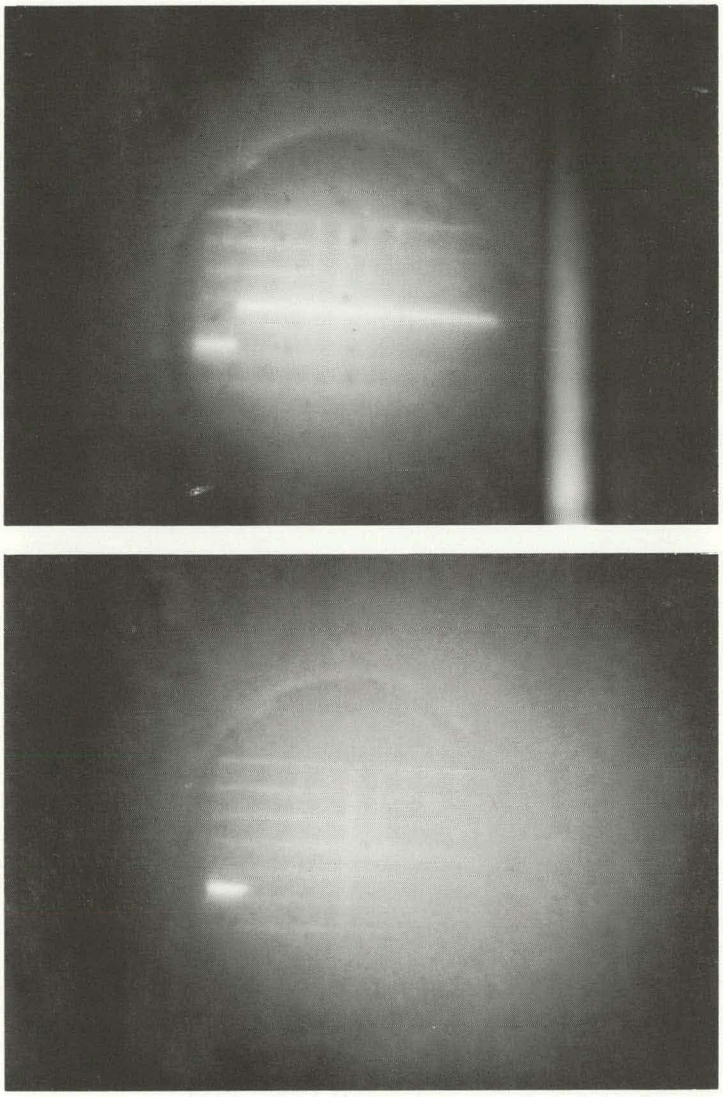

Fig. 3.20. Snooperscope Image of Oscilloscope Screen. Top, image of negative pulse; bottom, image of negative pulse – the Snooperscope is gated *open* only during the negative pulse; so only this section of the oscilloscope trace is seen. The negative pulse is about 10 μsec long. A short-persistence blue phosphor is used on the oscilloscope tube.

were successful, but no photographs were made at the time.

Extensive use of this stroboscopic shutter is planned in the study of oscillating discharge tubes, magnetically supported plasma columns, and calutron beams. In the event an oscillating plasma is nonluminous, a phosphor with a fast-decay constant could be placed where electrons or ions would cause it to glow and give evidence of fluctuations in electron or ion density.

4. Vacuum Arc Research

4.1 FUEL ION HEATING ANALOGY IN THE MAGNETICALLY CONFINED, STEADY-STATE CARBON ARC

J. R. McNally, Jr. M. R. Skidmore

Ionic temperatures up to 5×10^6 °K have been observed in a 16-ft-long, magnetically confined, low-pressure, steady-state carbon arc.[1] It is of interest to evaluate the heating of impurity gas fed as "fuel material" to such steady-state arcs in order to ascertain the degree of heating and equilibration attainable between "fuel" and carbon ions.

Our first experiments, made by use of a 96-in.-long arc for which ion temperatures up to 2.7×10^6 °K have been observed, gave inconclusive results, for hydrogen gas leaked into either the carbon anode or cathode. This result apparently stems from the indirect method available for observation; namely, the hydrogen ions must undergo a recombination process before radiating. The probability of recombination to the nth quantum level is approximately proportional to $1/n^3$, so that only about 1% of these can produce H_β quanta (λ 4861 A), which must then compete with radiation from excited, cool neutrals. The observed H_β line widths corresponded to less than 40,000°K, which is comparable to the kinetic energy of molecular dissociation fragments.

Helium was next studied, since the He^+ trapped in the arc can be directly excited by electrons. The 4-to-3 transition at λ 4686 A was investigated with a 50-cm Ebert spectrometer having 0.3-A or better resolution. Gas feed ($\gtrsim 3\,cm^3/min$) to anode, cathode, or the vacuum tank proper revealed marked broadening of the line, but cathode feed permitted arc operation at the lowest tank pressure. The observation point was 88 in. from the anode. The line half-width ranged from 1.25 to 1.68 A, while the λ 4647 A line of C^{2+} varied from 1.05 to 1.38 A, the larger half-widths being obtained at the lowest tank pressures. These line widths correspond to ion temperatures of (0.6, 1.0, 1.2, and 2.0) $\times 10^6$ °K respectively. Figure 4.1 shows the closeness of fit of the observed intensity points to a Doppler (Gaussian) profile, indicating that it may be meaningful to ascribe a temperature to these ions. The fine structure intensities shown were evaluated by the method of Bates and Damgaard.[2]

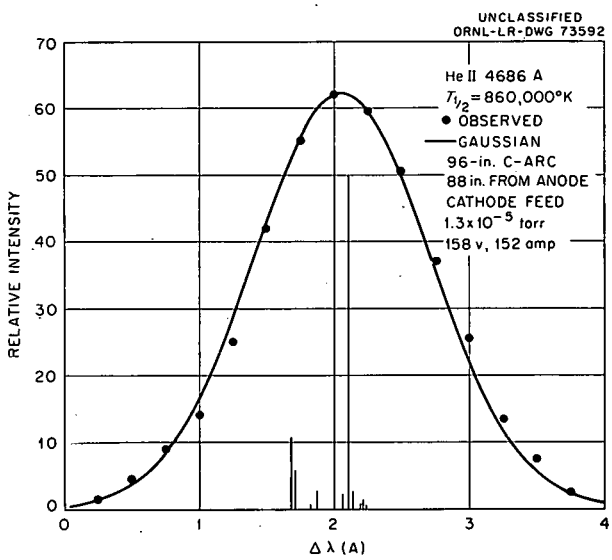

Fig. 4.1. Intensity Profile of He^+ λ 4686 A for a Transverse View of a 96-in. Carbon Arc in a Magnetic Field of 8300 gauss and with the Helium Gas Feed Through a Cathode Hole.

[1] J. R. McNally, Jr., *et al.*, *Thermonuclear Div. Semiann. Progr. Rept. Apr. 30, 1962*, ORNL-3315, p 45.

[2] D. R. Bates and A. Damgaard, *Phil. Trans. Roy. Soc. London, Ser. A* **242**, 101 (1949).

Cursory studies of nitrogen- and argon-fed carbon arcs showed that ion heating is dependent on the charge state of the ion. Ion temperatures, evaluated from line half-widths, vary with gas feed but for this 96-in. arc are of the order:

Ion	Temperature (°K) $\times 10^6$
C^+	2.0
N^+	1.5
A^+	1.4
C^{2+}	2.5
N^{2+}	2.5
A^{2+}	2.6
N^{3+}	2.5

This strong dependence of ion heating on charge state suggests that the heating mechanism is electrostatic in origin. Other experiments show that heating is more pronounced transverse to the arc than parallel with the arc, indicating that the electric fields are primarily radial, which is in agreement with probe experiments.[3] The closer agreement of the carbon ion temperatures may be due to rapid resonance charge-transfer processes among the high-density carbon ions, which cause the ions to lose more rapidly their specific charge identity.

These experiments indicate strongly that cold thermonuclear-fuel gas may be heated rapidly to high temperatures in a hot plasma having high, transverse electric fields. The experiments, and others, suggest that the carbon and "fuel" ions flow readily along magnetic flux lines against the axial electric field of the arc – a result in agreement with $nKT \gg \xi^2/8\pi$. These ion feed and heating observations may have an important bearing on the problem of feeding and heating fuel material in a steady-state fusion reaction.

We plan to rebuild the 16-ft arc facility, or possibly extend it, in order to make feed-gas heating studies at higher ion temperatures. We may also examine the heating of deuterium by study of fusion processes (the anticipated reaction rate is expected to be quite low).

---

[3] J. F. Potts *et al.*, *Thermonuclear Project Semiann. Rept. Jan. 31, 1959*, ORNL-2693, p 41.

5. Ion Production, Acceleration, and Injection

5.1 HIGH-CURRENT ION-BEAM INJECTION

R. C. Davis E. C. Moore
R. R. Hall O. B. Morgan
G. G. Kelley R. F. Stratton
D. C. Weaver

The efforts of this group have been divided between injecting an ion beam into DCX-2 and doing basic injection studies at the High-Intensity-Beam Facility. Both of these facilities utilize the 600-kv 1-amp power supply, and they cannot be operated simultaneously.

The DCX-2 injection system has been operated at total ion currents up to 150 ma while injecting into the plasma region. Calorimetric measurements indicate that the maximum H_2^+ ion current injected into the machine does not increase significantly as the total current is increased above 100 ma. The maximum H_2^+ beam injected has been approximately 45 ma out of a total ion beam of 90 ma and only 50 ma with a total of 150 ma. Whether this is the actual component ratio produced by the ion source or whether some of the H_2^+ component is lost inside the injection duct has not been determined.

The original accelerator tube developed for high-current injection was successfully used on DCX-2 until October. At this time the tube started to become unstable because of external breakdowns along the surface of the insulators. Two of the insulators had developed exterior surface conductive paths that could not be removed by normal cleaning procedures. The tube was replaced with one being developed that uses epoxy skirts cast around the porcelain insulators, Figs. 5.1 and 5.2. This tube has operated on DCX-2 at above 600 kv but not reliably above 570 kv. Several minor modifications are in the process of being tested which, based on prior experience on a similar tube, should allow satisfactory operation at 600 kv. Except for a few runs in which the accelerator operated with no involuntary shutdowns, performance has left something to be desired in spite of the fact that the same arrangement works very well at the High-Intensity-Beam Facility. Discharges may initiate either internally or externally, and under certain conditions it is difficult to distinguish between them. The problem of achieving a more desirable level of stability, which will allow experiments to be conducted without interruption, will be pursued on both of the intense-beam facilities.

For several reasons, particularly in connection with DCX-2 diagnostics, it is desirable to be able to measure the beam current as a function of time with a resolution of the order of 10 μsec or better. This current cannot be measured in the ground leg of the 600-kv supply because of large ac ground currents associated with the nature of the supply itself. For this reason an FM link was developed to transmit current information from the 600-kv level to ground. The scheme uses two commercial FM receivers connected as shown in Fig. 5.3. One of the receivers has its oscillator shifted downward by 21.4 Mc so that when the receivers are tuned to receive each other's local oscillator the beat note in the mixer is 10.7 Mc. The feedback loop providing AFC in the transmitting unit is closed with additional gain provided by a transistor amplifier. A signal voltage proportional to the current to be measured is obtained across a 10-ohm shunt. This voltage is connected in series with the discriminator output in the feedback loop. In this way the oscillator frequency is caused to shift by the amount necessary to provide a voltage from the discriminator to approximately cancel the signal. Loop gain is sufficiently high that the accuracy is better than 1%. The unit used as a receiver detects this frequency shift and produces a corresponding dc

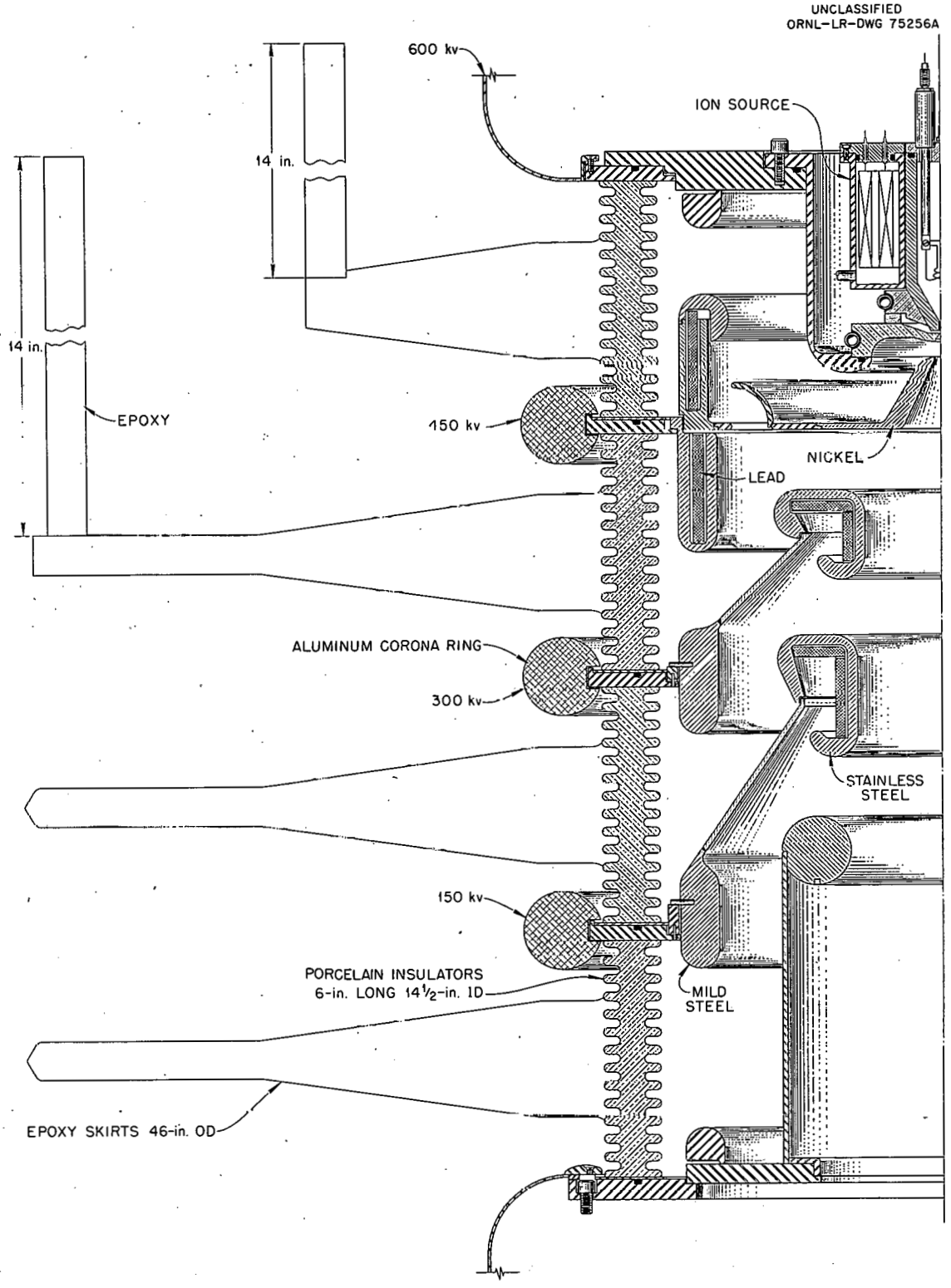

Fig. 5.1. 600-kv Accelerator Tube, Mark IV.

UNCLASSIFIED
PHOTO 38944

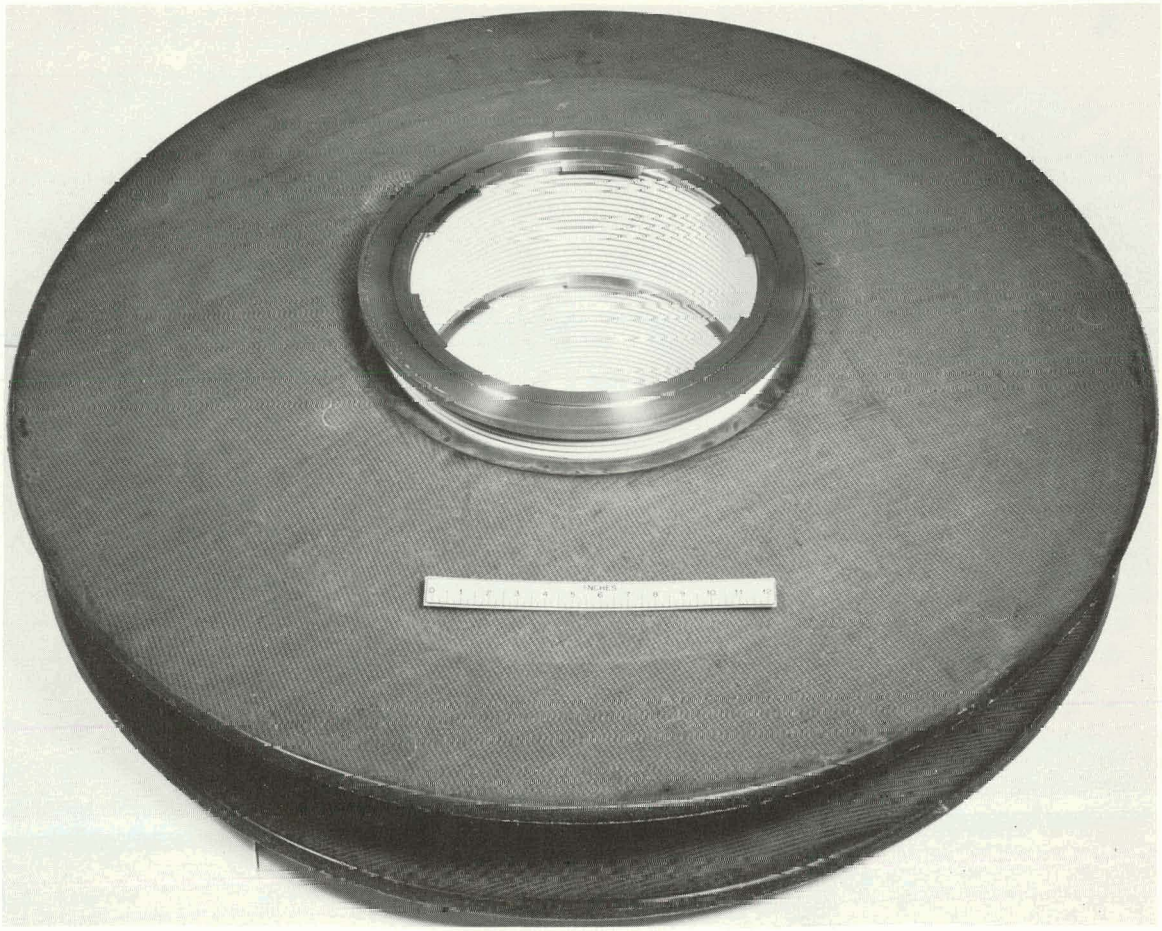

Fig. 5.2. Two Insulator Sections for a 600-kv Accelerator Tube.

output voltage. The discriminator output is identical with the shunt voltage up to more than 5 v and to within less than 1%. These units have been operated at distances exceeding 100 ft, but corona noise from the power supply is troublesome at this distance when currents of less than 5 ma are to be measured. The transmission path in use now is about 25 ft.

Equipment is installed at the High-Intensity-Beam Facility for doing high-current analysis, Fig. 5.4. This analysis is achieved by using the mass-dependent focal length of the magnetic solenoid lens to pass preferentially only one beam component through the funnel. In some preliminary checkout experiments the beam analysis appeared to be approximately 50 ma of H_2^+ out of a total beam of 150 ma. These results will be more thoroughly evaluated as soon as a new accelerator tube is installed to replace the one transferred to DCX-2 and when operating time is available on the 600-kv power supply. In the event that these preliminary results are correct, new electrodes have been built for the duoplasmatron which can be used for optimizing the H_2^+ beam fraction at total ion currents in excess of 100 ma. The equipment for doing beam emittance work[1] has been installed. Unfortunately, time has not permitted the study of the anomalous spreading of a beam beyond a crossover reported earlier.[2,3] The 600-kv power supply must be shared with DCX-2. It is not

---

[1] R. C. Davis *et al.*, *Thermonuclear Div. Semiann. Progr. Rept. Apr. 30, 1962*, ORNL-3315, pp 59–60.

[2] G. G. Kelley *et al.*, *Thermonuclear Div. Semiann. Progr. Rept. Jan. 31, 1961*, ORNL-3104, p 19.

[3] G. G. Kelley and O. B. Morgan, *Phys. Fluids* 4(11), 1446–47 (1961).

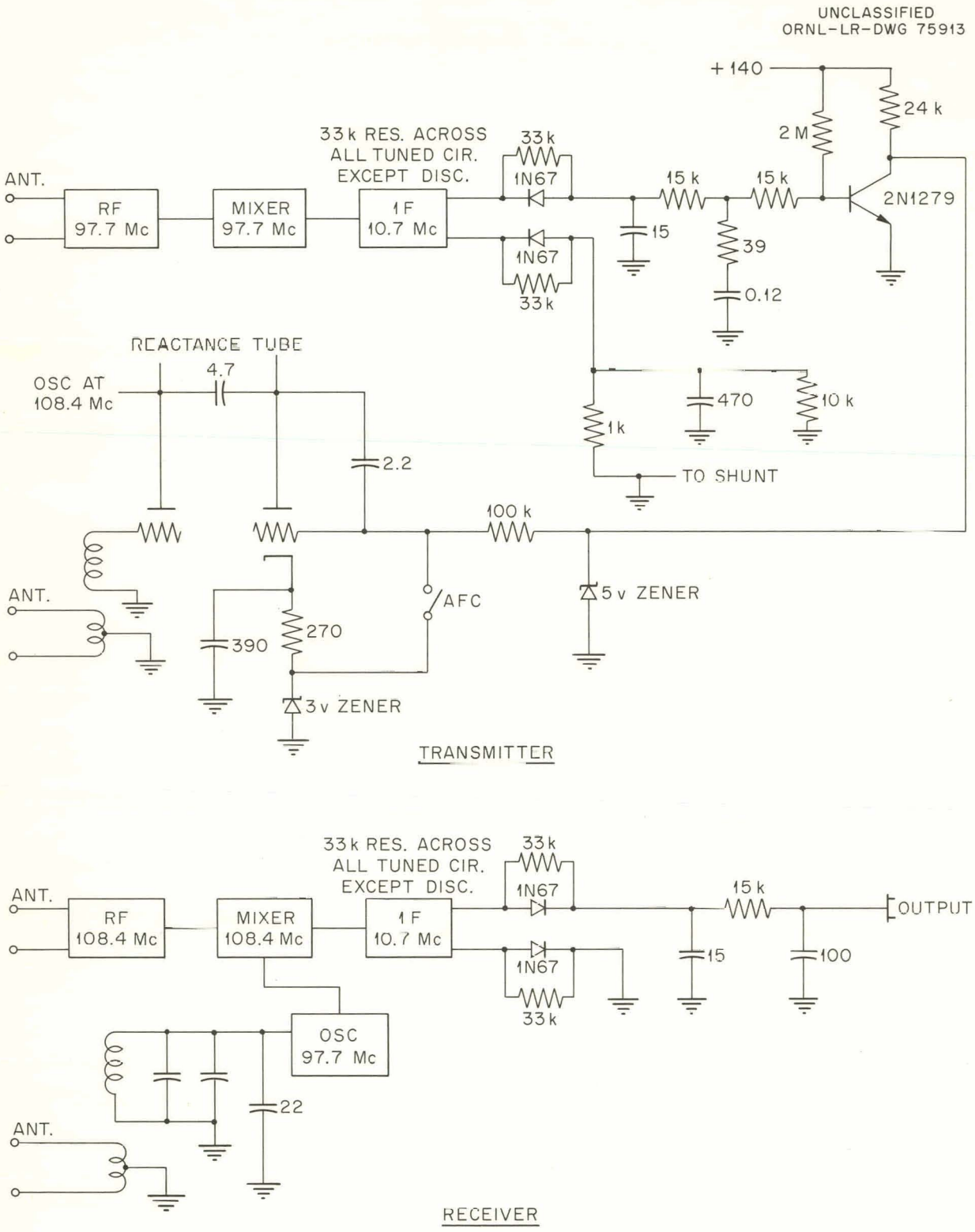

Fig. 5.3. Block Diagram of FM Telemetry Link.

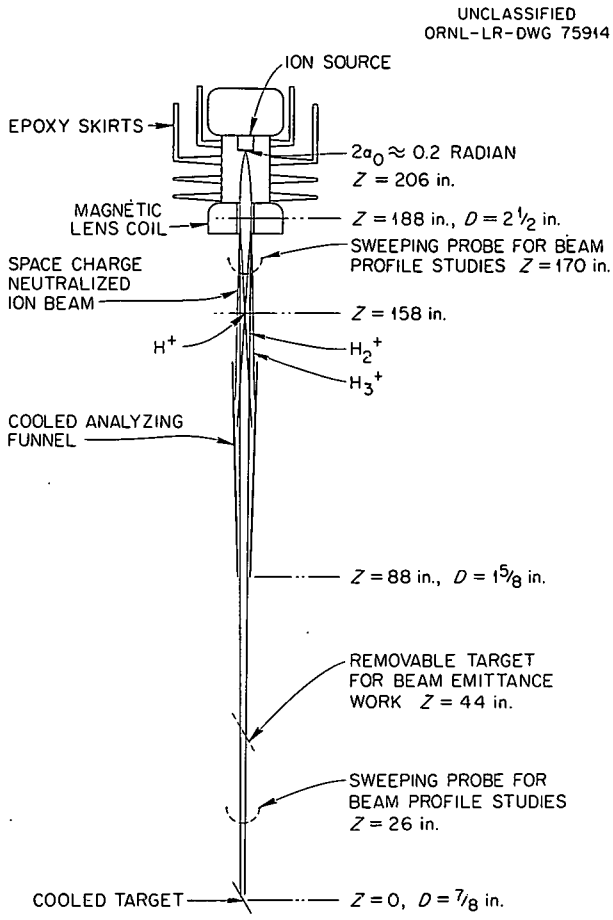

Fig. 5.4. Typical 100-ma Beam Profiles in the High-Intensity Beam Facility.

observed under the present beam conditions, Fig. 5.4. As soon as the information needed for DCX-2 can be obtained with the present facility, this effect will be studied again.

5.2 100-kev NEUTRALIZED-BEAM ACCELERATOR

E. L. Earley[4] V. J. Meece
J. W. Flowers[5] W. L. Stirling

Operation of the 100-kev accelerator[6] at accelerating voltages in the 10- to 20-kev range has given satisfactory results. In all experiments to date, the accelerating electrode has been removed; the lower-coil can shield serves in this capacity. This allows a maximum interaction path length between the ions and injected electrons.

Figure 5.5 shows the major components and their electrical connections. As explained in previous reports,[7] the electrons, which originate in the electron gun, are accelerated into the positive-ion-source region. They pass through the ion source and are decelerated by the electric field as the ions are simultaneously accelerated. The booster voltage supplies the energy lost by the electrons due to collective interaction of the electron beam with the plasma existing in the ion source.

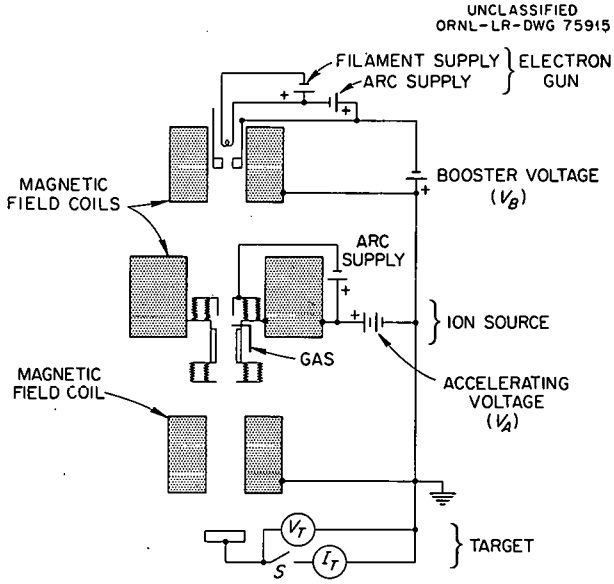

Fig. 5.5. Electrical Connections of the Neutralized-Beam Accelerator.

Table 5.1 contains typical data obtained for a 15-kev hydrogen-ion beam. The electron-gun arc conditions (argon) were 0.5 amp at 200 v; the ion-source arc (hydrogen) was 15 amp at 360 v. Target power was measured calorimetrically, and the algebraic signs under "target current" indicate electron current, −, and positive-ion current, +. These results indicate an increase by a factor

[4] On loan from Y-12.

[5] Consultant, University of Florida, Gainesville.

[6] C. W. Blue *et al., Thermonuclear Div. Semiann. Progr. Rept. Apr. 30, 1962*, ORNL-3315, p 59.

[7] C. W. Blue *et al., Thermonuclear Div. Progr. Rept. Oct. 31, 1961*, ORNL-3239, p 67.

Table 5.1. Low-Voltage Operating Characteristics of a Neutralized-Beam Accelerator

Electron Gun	Ion Source	Booster Voltage (v)	Accelerating Voltage (kev)	Target Power (w)	Target Current (ma)
On	On	350	15	92	−62
On	On	75	15	264	−51
Off	On	75	15	99	+10
On	Off	75	15	118	−55

of about 3 in target power with electron injection over that obtained without electron injection. This number has been increased to a factor of 4 to 5 with a target power equivalent to 18 to 20 ma. The calculated space-charge limited current is approximately 5 ma.

Table 5.1 shows that the target current is negative when the power delivered to the target is maximum. However, the potential of the target, V_t, as read by the electrostatic voltmeter, remained at ground upon opening switch S, Fig. 5.5. In addition, the power to the target remained constant.

It is possible to adjust the target current to zero with the switch closed. Figure 5.6 shows the variation with booster voltage of target power and target current (electron current read from meter) with the arc (hydrogen) and the accelerating voltage held constant. The curves depict a smooth transition from the low-power to the high-power mode. The damage to various meters (before adequate filtering components were installed) indicates an increase in rf generation at the lower booster-voltage values. Probes are now being installed to monitor the rf.

The variation of target power with acceleration voltage does not yield a current output which varies with the three-halves power of the voltage as predicted for space-charge limited operation. In the experiment from which Fig. 5.2 was compiled, the target current calculated from power measurements fell from 20 ma at 10 kev to 17 ma at 20 kev; the booster voltage was 90 v, and all the other parameters were held constant. Within experimental error, this is a constant target current.

As reported in ref 7, a strong interaction had been observed between the electron stream and

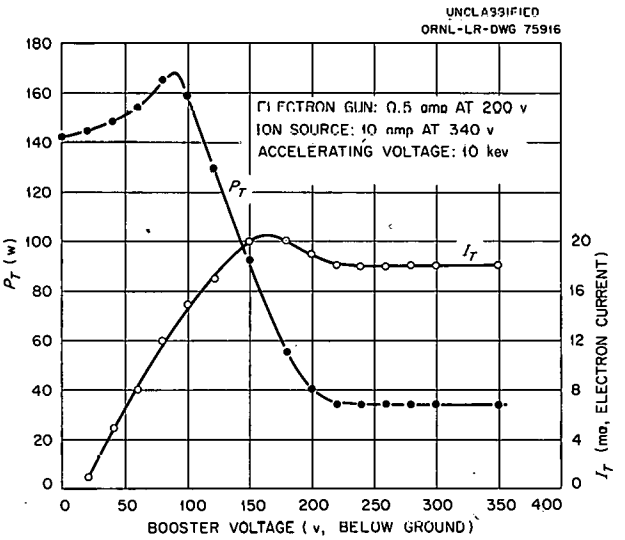

Fig. 5.6. Neutralized-Beam Source Output vs Booster Voltage.

the ion-source plasma when the latter was an argon arc. However, attempts to repeat this observation have not been successful thus far. The target power increases uniformly by about 25% as the booster voltage is increased from 0 to 350 v. This is in marked contrast to the hydrogen results depicted in Fig. 5.6. For zero booster voltage with argon operation, the target current calculated from the power measurements is equal to that expected from space-charge limited operation. Preliminary results from operation with helium and nitrogen are similar to those obtained with argon. The performance with deuterium will be observed next. The variation of ion current output with accelerating-gap distance will also be studied; the original argon experiments were performed with

an accelerating gap about one-tenth as long as that employed in the results reported here.

The results of the low-voltage operation of the accelerator show thus far that there are three phenomena to be reconciled: the variation of output power (1) with the mass of the ion being accelerated, (2) with the electron beam velocity as determined by the booster voltage, and (3) with the electron beam velocity as determined by the accelerating voltage.

The observation of a mass-dependent beam-plasma interaction is not surprising. However, the large variation in the observations of this experiment with those reported in ref 7 illustrates that more experimental information is needed in order to understand the variations observed.

A qualitative explanation of the variation of power output with electron beam velocity may be speculated as follows. On a single-particle basis, the accelerating voltage determines the velocity of the electrons at every point in the accelerator; the booster voltage has very little effect percentage-wise on this velocity, but it does determine whether an electron reaches the target or whether it turns around to assume an oscillatory path until it is scattered from the system. Thus at 350 v booster voltage, the electrons reach the target. Upon lowering the booster voltage, a point is reached at which the electrons start to oscillate, and in so doing they interact with the ion beam and/or secondary plasma associated with the beam, resulting in a favorable increase in power output. This interaction occurs most probably in a region in space very close to ground potential, with the electrons being scattered from the system before they assume oscillatory paths with appreciably decreased amplitude. A change in accelerating voltage only changes the interaction path length or time and produces no measurable interaction between the electron beam and the arc plasma in the ion source itself. This latter statement leads one to assume that the plasma in the ion source has a hollow cylindrical geometry of rather low density along the axial path which the electron beam traverses. The electrode geometry of the ion source makes such an assumption plausible.

The beam-plasma interaction described above makes no prediction about the ion energy distribution. All calculations of target current from measured target power assume a monoenergetic ion beam having the applied accelerating potential.

6. Theory and Computation

6.1. EFFECT OF A SPREAD IN CYCLOTRON FREQUENCIES ON THE CYCLOTRON RESONANCE INSTABILITY

E. G. Harris [1]

Introduction

The dispersion relation found by Burt and Harris [2] can be written

$$\frac{1}{\omega_{pe}^2} = \frac{1}{\omega^2} + \frac{m/M}{(\omega - l\omega_{ci})^2} = g(\omega) . \qquad (1)$$

In deriving this equation, it was assumed that the ions move in concentric Larmor orbits with their centers on the z axis. They fill a cylindrical shell with uniform density. The electrons were assumed to be cold. Perturbations were assumed proportional to $e^{ik_z z - il\theta + i\omega t}$ and $k_z \gg l/R$, where R is the mean radius of the shell.

The real roots of Eq. (1) can be found graphically by plotting $g(\omega)$ vs ω and seeing where it intersects the horizontal line at $1/\omega_{pe}^2$ as shown in Fig. 6.1. When ω_{pe} becomes sufficiently large, two of the real roots disappear from the figure, indicating that these roots have become complex. The criterion for this is easily shown to be

$$l\omega_{ci} < \omega_{pe}\,[1 + (m/M)^{1/3}]^{3/2} \approx \omega_{pe} .$$

This instability is sometimes thought of as a kind of resonance between electron plasma oscillations at frequency ω_{pe} and ion cyclotron oscillations at frequency $l\omega_{ci}$. This suggests that if there is a spread in cyclotron frequencies due to a nonuniform magnetic field, then many of the particles will be out of resonance and the coherence of the oscillation will be destroyed. In any magnetic-mirror machine the field is nonuniform owing to the presence of magnetic mirrors.

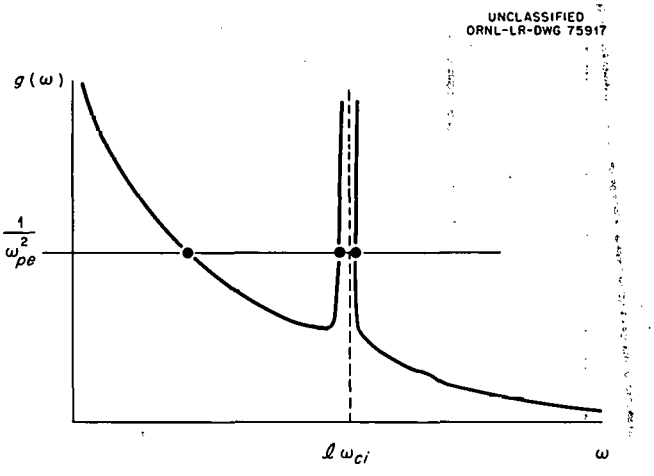

Fig. 6.1. Graphic Solution of Dispersion Relation for Uniform Magnetic Field.

We shall investigate the effect of a spread of cyclotron frequencies by assuming that Eq. (1) can be replaced by

$$\frac{1}{\omega_{pe}^2} = \frac{1}{\omega^2} + \frac{m}{M}\int \frac{f(\omega_{ci})\, d\omega_{ci}}{(\omega - l\omega_{ci})^2} , \qquad (2)$$

where $f(\omega_{ci})\, d\omega_{ci}$ is the fraction of ions with cyclotron frequency in the range $d\omega_{ci}$ about ω_{ci}. In writing Eq. (2) we have ignored the fact that ω_{ci} is actually a function of position in the machine. The effect of this omission is largely unknown. We hope that results obtained from Eq. (2) will be at least qualitatively correct.

It should be noted that allowing for a spread in ω_{ci} as we have done has the same qualitative effect as allowing a spread in ion velocities parallel to the magnetic field, since this would

[1] Consultant, University of Tennessee.

[2] Philip Burt and E. G. Harris, *Phys. Fluids* 4, 1412 (1961).

give the dispersion relation

$$\frac{1}{\omega_{pe}^2} = \frac{1}{\omega^2} + \frac{m}{M}\int \frac{f(V_z)\, dV_z}{(\omega - l\omega_{ci} - k_z V_z)^2} . \quad (3)$$

In this case a spread in frequencies is obtained because of the Doppler shift. A particle with the velocity V_z will see the frequency $l\omega_{ci} + k_z V_z$ instead of $l\omega_{ci}$.

Analysis of Eq. (2)

We shall first assume the rectangular distribution (see Fig. 6.2)

$$f(\omega_{ci}) = \begin{cases} \dfrac{1}{2\alpha} & |\omega_{ci} - \omega_0| < \alpha , \\ 0 & |\omega_{ci} - \omega_0| > \alpha . \end{cases} \quad (4)$$

The integral in Eq. (2) is easily carried out with the result

$$\frac{1}{\omega_{pe}^2} = \frac{1}{\omega^2} + \frac{m/M}{(\omega - l\omega_0)^2 - l^2\alpha^2} . \quad (5)$$

We plot $g(\omega)$ in Fig. 6.3. It is seen from Fig. 6.3 that the plasma first becomes unstable when ω_{pe} becomes greater than $l(\omega_0 - \alpha)$ but then may become stable again when ω_{pe} becomes still greater. We shall now give a more quantitative analysis of Eq. (5). We write it as

$$(\omega^2 - \omega_{pe}^2)[(\omega - l\omega_0)^2 - l^2\alpha^2] = (m/M)\,\omega_{pe}^2\omega^2 . \quad (6)$$

Introduce the dimensionless variables

$$\begin{aligned} Z &= \omega/l\alpha , \\ Z_p &= \omega_{pe}/l\alpha , \\ Z_c &= l\omega_0/l\alpha = \omega_0/\alpha , \\ \delta &= m/M . \end{aligned} \quad (7)$$

Equation (6) may be written

$$(Z - Z_p)(Z + Z_p)(Z - Z_c - 1)(Z - Z_c + 1) = \delta Z_p^2 Z^2 . \quad (8)$$

We are interested in roots in the neighborhood of

$$Z \approx Z_p \approx Z_c - 1 ; \quad (9)$$

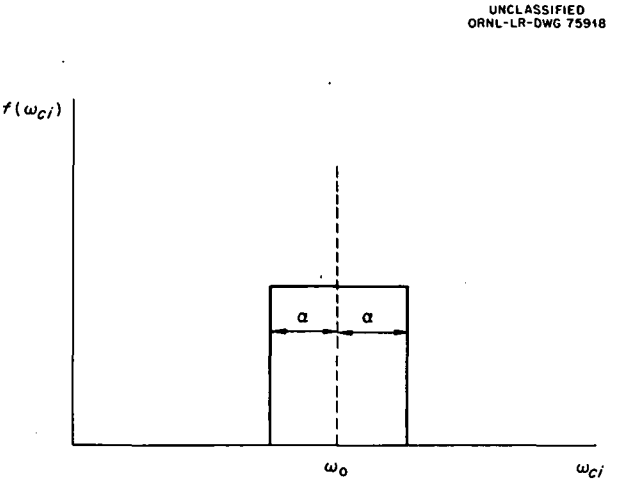

Fig. 6.2. Assumed Cyclotron Frequency Distribution Approximating Field Nonuniformity.

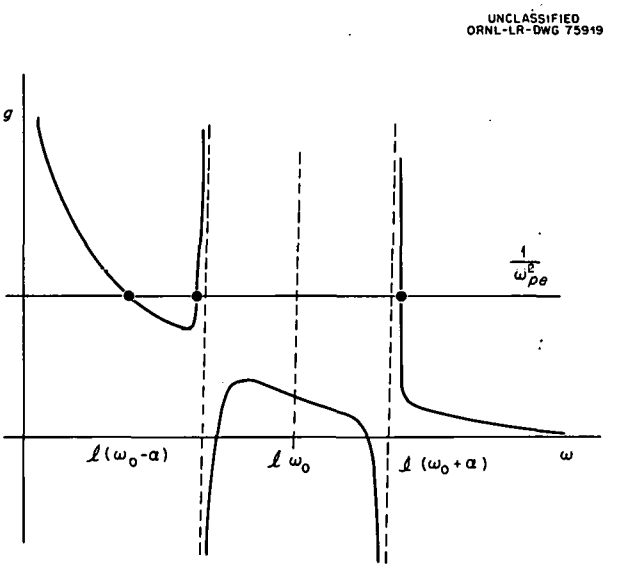

Fig. 6.3. Graphic Solution of Dispersion Relation Assumed for Cyclotron Frequency Distribution of Fig. 6.2.

so we write

$$(Z - Z_p)(Z - Z_c + 1) = \frac{\delta Z_p^2 Z^2}{(Z + Z_p)(Z - Z_c - 1)} \approx -\frac{\delta Z_p^3}{4} . \quad (10)$$

Solving this quadratic equation we obtain

$$Z = \left[\frac{Z_p + (Z_c - 1)}{2}\right] \pm \sqrt{\left[\frac{Z_c - (Z_c - 1)}{2}\right]^2 - \frac{\delta Z_p^3}{4}} . \quad (11)$$

It is seen from Eq. (11) that Z is complex if

$$| Z_p - (Z_c - 1)| < \delta^{1/2} Z_p^{3/2} , \quad (12)$$

or

$$| \omega_{pe} - l(\omega_0 - \alpha)| < \frac{\delta^{1/2}\omega_{pe}^{3/2}}{(l\alpha)^{1/2}} = \omega_{pi}\left(\frac{\omega_{pe}}{l\alpha}\right)^{1/2} . \quad (13)$$

We find for the maximum growth rate

$$(\mathcal{I}mZ)_{max} = \sqrt{\frac{\delta Z_p^3}{4}} \quad (14)$$

or

$$(\mathcal{I}m\omega)_{max} = \frac{\omega_{pi}}{2}\sqrt{\frac{\omega_{pe}}{l\alpha}} . \quad (15)$$

These results are not valid unless the approximation in Eq. (9) is a good one.

We now write Eq. (5) as

$$\frac{1}{Z_p^2} = \frac{1}{Z^2} + \frac{\delta}{(Z - Z_c)^2 - 1} = g(Z) . \quad (16)$$

The roots corresponding to $g(Z) = 0$ (infinite plasma density) are

$$Z = \frac{Z_c}{1+\delta} \pm \sqrt{\left(\frac{Z_c}{1+\delta}\right)^2 - \frac{Z_c^2 - 1}{1+\delta}} . \quad (17)$$

The roots coincide when

$$Z_c = \sqrt{\frac{1}{\delta} + 1} \approx \sqrt{\frac{1}{\delta}} = \sqrt{\frac{M}{m}} . \quad (18)$$

If $Z_c > \sqrt{M/m}$, then Z is complex for infinite Z_p. Therefore the plasma cannot be stabilized by increasing the density.

We can summarize these results by indicating the stable and unstable regions in the $Z_p - Z_c$ plane. This is done in Fig. 6.4.

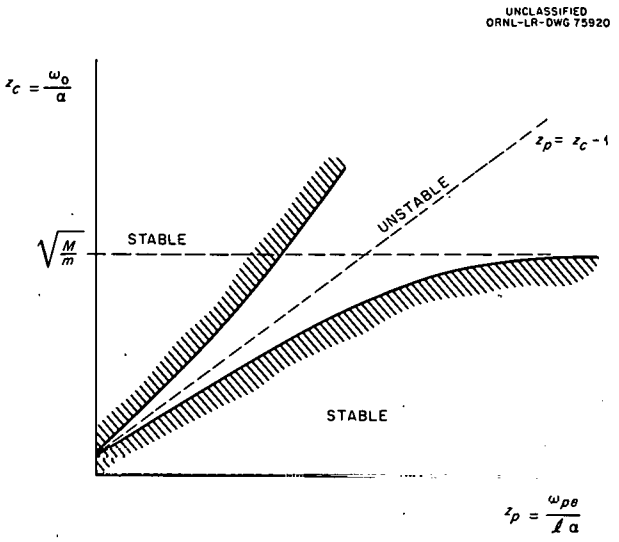

Fig. 6.4. Map of Stable and Unstable Zones if Field Nonuniformity Is Approximated by Cyclotron Frequency Distribution of Fig. 6.2. ω_{pe} is the plasma frequency.

We next inquire as to what extent these results are a consequence of the assumption of a rectangular distribution, Eq. (4). We shall assume a Gaussian distribution of width 2α and compare the results obtained with the previous results. Let

$$f(\omega_{ci}) = \frac{1}{(2\pi\alpha^2)^{1/2}} e - (\omega_{ci} - \omega_0)^2/2\alpha^2 . \quad (19)$$

Substituting into Eq. (2) we obtain

$$\frac{1}{\omega_{pe}^2} = \frac{1}{\omega^2} + \frac{M}{Ml^2\alpha^2}\left[R\left(\frac{\omega - l\omega_0}{l\alpha}\right) - iI\left(\frac{\omega - l\omega_0}{l\alpha}\right)\right] , \quad (20)$$

or

$$\frac{1}{Z_p^2} = \frac{1}{Z^2} + \delta\left[R(Z - Z_c) - iI(Z - Z_c)\right] , \quad (21)$$

where

$$R(Z) = -1 + Ze^{-Z^2/2}\int_0^Z e^{X^2/2}\, dX , \quad (22)$$

$$I(Z) = \sqrt{\frac{\pi}{2}} Ze^{-Z^2/2} . \quad (23)$$

The boundary between stable and unstable regions of the $Z_p - Z_c$ plane can be found by assuming that ω (hence Z) is real. Then,

$$I(Z - Z_c) = 0 . \tag{24}$$

Hence,

$$Z = Z_c , \tag{25}$$

and from Eqs. (21) and (22)

$$\frac{1}{Z_p^2} = \frac{1}{Z_c^2} - \delta , \tag{26}$$

which gives

$$Z_c = \frac{Z_p}{\sqrt{1 + \delta Z_p^2}} \tag{27}$$

as the boundary between stable and unstable regions. This is sketched in Fig. 6.5.

UNCLASSIFIED
ORNL-LR-DWG 75921

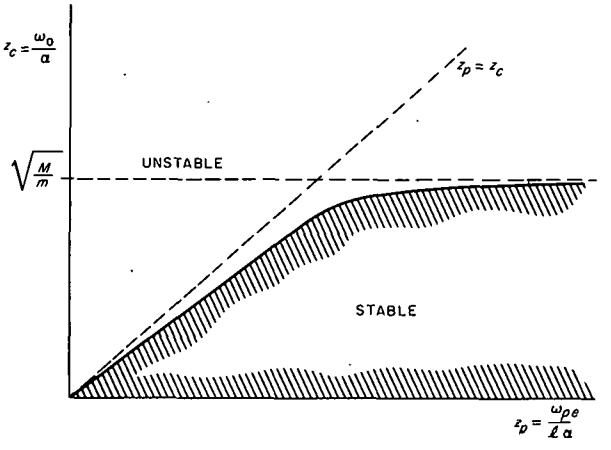

Fig. 6.5. Map of Stable and Unstable Zones If Field Nonuniformity Is Approximated by a Cyclotron Frequency Distribution of Gaussian Shape, Centered at ω_0, One-Half Width α. ω_{pe} is the plasma frequency.

It is seen that the plasma is stable at high densities if $Z_c < \sqrt{M/m}$, but unstable at zero density in contrast to the previous case. This is because the Gaussian distribution, Eq. (19), contains all frequencies, whereas the lowest frequency contained in Eq. (4) was $(\omega_0 - \alpha)$.

Let

$$Z_0 = \frac{Z_p}{\sqrt{1 + \delta Z_p^2}} . \tag{28}$$

From Eq. (21) we obtain

$$Z = \frac{Z_0}{\sqrt{1 - \delta Z_0^2 [R(Z - Z_c) + 1 - il(Z - Z_c)]}} . \tag{29}$$

For

$$\delta Z_0^2 << 1 \tag{30}$$

that is, $\omega_{pi}^2 << l^2 \alpha^2$, we find that approximately

$$Z \approx Z_0 \left\{ 1 - \frac{\delta Z_0^2}{2} [R(Z_0 - Z_c) - il(Z_0 - Z_c)] \right\}, \tag{31}$$

$$\mathcal{I}mZ = \delta Z_0^3 \sqrt{\frac{\pi}{8}} (Z_c - Z_0)\, e^{-(Z_c - Z_0)^2/2} . \tag{32}$$

Discussion

In DCX-1 the mirror ratio is about 2; so if ω_0 is taken to be the average cyclotron frequency and α the difference between ω_0 and the cyclotron frequency at the mirrors, then $\alpha = \frac{1}{3}\omega_0$ and $Z_c = \omega_0/\alpha = 3$. This is much below $\sqrt{M/m}$ (= 43 for protons). If we assume a rectangular distribution, we may use Eq. (12) in the form

$$Z_c - 1 - \delta^{1/2} Z_p^{3/2} < Z_p - 1 + \delta^{1/2} Z_p^{3/2} . \tag{33}$$

We may use $\delta << 1$ to write that for instability approximately

$$2(1 - \sqrt{2\delta}) < Z_p < 2(1 + \sqrt{2\delta}) , \tag{34}$$

or

$$\tfrac{2}{3} l\omega_0 (1 - \sqrt{2\delta}) < \omega_{pe} < \tfrac{2}{3} l\omega_0 (1 + \sqrt{2\delta}) . \tag{35}$$

For protons, $\sqrt{2\delta} \approx \frac{1}{3}$.

It would seem that there is a very narrow band of densities for which the plasma is unstable.

The Gaussian distribution gives qualitatively similar results.

Caution should be used in accepting these results because of the drastic nature of the

simplifying assumptions that were made. However, there is an indication that machines such as DCX and OGRA may become stable to this type of instability at sufficiently high density.

6.2 NONLINEAR STABILITY AND LYAPUNOV'S THEORY

T. K. Fowler

An adaptation of the orbit stability theory of Lyapunov to the Vlasov equation has been completed, and a paper has been prepared.[3] Besides the previously reported theorems giving conditions for stability with respect to the linearized equations (linear stability),[4] nonlinear stability has been shown to be a consequence of *strong* linear stability whenever modes actually damp to zero in the linear approximation. The latter happens, for example, if effects of collisions and particle loss are retained in the Vlasov equation, or if Landau damping occurs. By *strong* linear stability, we mean that electric- and magnetic-field perturbations, together with all velocity moments of the phase space distribution, remain bounded in time at each point of space.

That linear stability with damping promotes nonlinear stability can be understood from the following example. Consider the stability of the solution $x = 0$ of the ordinary differential equation,

$$\frac{dx}{dt} = -ax + bx^2 , \qquad (1)$$

where a is positive. The linear solution, $\exp(-at)$, damps. From the inequality,

$$\frac{dx}{dt} \leqq (-a + |b||x|)x , \qquad (2)$$

it is clear that the nonlinear solution also damps if, at $t = 0$, $|b||x|_0 < a$. Then $|x| \leqq |x|_0$ for all time and $(-a + |b||x|) < 0$ for all time. That is, the nonlinear solution damps if initially the nonlinear growth rate, $|b||x|_0$, is less than the linear damping rate a. But, since the nonlinear growth depends on the initial perturbation, the condition can always be satisfied for finite a, and nonlinear stability is assured for all perturbations sufficiently small at $t = 0$. This is the nature of Lyapunov's criterion, the proof of which is given by Bellman[5] and follows the reasoning above. Evidently, the magnitude of nonlinearly stable perturbations becomes small if either the linear damping is small or the magnitude b of the nonlinear term is large. But the allowable perturbation guaranteed stable by the theorem is at least finite, and certainly for plasmas the criterion is pessimistic.

6.3 STABILITY OF COLLISIONLESS PLASMAS AGAINST EXPONENTIAL GROWTH

T. K. Fowler

It has been shown that, in principle, stability against exponential growth can always be proved by the existence of a Lyapunov function. The result applies to the linearized Vlasov equation and to moment equations. Unlike mode analysis, stability analysis by means of Lyapunov functions does not require knowledge of solutions of the equations. The MHD (magnetohydrodynamic) energy principle, applicable to spatially complicated situations inaccessible to mode analysis, is an example of the technique. One might hope that our existence theorem for Lyapunov functions suggests that complicated situations may also be analyzed employing the Vlasov equation.

The class of Lyapunov functions shown to exist are quadratic forms in perturbations. Consider the linearized Vlasov equation. If $f(\vec{x}, \vec{v}, t)$ is the phase space distribution perturbation, and $(f_1, f_2) = \int d\vec{x}\, d\vec{v}\, f_1^* f_2$, then (f, Hf) is a Lyapunov function if H is a positive definite Hermitian operator independent of t and $d(f, Hf)/dt \leqq 0$. If such an H exists, (f, f) is at least bounded for all time, implying stability. For example, if on the contrary $f \propto \exp \lambda t$ with $Re\ \lambda > 0$, $(f, f) \propto \exp 2Re\lambda t$ would blow up exponentially. Thus the existence of a Lyapunov function is sufficient for stability. The more interesting result is the following necessary condition. If, for all f, (f, f) in fact damps for all time, and fast enough so

[3] Accepted for publication in *Journal of Mathematics and Physics.*

[4] T. K. Fowler, *Phys. Fluids* **4**, 1393 (1961); **5**, 249 (1962); also *Thermonuclear Div. Semiann. Progr. Rept. Apr. 30, 1962*, ORNL-3315, p 64.

[5] R. Bellman, *Stability Theory of Differential Equations*, pp 78–85, McGraw-Hill, New York, 1953.

that $\int_0^\infty dt\ (f, f) < \infty$, then there exists a Lyapunov function (f, Hf).

Now, we have only shown that Lyapunov functions necessarily exist if (f, f) damps. But, in the absence of collisions, this quantity does not damp. To apply our results to collisionless plasmas, we introduce artificial damping by the transformation $g = f \exp(-\mu t)$, $\mu > 0$, and apply our theorems to the modified equation satisfied by the g's. If (f, f) grows *more slowly* than exp $2\mu t$, (g, g) is integrable on $0 < t < \infty$, so that the existence theorem for Lyapunov functions applies. Conversely, if a Lyapunov function for the g's exists, (f, f) grows no faster than exp $2\mu t$. By choosing μ small but finite, one obtains for all practical purposes a criterion against exponential growth of perturbations.

6.4 STABILITY OF INHOMOGENEOUS COLLISIONLESS PLASMA

Y'akov Shima

The stability of inhomogeneous collisionless plasmas is being investigated by a method employing the equilibrium constants of motion.[6] For the case where the distribution function f_0 depends on the three constants of motion p_θ, $v_\perp$, v_z (p_θ – canonical angular momentum, $v_\perp^2 = v_x^2 + v_y^2$, the constant external magnetic field is in the z direction), the problem reduces to investigating a one-dimensional integral equation.[7]

It has been shown that when f_0 does not depend on p_θ (infinite, homogeneous, anisotropic plasma) the integral equation reduces to a dispersion relation.[8] The integral equation reduces to dispersion relations also in the case when f_0 for ions describes an infinite anisotropic plasma rotating with the cyclotron frequency around the z axis [f_0 is then of the form $f_0(v_\perp^2 + 2p_\theta\omega_c, v_z)$, where ω_c is the cyclotron frequency]. These dispersion relations differ from the former ones only in that in the ion contribution the imaginary part of the Laplace transform p is Doppler-shifted by an integral multiple of ω_c.

6.5 CORRELATION DAMPING

David Montgomery[9]

The Vlasov (or "collisionless Boltzmann") equation describes a limit in which the effects of particle individuality are lost. Past attempts to assess the effect of two-body encounters on such collective phenomena as plasma oscillations and instabilities have usually proceeded from a model in which *isolated* two-body encounters played a dominant role. This is quite unsatisfactory, since such encounters do not take place in an inhomogeneous plasma.

The first two BBGKY equations provide, insofar as ternary correlations are negligible, a rigorous framework for describing the effect of two-body encounters, albeit a quite complicated one. These two equations have been linearized about a thermodynamic equilibrium, certain terms have been neglected, and then the system has been solved. Ion motions are neglected.

The Fourier-Laplace transform of the charge density of the electron plasma is expressible as the quotient of two entire functions, and reduces to the classical Landau expression as $k_D^3/n \to 0$. The asymptotic behavior of the electric field is determined by the singularities of this function.

For long wavelengths of wave number k, the damping decrement is given by $\gamma_L + \gamma_c$, where γ_L is the usual Landau damping decrement, and γ_c is given by

$$\frac{\gamma_c}{\omega_p} = 0.0106\ \frac{k^2 k_D}{n}\ ,$$

where $\omega_p^2 = 4\pi ne^2/m$, and $k_D^2 = 4\pi ne^2/KT$.

6.6 COULOMB DISSOCIATION OF DEUTERONS BY ELECTRONS

G. K. Soper

The electrodisintegration cross section for Coulomb dissociation of deuterons by electrons can be evaluated employing the formula by Guth

---

[6] T. K. Fowler, *Plasma Stability Analysis Employing Equilibrium Constants of Motion*, ORNL-3123 (1961).

[7] Y'akov Shima and R. G. Alsmiller, "Code for Studying Stability of Plasma Columns in a Magnetic Field," *Thermonuclear Div. Semiann. Progr. Rept. Apr. 30, 1962*, ORNL-3315.

[8] E. G. Harris, *J. Nucl. Energy, Pt C* 2, 138 (1961).

[9] Consultant, University of Maryland.

and Mullin:[10]

$$\sigma_e(E_i) = \int_{\epsilon}^{E_i} d(\hbar\omega)\, \sigma(\hbar\omega)\, N(E_i, \hbar\omega)\,,$$

where

ϵ = binding energy of deuteron,

$N(E_i, \hbar\omega)$ = number of photons (per unit energy interval) with energy $\hbar\omega$ by which the action of the field of the electron may be represented in producing the disintegration process,

$\sigma(\hbar\omega)$ = cross section for photodisintegration with photons of energy $\hbar\omega$.

Figure 6.6 is a plot of the electrodisintegration cross section as a function of the electron energy which is the sum of the electric and magnetic disintegration cross sections which are also included here.

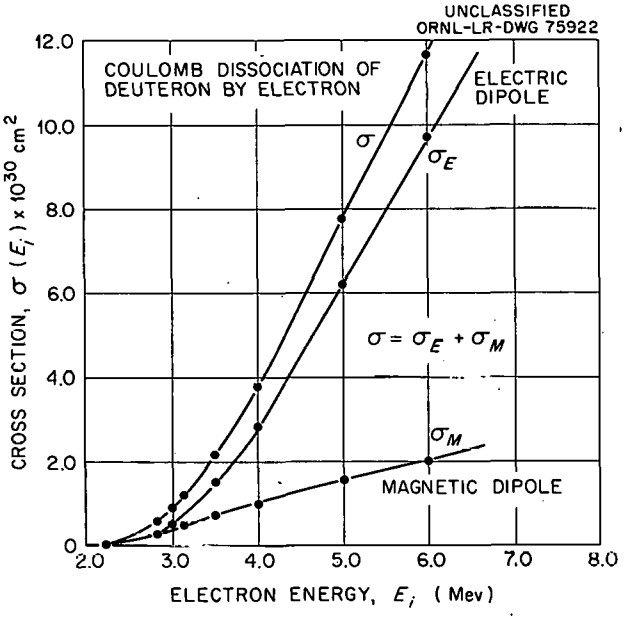

Fig. 6.6. Evaluation of Formula (38) in Guth and Mullin, *Phys. Rev.* 76, 234–43 (1949).

6.7 ORBIT CALCULATION AND PLOTTING

Mozelle Rankin D. A. Griffin

A new IBM 7090 code, MADCAP, has been written for the calculation and plotting of single-particle trajectories in electromagnetic fields. Its time, as calculated from use for orbits in Elmo, PTF, and the DCX-1 midplane, is about 40 to 50 integration steps per second; this is approximately 6 to 7 times faster than previous codes. MADCAP also permits orbit calculation between coils, thus overcoming a difficulty previously encountered in Elmo calculations.[11]

The first section of MADCAP, which is run only one time for any given coil configuration, stores all necessary magnetic-field information in a specified (r, z) mesh of points (theta symmetry is assumed). In this part of the code, B_r and B_z and the first and second partial derivatives of one component (B_r in this case) are calculated, printed, and also stored on a magnetic tape. This tape is then read into the memory at the beginning of all following orbit calculations. Whenever the magnetic field is required (three times per step in the Nystrom version of the Runge-Kutta integration procedure which the orbit calculation uses), it is obtained by Taylor's series expansion.

In Elmo and PTF, the storage mesh has been specified as $\frac{1}{2}$ in. over an area defined by $0 \leq r \leq 11.5$ in. and $0 \leq z \leq 11.5$ in. Tests show that Taylor's series expansions in this grid give the field to an accuracy of 1 part in 5000. The DCX-1 midplane field has been stored in $\frac{1}{2}$-in. steps from 0 to 80 in.

The field and its derivatives were stored by the summation of contributions from loops using elliptic integral evaluations. This method has the computational advantage that, although the equations are rather lengthy, all seven quantities to be stored are algebraic combinations of the two elliptic integrals $E(k)$ and $K(k)$. Computing time for the two field components and five derivatives has been found to be about 6 msec per loop-point, or about 45 min. for the 576 points stored for PTF. It is necessary to store only the derivatives of one field component, since the derivatives of the other component may be obtained from the Maxwell equations.

The new Cal-Comp plotter at the Mathematics Panel has been programmed from the IBM 7090 to display pertinent information from the orbit calculations. For electron trajectories in Elmo,

[10] Eugene Guth and C. J. Mullin, *Phys. Rev.* **76**, 234–43 (1949).

[11] Mozelle Rankin and R. J. Kerr, *Thermonuclear Div. Semiann. Progr. Rept. Apr. 30, 1962*, ORNL-3315, p 71.

r, z, and the adiabatic moment μ are plotted vs time as well as r vs z. In PTF orbits, a plot of energy change E/E_0 vs time is substituted for μ vs time. The DCX-1 midplane calculation code plots the midplane orbit.

We have continued to operate an expanded version of an old code, TILDA,[12] for studies of precession in DCX-2. The code additions consist of a plotting routine to give an X-Y plot, an r and z vs time plot, and an r vs z plot. The precession angle at the end of a run is also now printed. A typical case is shown in Figs. 6.7 and 6.8.

6.8 CODES FOR DCX-1 STUDIES

Mozelle Rankin D. A. Griffin
J. L. Dunlap

Two codes, one for energy-spectrum analysis and one for containment zones, have been written to facilitate studies of data taken in DCX-1. The result of the energy-spectrum analysis code is shown in Figs. 6.9 and 6.10.

In Fig. 6.9 the energy distribution of charge-exchange neutrals (measured with a silicon surface barrier detector and a 256-channel energy analyzer) is input data. The neutral-particle distribution normalized to 1 is plotted, and the inferred trapped-proton distribution is computed from the relationship:

$$\frac{n_+(E)}{n_+(E^*)} = \frac{n_0(E)}{n_0(E^*)} \frac{\sqrt{E^*}\,\sigma_{cx}(E^*)}{\sqrt{E}\,\sigma_{cx}(E)},$$

where E^* is arbitrarily fixed as the energy at which the neutral distribution is a maximum. The proton curve is then normalized to 1 and plotted. Average energies and the areas under each curve (which are proportional to the densities) are printed.

In Fig. 6.10 are plotted the time decay curves of the trapped-proton density and of the charge-exchange signal to foil-covered neutral-particle detectors, where

$$N_+(t) = \frac{\sum_i n_+(E_i) \cdot e^{-k\sigma_{cx}(E_i)\sqrt{E_i}\,t}}{\sum_i n_+(E_i)}$$

and

$$\mathrm{NPD}(t) = \frac{\sum_i n_+(E_i) T(E_i) \sigma_{cx}(E_i) \sqrt{E_i} \cdot e^{-k\sigma_{cx}(E_i)\sqrt{E_i}\,t}}{\sum_i n_+(E_i) T(E_i) \sigma_{cx}(E_i) \sqrt{E_i}}.$$

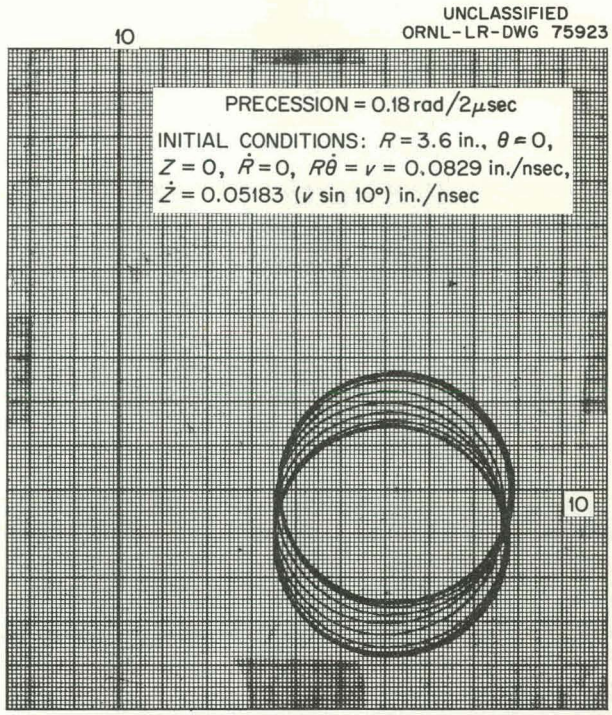

Fig. 6.7. X-Y Plot of 300-kev H^+ in DCX-2.

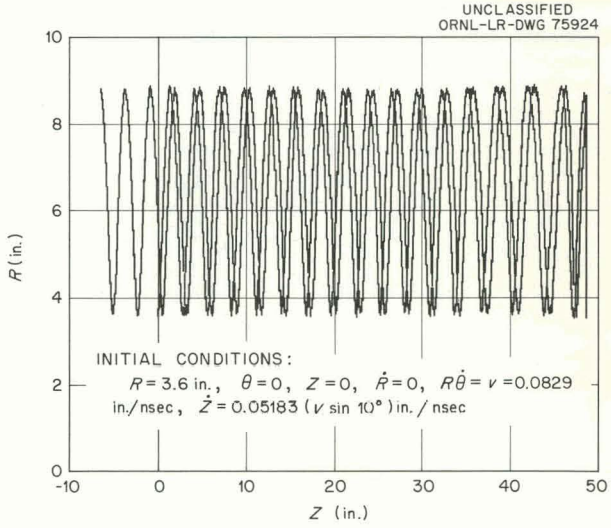

Fig. 6.8. R-Z Plot of 300-kev H^+ in DCX-2.

[12] G. R. North and C. E. Parker, *Thermonuclear Div. Progr. Rept. Oct. 31, 1961*, ORNL-3239, p 77.

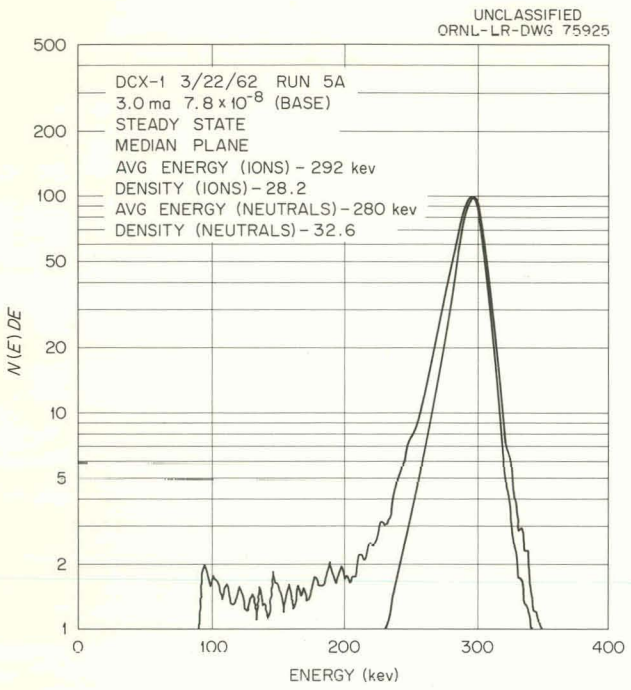

Fig. 6.9. Energy Distributions of Charge-Exchange Neutrals and Trapped Protons.

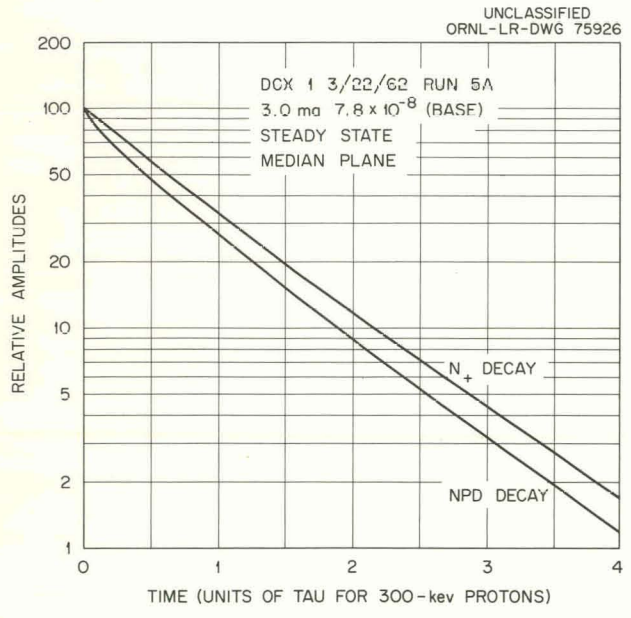

Fig. 6.10. Time Decay Curves of Trapped-Proton Density and of Charge-Exchange Signal to Neutral-Particle Detectors.

The summation extends over all energy channels; $k \equiv 1/[\sigma_{cx}(300)\sqrt{300}]$, and $T(E)$ is the transmission factor for the foil covering the neutral-particle detectors.

The containment-zone code calculates and plots containment zones directly from the input of coil configurations and currents for any mirror field. Searching for the $|(P_\theta/r) - a| = 1$ boundaries, formerly a time-consuming intermediate step performed off-machine, is now done efficiently by the code.

6.9 DCX-2 PERFORMANCE CURVES

Mozelle Rankin T. K. Fowler

The survey of expected DCX-2 performance as a function of machine parameters has been continued. As previously reported, in computing the "*S*-curve" relation between molecular-ion injection current and the trapped-ion density achieved, charge-exchange and ionization cross sections are properly averaged over ion and electron energy distributions determined from numerical solution of Fokker-Planck equations.[13,14] Figure 6.11

[13] T. K. Fowler and Mozelle Rankin, *Thermonuclear Div. Semiann. Progr. Rept. Apr. 30, 1962*, ORNL-3315, p 66.

[14] T. K. Fowler and Mozelle Rankin, *J. Nucl. Energy, Pt C* **4**, 311–20 (1962).

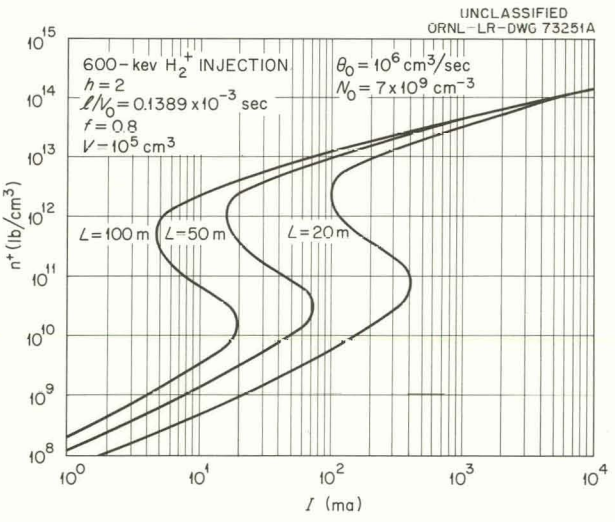

Fig. 6.11. DCX-2 Performance Curve. Trapped-ion density vs injected molecular-ion current (path length as a parameter).

gives performance curves for E_M = 600 kv (molecular-ion energy) and several values of the molecular-ion path length in the machine, L. In Fig. 6.12, L = 50 m and E_M is varied. For these results, only binary collisions are taken into account in computing energy transfer rates (E.T.R.) in the Fokker-Planck coefficients. To see the effect of enhancement of these rates by collective phenomena, in Fig. 6.13 performance curves are presented with E.T.R. multiplied by arbitrary factors. Having in mind mechanisms primarily involving ion-electron interaction, such as the Harris instability, we have enhanced only the ion-electron transfer rate and the electron scattering loss rate.

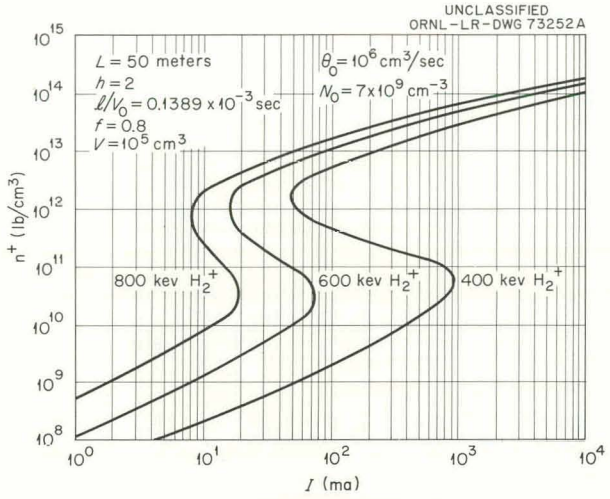

Fig. 6.12. DCX-2 Performance Curve. Trapped-ion density vs injected molecular-ion current (molecular-ion energy as a parameter).

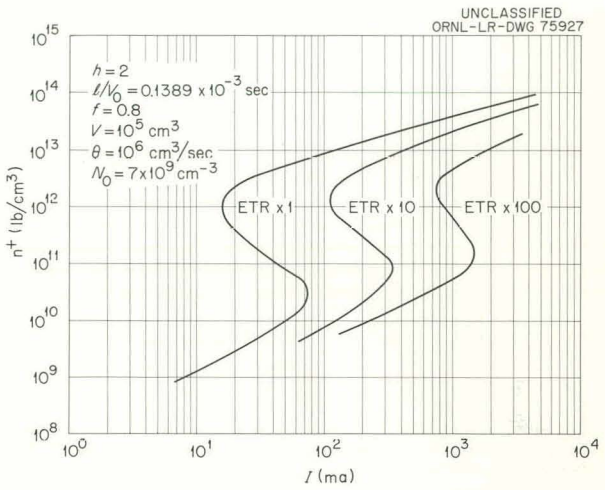

Fig. 6.13. Trapped-Ion Density vs Injected 600-kev H_2^+ Ion Current for 50-m Path Length (Energy Transfer Rate as a Parameter).

7. Magnetics and Superconductivity

7.1 NEW COMPUTER PROGRAMS FOR CALCULATING MAGNETIC PROPERTIES OF CURRENT SYSTEMS

C. E. Parker

In report ORNL-3318, *Computer Program Using Zonal Harmonics for Magnetic Properties of Current Systems with Special Reference to the IBM 7090*, Garrett[1] gives a detailed description of his new computer program. This extended work was undertaken on request from and in close cooperation with the Engineering Science Group, who previously employed zonal harmonic methods for several special problems.[2]

The application of this computer program is limited to source-free regions (inside convergence spheres); for special cases another code is desirable which is not restricted in this respect. A computer program of the latter kind based on Gaussian integration of elliptic integrals is near completion, and a report will be published. For many applications, however, the former code is preferable because of its superior speed and other advantages.

The abstract of Garrett's computer code based on zonal harmonics is as follows:

"This report discusses the magnetic vector and scalar potentials, magnetic field components and their derivatives, and flux linkage for single current systems, and the mutual inductance, forces and torques between two such systems, whose axes are coplanar but not necessarily coincident. Each system may include a combination of coaxial loops, cylindrical or plane annular current sheets, and cylindrical coils of rectangular section.

"Working equations are listed, following an outline of theory in a form that has considerable generality but is at the same time ideally suited to precise calculation. A discussion of errors and of means for reducing them leads to specific suggestions for use of the method with any programmed computer. An existing comprehensive program for the IBM 7090 is described in detail.

"The rate of convergence of the harmonic series depends on the ratio R of the polar radius of the field point to that of the current discontinuity nearest the origin. In some cases the precision reaches 1000 parts per million even at $R = 0.95$, improving to 1 or 2 parts at $R = 0.80$. Since the origin is arbitrary, the practical range of the method often includes the whole space that is accessible to experiment. For very close approach to the windings one must resort to elliptic integral methods or their equivalent.

"Alternative programs that have been used are compared with the method of zonal harmonics, but they are slower by more than a factor of 10 when large numbers of field calculations must be made on a complex current system. One example is the problem of following individual ions through paths in the order of 100 turns in a field that is generated by 20 coaxial thick coils; available competing methods would have required too much computer time. The zonal harmonic method also has superior flexibility in attacking a wide range of problems. This is especially true for the calculation of rates of change, with respect to coordinates of the field or of the generating system, and for problems in which some property of

[1]Consultant, Swarthmore College.

[2]Mozelle Rankin and W. F. Gauster, *Thermonuclear Project Semiann. Progr. Rept. July 31, 1959*, ORNL-2802, pp 105–7; W. F. Gauster and M. W. Garrett, *Thermonuclear Project Semiann. Progr. Rept. July 31, 1959*, ORNL-2802, pp 133–35; W. F. Gauster, *Thermonuclear Project Semiann. Progr. Rept. Jan. 31, 1960*, ORNL-2926, pp 80–81 and 84–91; W. F. Gauster, Harold Mott, and C. E. Parker, *Thermonuclear Project Semiann. Progr. Rept. July 31, 1960*, ORNL-3011, pp 85–92.

a system must be not only calculated, but also adjusted to meet a specification."

7.2 MAGNET-COIL TECHNOLOGY

7.2.1 High-Field Magnet

R. L. Brown

The increasing demands for high-field magnets prompted the construction of one to produce a field of 100 kilogauss or more. Such magnets can be employed for experiments in plasma physics and superconductivity and are of interest for studying the possibilities of improving magnet design and reliability in general. High-field magnets have been made using Bitter-type[3] construction, which is very efficient from the standpoint of power consumption. However, there are some associated problems with that type of magnet, such as reliable insulation and maintaining good quality of coolant, which justify a look at more conventional methods of construction.

Based on Luton's design of magnet coils,[4] pancake coils were made of 12 short conductors wound in concentric spirals. The water paths are in parallel, and the conductors are connected in series electrically (Fig. 7.1). The conductors spiral inward to the center, are offset to another plane, then spiral outward, always winding in the same direction. Fast, simultaneous winding of pancakes was accomplished by stretching all conductors from one large wagon wheel (see Fig. 7.2) to the opposite side of another wagon wheel. An offset in each conductor at the center spool is necessary in order to change from the front plane to the rear plane of the pancake coil. After the offsets or "crossovers" are made, the wagon wheels are rotated in opposite directions to complete the winding operation. Silver-solder connections between the electric circuits are made after the pancake has been clamped and removed from the wheels. An insulating coat of Teflon and acrylic enamel (4 mils thick) is applied to each conductor before winding. Mylar segments are preformed for the center offset and placed between the two planes of the pancakes. Figure 7.3 shows a single conductor with its insulation and the ultimate shape which the conductor will have when wound into a pancake. Each conductor makes $2\frac{1}{12}$ turns. At each electrical connection there are two water connections; these pairs are alternate inlet and outlet terminals for the coolant water.

Six pancakes were made while perfecting winding and insulating techniques. These were potted in epoxy (Shell 828, curing agent "Z," with aluminum oxide filler), selected because of its strength and because its coefficient of expansion is about the same as that of copper (Fig. 7.4). The coil failed under test because of what appeared to be a faulty silver-solder joint. Furthermore, poor epoxy impregnation allowed water to leak from several water headers through the coil to the bore. These problems probably could have been solved, but it was decided to construct another coil without epoxy. Four new pancakes were wound and were successfully tested with 50 kilogauss, using a water-supply system (shown in Fig. 7.5). The inset to Fig. 7.5 shows the basic parts of the water header. Tests proved the reliability of this system. Its special advantage is that the coil is very accessible if repairs become necessary. Shoes are machined to fit at 12 places around the periphery of each pancake. These shoes are hand-fitted to be snug so that they will contain the radial magnetic forces.

A magnet has been constructed. It consists of 11 pancakes stacked $4\frac{1}{2}$ in. high. A mild-steel yoke reduces somewhat the power required for a given field and also diminishes the stray field around the coil. This magnet (Fig. 7.6) has been tested with currents up to 4300 amp, corresponding to 104 kilogauss. Tests will be continued with full rated currents of 5000 amp as soon as necessary generator changes can be made.

The essential data of the magnet coil are shown in Table 7.1.

7.2.2 80-kilogauss Magnet Facility

J. N. Luton, Jr.

The design and the purpose of an 80-kilogauss magnet were described in a previous report.[5] The first of the two coils was fabricated, installed,

---

[3] F. Bitter, "The Design of Power Electromagnets – Part II," *Rev. Sci. Instr.* **7**, 482–89 (1936).

[4] *Thermonuclear Project Semiann. Progr. Rept. July 31, 1960*, ORNL-3011, sec 2.4.

[5] *Thermonuclear Div. Semiann. Progr. Rept. Apr. 30, 1962*, ORNL-3315, p 74.

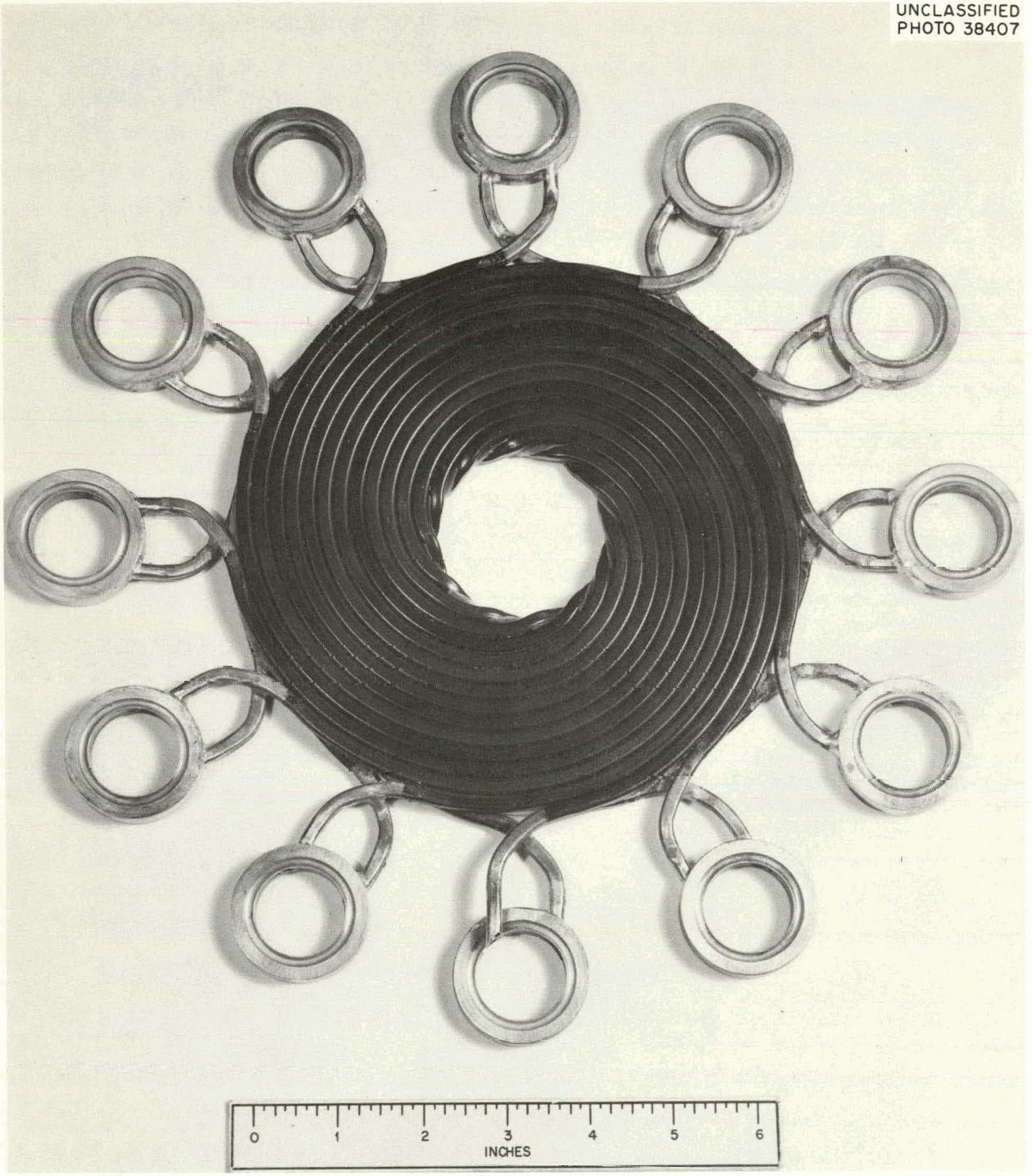

Fig. 7.1. Single Pancake Coil.

UNCLASSIFIED
PHOTO 59667

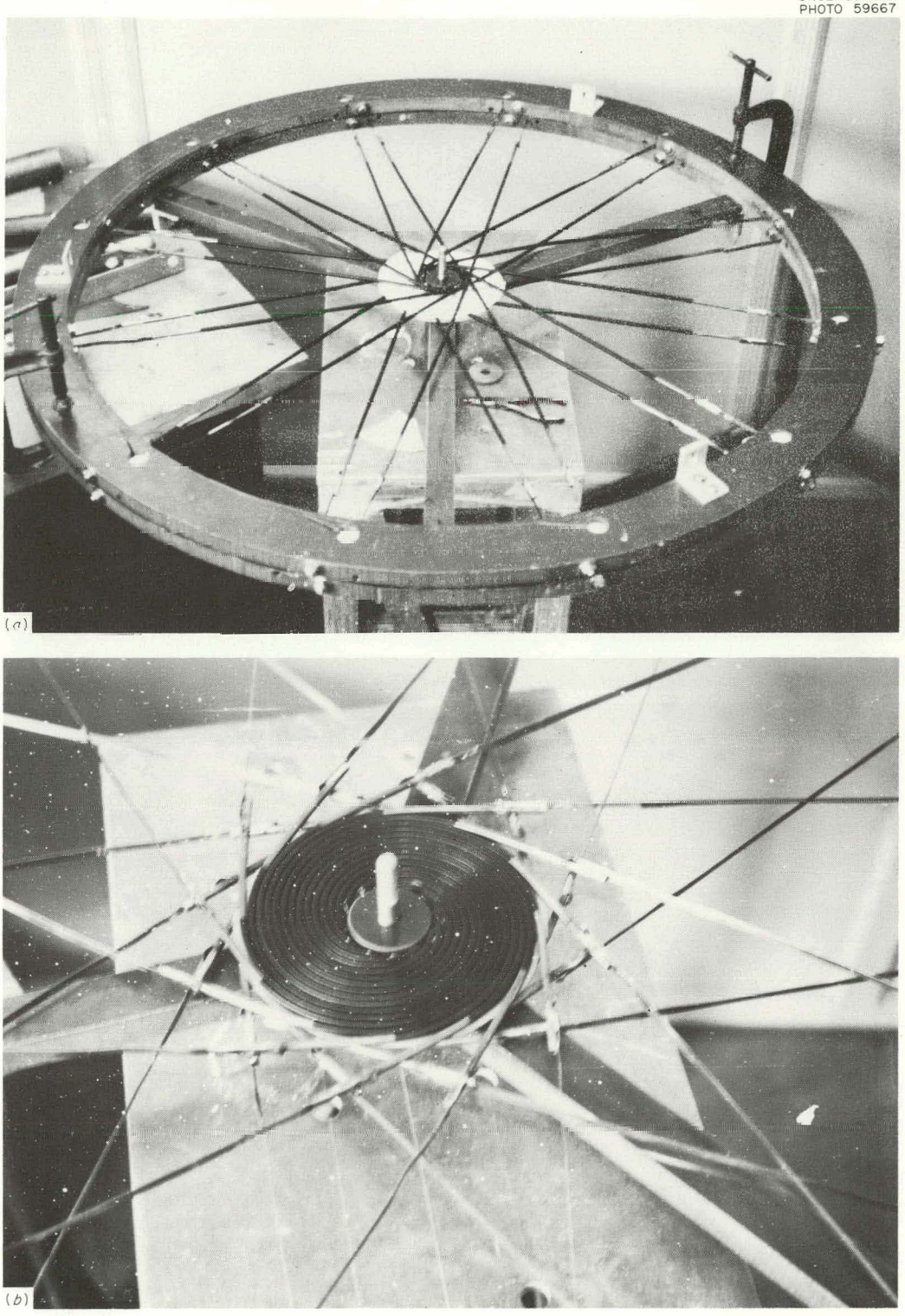

Fig. 7.2. **Pancake Winding Wheels.** Pancake shown partially wound.

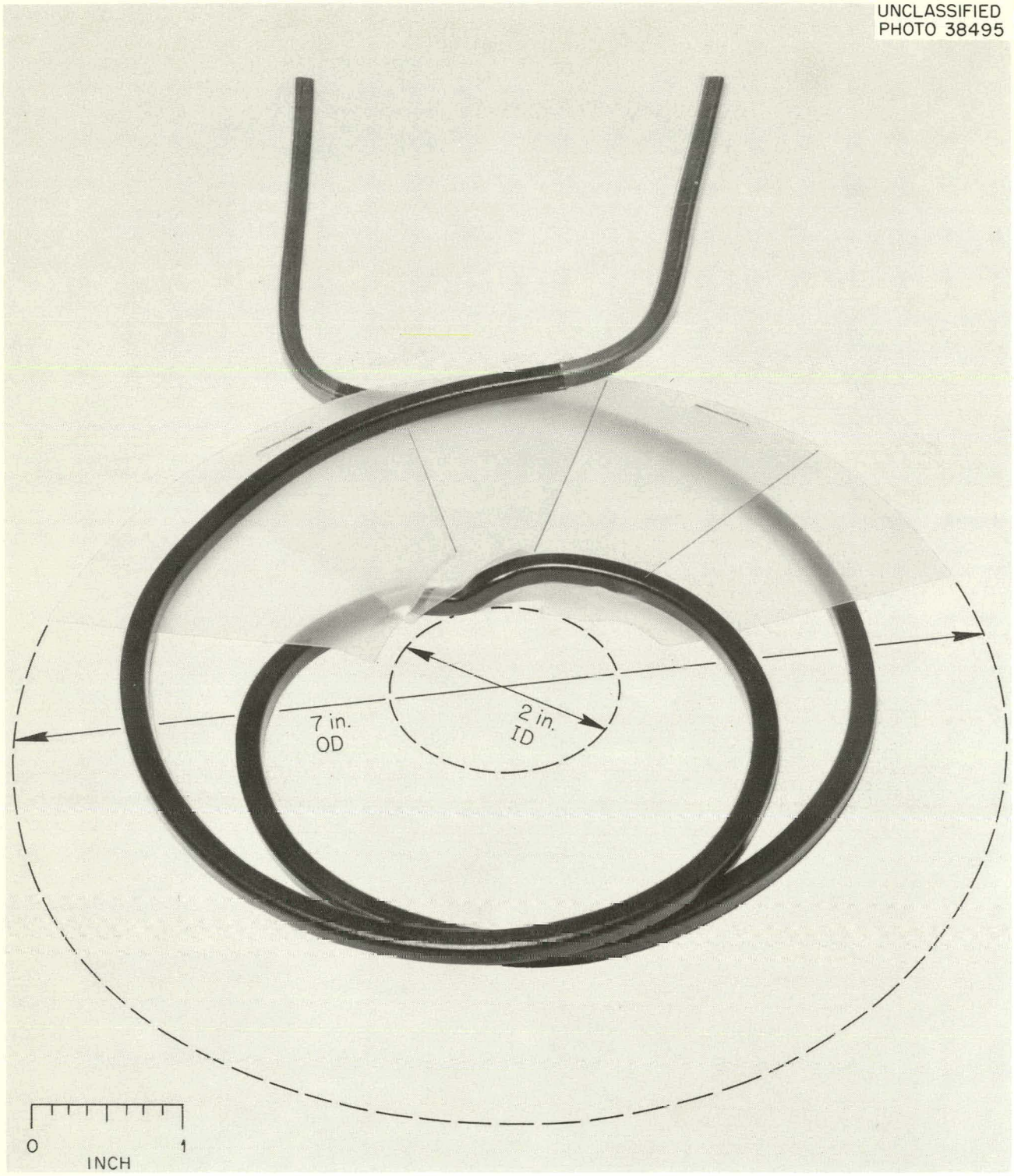

Fig. 7.3. Single Conductor and Insulation.

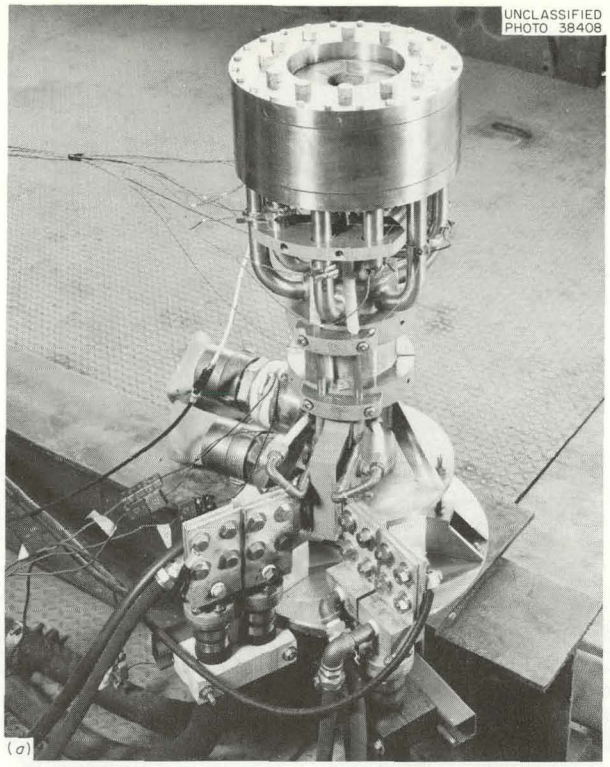

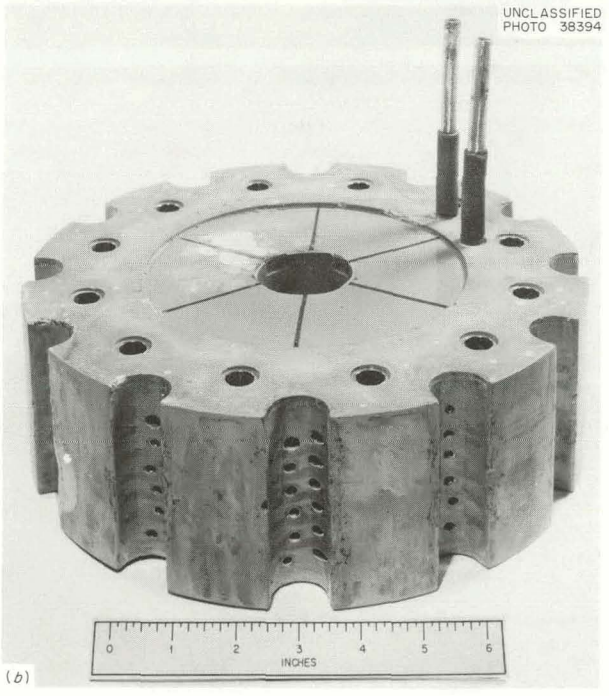

Fig. 7.4. Six-Pancake-Coil, Epoxy-Impregnated Magnet.

Table 7.1. Magnet Specifications

B = 118 kilogauss
I = 5000 amp
V = 900 v
P = 4.5 Mw
R = 0.18 ohms
N = 275 turns
G = 0.177 Fabry factor
a_1 = 1 in., inside radius
a_2 = 3.5 in., outside radius
$2b$ = 4.6 in., length
S = 3/16 in., conductor size (square)
d = 1/8 in., conductor coolant hole (circular)
Δp = 200 psi, water pressure drop
Q = 275 gpm, water flow
ΔT = 55°C, water temperature rise

successfully tested, and operated at its rated field of 62 kilogauss. It showed no indication of shorts or other malfunction and will be placed in routine operation as soon as the current regulation is improved. It is shown in Fig. 7.7, with the top of the shielding box removed to make the coil visible. The outer diameter of the coil is 2 ft, and the height is 11 in. The lower coil, now under construction, has the same height as the temporary pipe stanchion and will be inserted below the existing coil.

Figure 7.8 gives some coil parameters and shows the calculated axial and midplane field distributions for one coil and for the two-coil assembly with a 0.6-in. gap. The field strength of 62 kilogauss produced by one coil can be increased to 80 kilogauss by using a pair of coils. For some experiments this increase might not be so important as the improvement of the field homogeneity (as shown in Fig. 7.8). Even at field strengths below 62 kilogauss, the two-coil set must be used when high-field homogeneity is required.

(a)

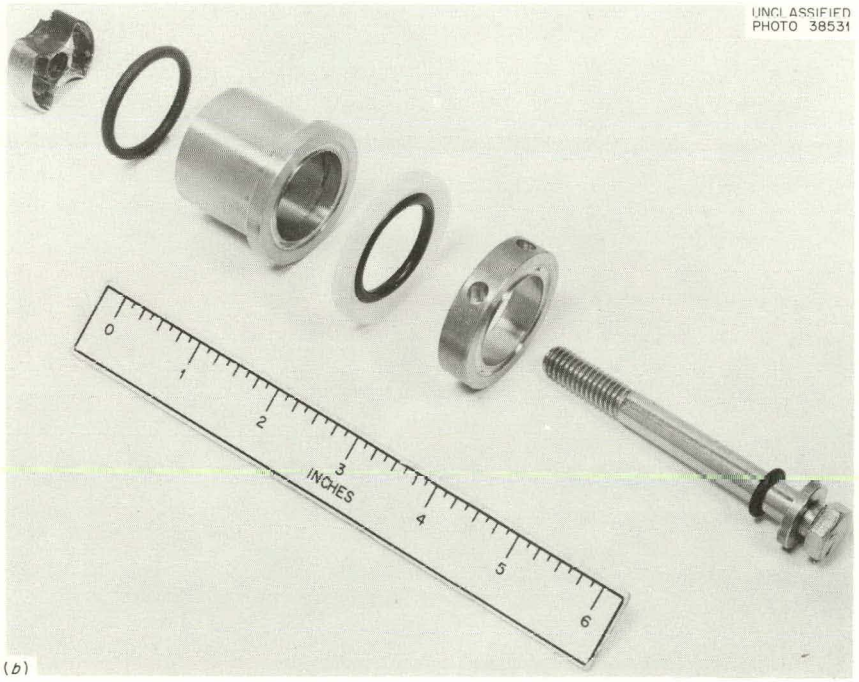

(b)

Fig. 7.5. Four-Pancake Magnet.

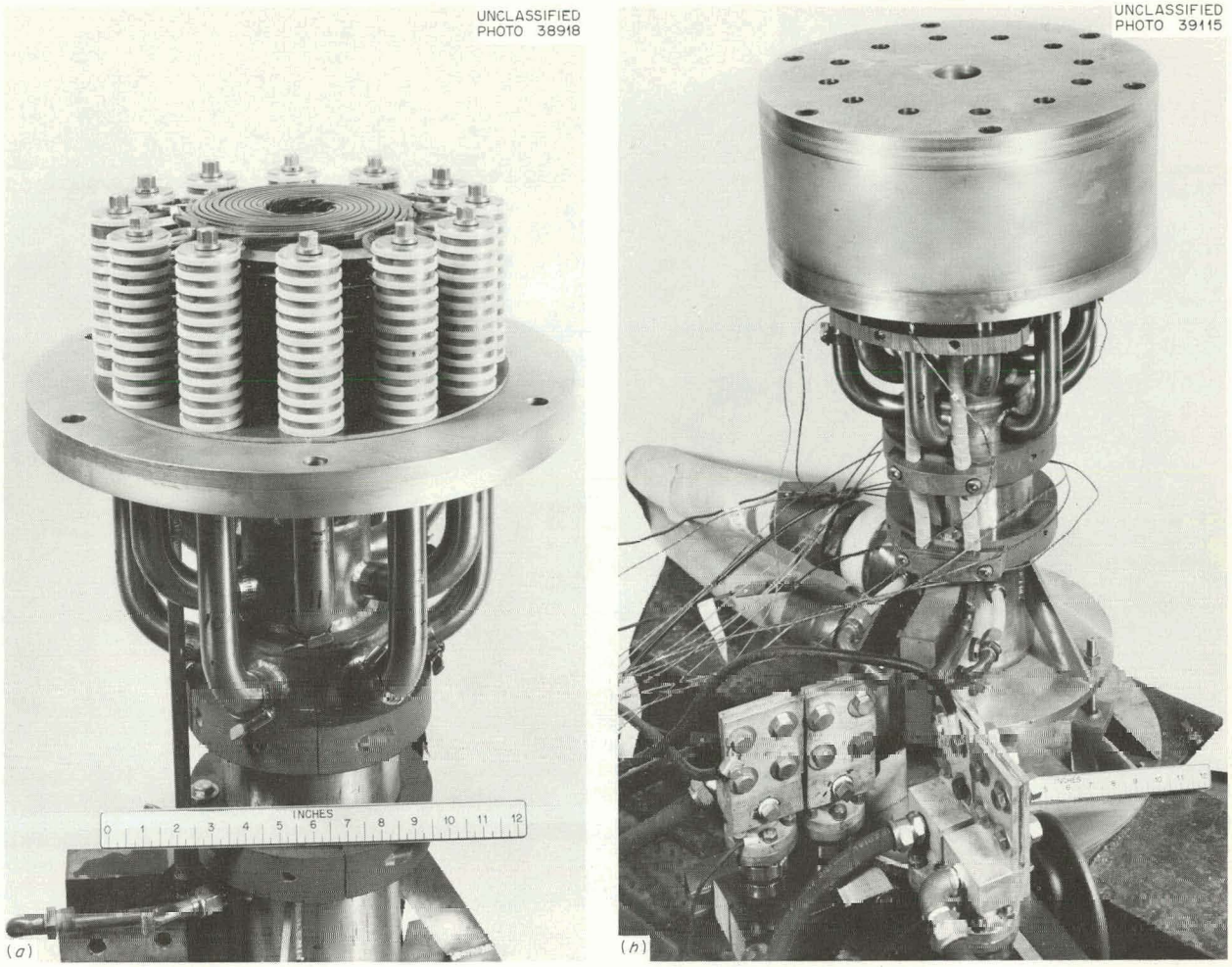

Fig. 7.6. Eleven-Pancake Magnet with Soft Iron Yoke Partly Removed.

7.2.3 Flexible-Cable Solenoid

J. N. Luton, Jr.

The preceding semiannual progress report contained a description[6] of a water-cooled dc solenoid to be built from flexible cable rather than from the more usual rigid tubular conductors. A bare, stranded welding cable, serving as the current conductor, was to be fished into a thin-walled water hose, thus insulating the cable and at the same time providing an annular water passage.

This "cable coil" has subsequently been constructed. Some difficulties were encountered in the fabrication of joints in the conductor assembly, and water-flow tests on the completed coil indicated that the joints were appreciably restricting the water flow and that the coil would therefore overheat. As a result, the coil was rewound to provide a larger number of parallel water paths. In spite of this extensive rewinding, the actual cost of the coil was still considerably less than the estimated cost of providing a pancake coil to produce the same field.

After construction, the coil was installed in its operating position at the neutral-beam experiment, as shown in Fig. 7.9, connected to the 3.5-Mw rectifier power supply, and subjected to

[6] *Thermonuclear Div. Semiann. Progr. Rept. Apr. 30, 1962*, ORNL-3315, p 74.

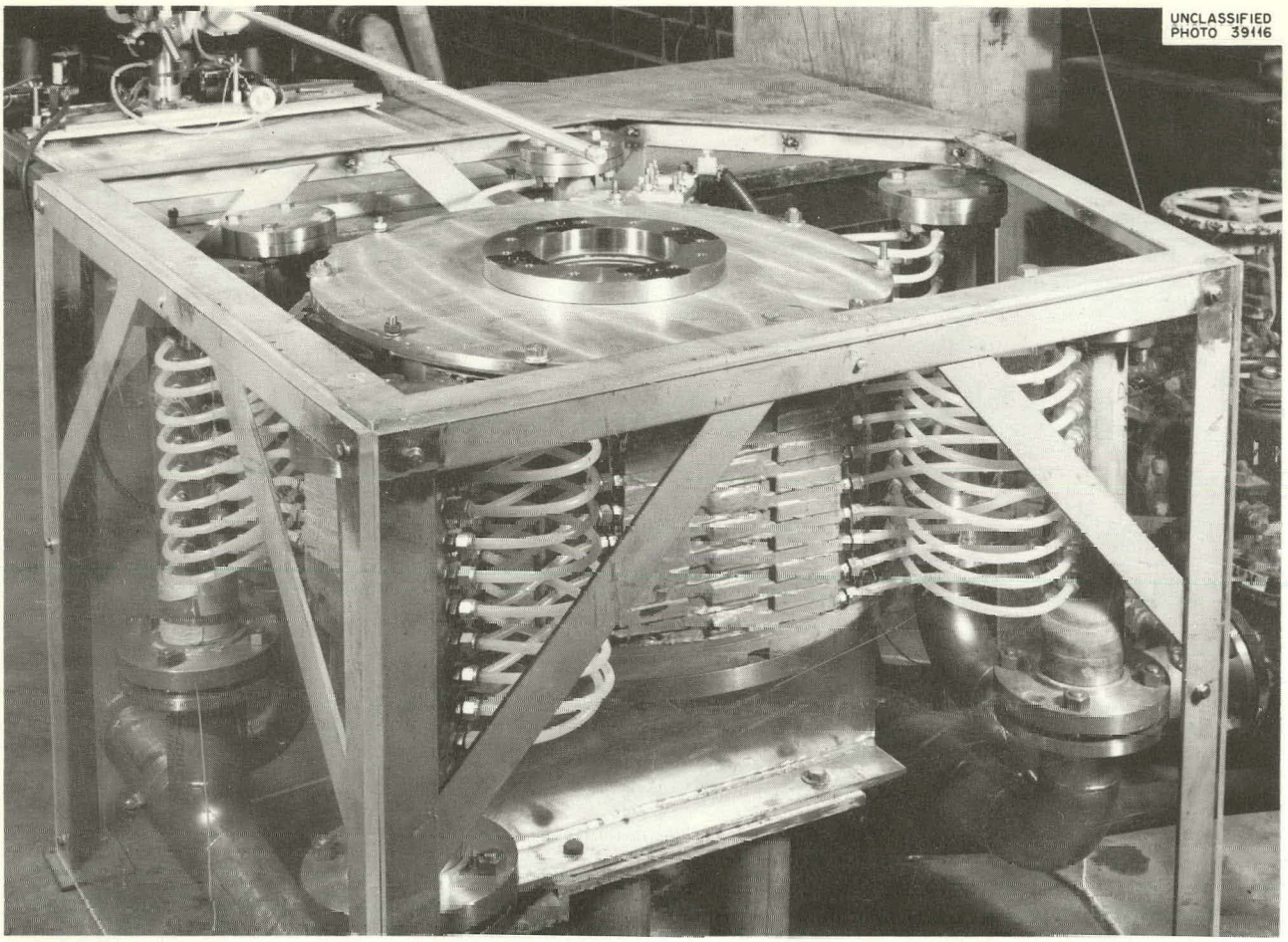

Fig. 7.7. First Coil of 80-Kilogauss Assembly.

acceptance tests. The coil current was raised stepwise to a value slightly above the coil design current of 7000 amp (which is also the rating of the rectifier) and was then rapidly cycled several times between no-load and full-load current. Water pressure and flow, conductor movement, coil current and voltage, and temperatures of water paths and structural members were monitored.

The coil itself performed satisfactorily in all respects, but due to the relatively low inductance of the coil and the absence of a filter on the rectifier, a large ripple in the coil current resulted. This produced both an excessive noise level and eddy-current heating in nearby structural members. The 10-in. stainless steel pipe on which the coil was wound reached a temperature of 150°C in about 15 min and was rapidly becoming hotter when the coil was shut down. An inductance and a capacitance are being added to the circuit in order to filter out the current ripple.

A calculation (based on the thickness of the pipe on which the coil is wound, the resistivity of stainless steel, and the predominant frequency of the ripple) indicates that the alternating field penetrates the pipe wall with about two-thirds its original strength. This fact introduces the possibility of using the coil, when the proposed filter is switched off, as an induction heater for bake-out of the included vacuum system. This might even provide selective heating of the components: parts to be heated would be made of a good conductor and would encircle as much flux as possible, whereas parts which should not be heated would be made of an insulating material or of a metal shaped so as to link little flux.

UNCLASSIFIED
ORNL-LR-DWG 73662A

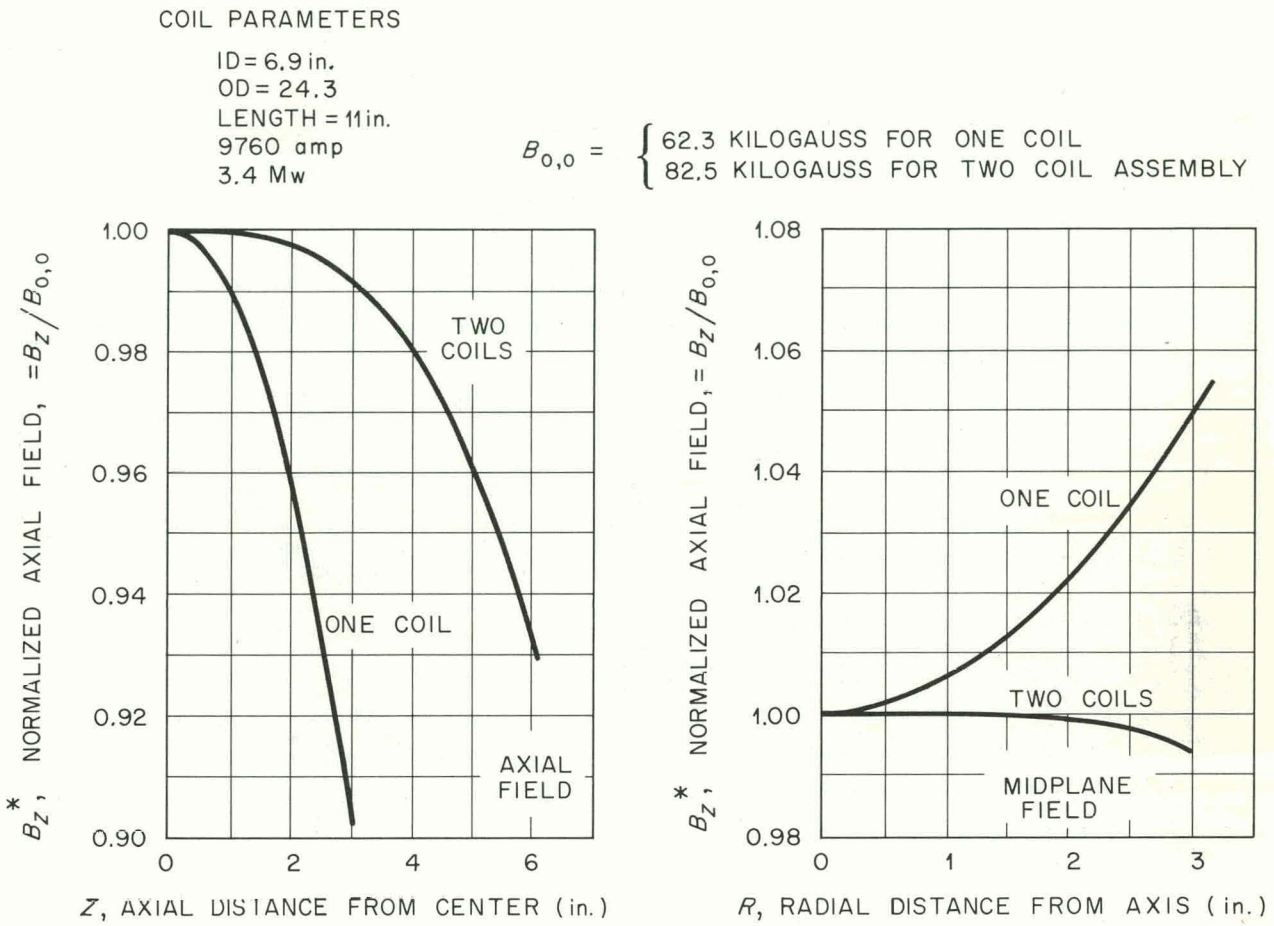

Fig. 7.8. 80-Kilogauss Magnet Facility.

7.3 CRYOGENIC TECHNOLOGY

7.3.1 Test Cells for Superconductivity Experiments

D. L. Coffey W. F. Gauster D. C. Hopkins[7]

Two important tests of samples of superconducting materials involve measurements of (1) the resistance and (2) the magnetic moment. Both tests require an apparatus that can hold the sample at a controllable, steady temperature.

With soft superconductors (Sn, Pb, Hg, In, etc.) the necessary temperature range can be achieved by pumping the liquid-helium bath surrounding the sample. High-field superconductors, with their higher critical temperatures [Nb_3Sn, 18.1°K; Nb(25% Zr), 11°K], demand a much larger temperature range for complete study. Liquid helium can be employed up to 5°K; liquid hydrogen can be used down to 14°K; but the range between requires a cryostat of special design. Many different designs, already known from other low-temperature investigations, give some insight into the type of apparatus required. To hold the proper temperature in the presence of ohmic heating produced in the intermediate state transition of the superconductor, a large heat capacity is to be desired.

Prototype Test Cell Design. – The test cell of Fig. 7.10 (*a* and *b*) has been developed and tested. The cell is suspended in cold helium gas just

[7]Summer employee, University of Illinois.

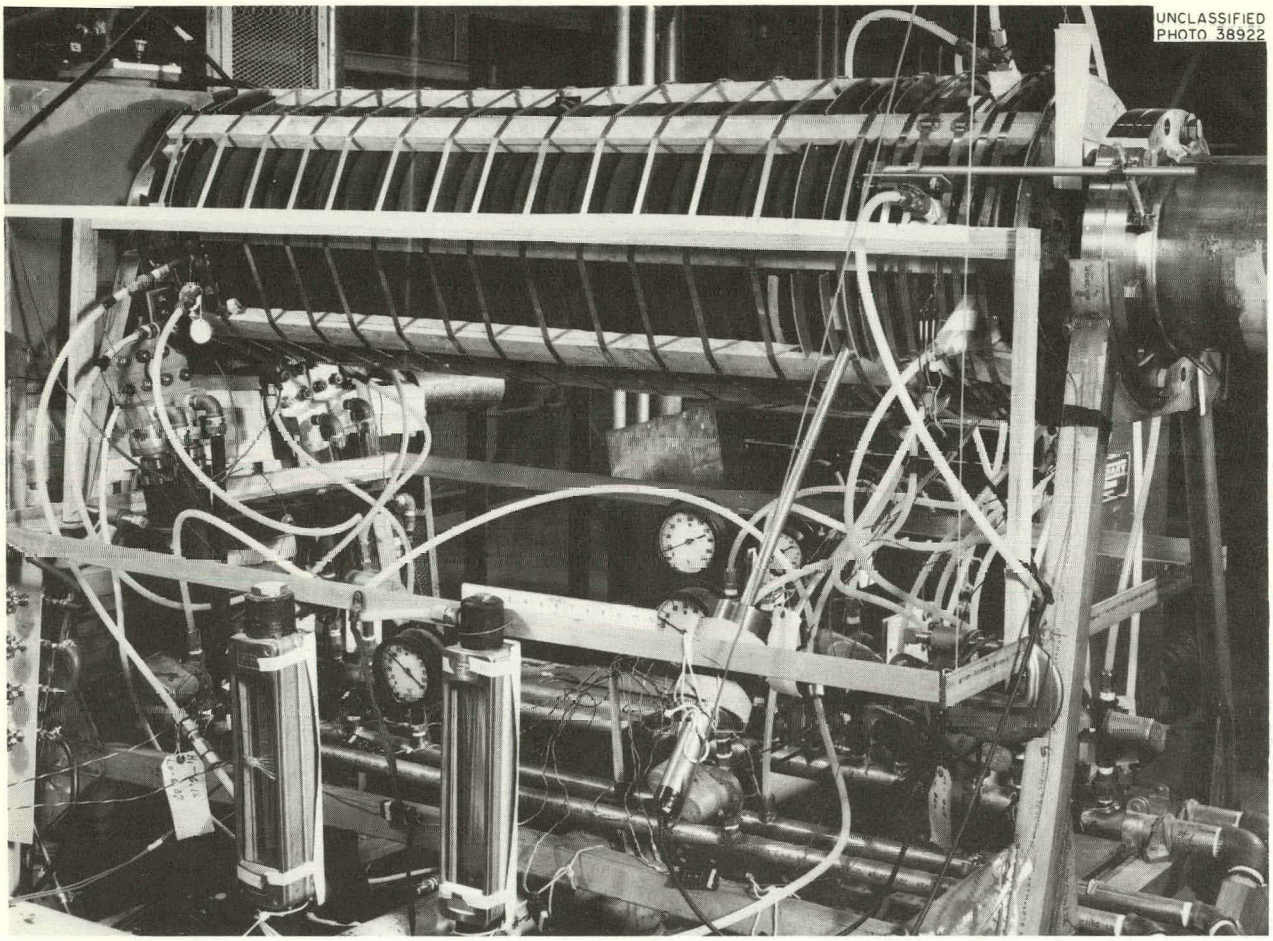

Fig. 7.9. Cable Coil for Neutral-Beam Experiment.

above the liquid-helium surface. It is constructed of heavy copper to provide an isothermal experimental volume and has copper fins on the cylinder to maintain adequate thermal contact between the cell and the helium gas.

The arrangement is designed to use efficiently the cold helium gas produced by evaporation of liquid helium because of the normal Dewar vessel heat leak. Similar arrangements have been used elsewhere.[8]

The chamber temperature is controlled by adjusting the height of the cell above the helium surface and by regulating the rate of pumping over the helium. Further control could be achieved by using a small electrical heater on the cell.

Tests of the Prototype. – In preliminary tests the temperature was measured with a gas thermometer. Assuming the ideal-gas law, the normal boiling points of nitrogen and of helium were used as reference temperatures. Pressures at low temperatures were read on Wallace and Tiernan gages, calibrated against a mercury manometer. It was necessary to consider in the usual way the dead volume of the gages.

Small temperature changes were observed by using a $\frac{1}{2}$-w carbon resistor thermometer. A second carbon resistor placed adjacent to the first was used to supply power, simulating dissipation of energy in the intermediate state of the superconductor or energy dissipated in the electrical leads.

It was possible to maintain the temperature of the test cell to within $\pm 0.007^{\circ}$K at about 10°K.

[8] D. E. Mapother and F. A. Otter, *Phys. Rev.* **125**(4), 1171–76 (1962).

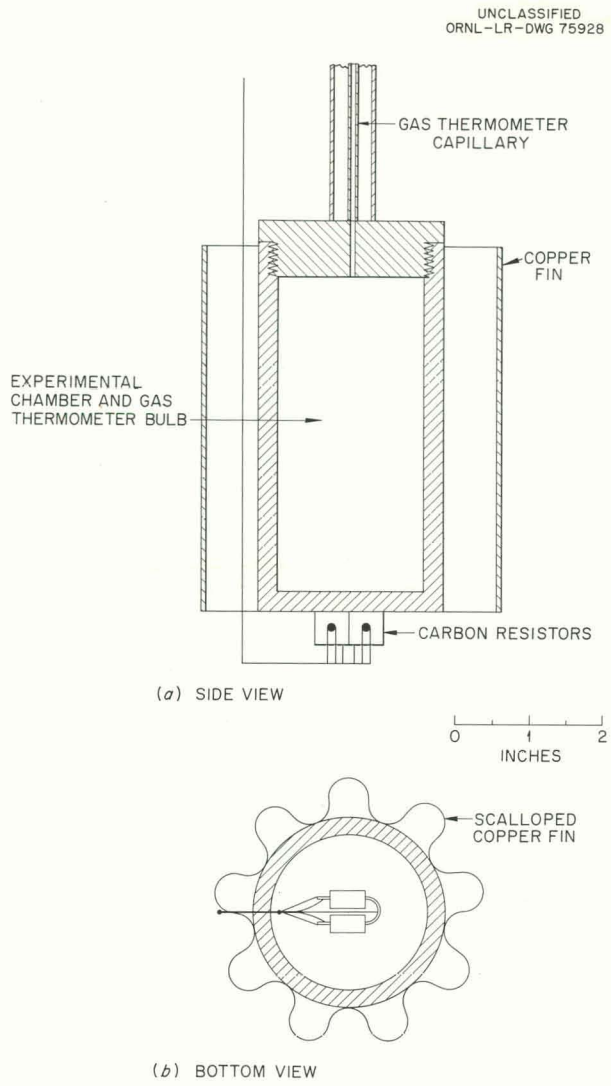

Fig. 7.10. Prototype Test Cell for Superconductors.

During this test the power input was 0.44 w. The cell was suspended about 3 in. above the helium surface. During this 26-min test the temperature of the bath was lowered from 4.18 to 3.43°K by the necessary pumping.

In a second test, power as high as 1.26 w was applied without changing the ability to control the temperature. Even more power could have been handled, but the 0.040-in. wires could not take higher currents.

An important property of this test cell design is a relatively very low helium evaporation rate.

Two New Test Cell Designs. – The experience gained with the prototype led to the development of two more advanced designs for actual experimental use. The first (Fig. 7.11*a*) will be used to measure magnetic moments as a function of temperature and magnetic field. The second (Fig. 7.11*b*) will be employed to measure resistance as a function of temperature, current, and magnetic field. Temperature measurements on each cell will be made by thermocouples, a carbon resistor thermometer, and a gas thermometer. A removable bottom plate, with a cryogenic O-ring seal, provides easier access into these new chamber designs.

The first chamber (Fig. 7.11*a*) contains two adjacent identical copper coils, connected in electrical opposition. The difference signal from these coils, produced when the sample is withdrawn from the first coil, indicates the relative permeability of the superconducting sample. In the normal state no signal will be observed. A thermal contact below the first coil maintains the sample at chamber temperature. A carbon resistor thermometer (not shown) will monitor the sample temperature.

The second chamber (Fig. 7.11*b*) contains two semicylindrical shells in intimate contact with the chamber walls. These shells are designed to carry large currents, in certain experiments, without significantly increasing in temperature above that of the chamber. Electrical insulation and thermal contact is ensured by greased mica sheets (0.001 in. thick) interposed between the semicylindrical shells and the chamber walls. Two springs maintain a pressure against the wall. Electrical connection to the sample is made by indium-tinned copper clamp joints. The temperature of each joint will be monitored by a carbon resistor thermometer (not shown). Indium-soldered voltage taps will be used to measure the sample voltage. Figure 7.12 shows an inside view of this test cell.

Experimental results will be reviewed in the next semiannual progress report.

7.3.2 Cryogenic Current Input Apparatus

R. L. Brown D. L. Coffey W. F. Gauster

Superconductivity experiments sometimes require currents up to several hundred amperes. Some provision must be made to transport these currents from room temperature (~290°K) to the experimental temperature (e.g., 4.2°K). Several attempts

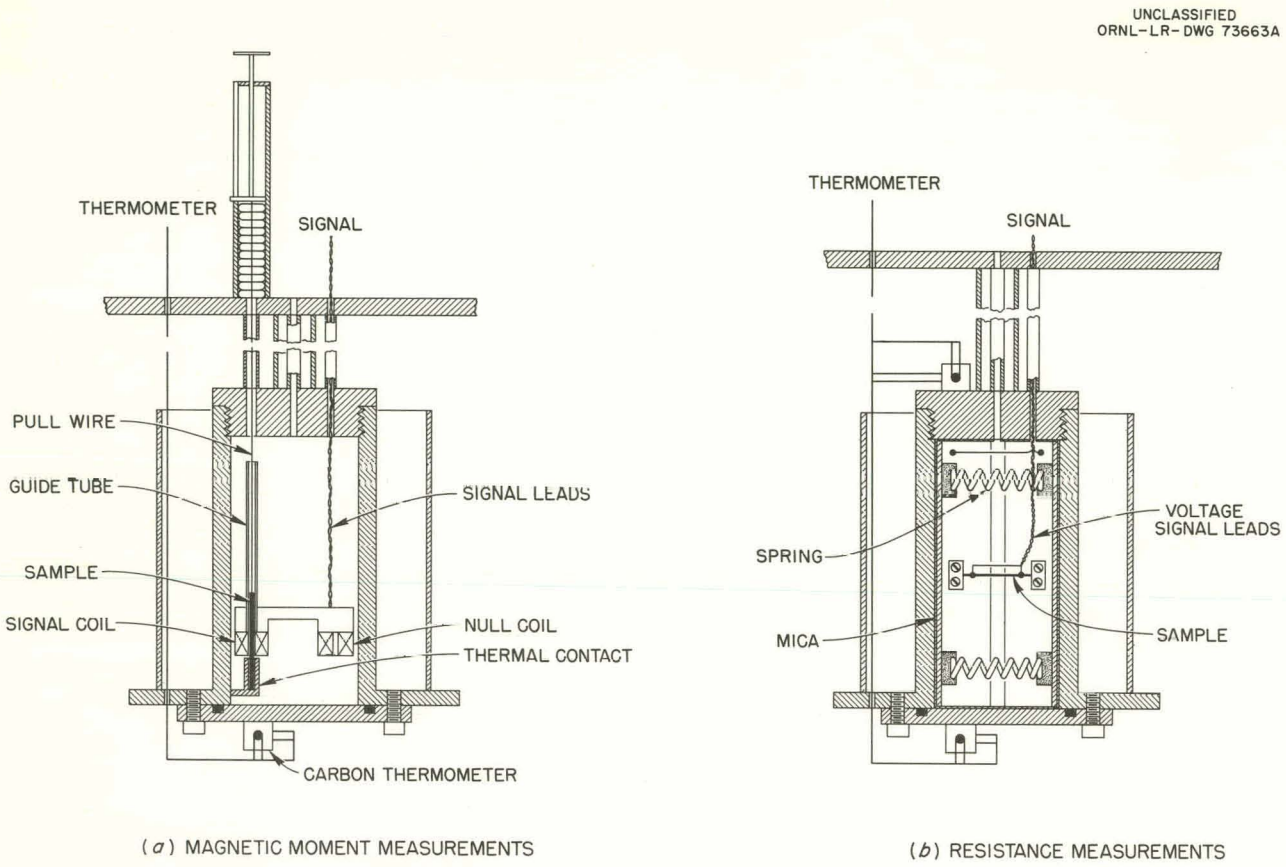

Fig. 7.11. Two New Test Cells for 1.5 to 20°K.

have been made to find current input designs which minimize the evaporation of liquid helium.[9,10] The principle employed is to precool the current leads with liquid nitrogen and to provide a large conductor surface in order to use the cold helium vapor efficiently as it rises from the surface of the helium bath.

The following special design was developed and has been tested in our laboratory:

Description of the Current Input Apparatus. Precooling to 77°K is achieved by means of six nitrogen Dewars symmetrically arranged about the top of the helium Dewar (Fig. 7.13). This design avoids current bushings through the bottom of a liquid-nitrogen container. Experience has shown that it is difficult to make reliable bushings of that type when using relatively large conductor cross sections. A nitrogen-filled copper center tube supplements the outer Dewars and maintains nitrogen temperatures inside the upper part of the apparatus. This upper section is heat-insulated by $\frac{3}{4}$-in.-thick foam rubber. The six input conductors are insulated with $\frac{1}{2}$-in. foam rubber tubing. The enlarged surface exposed to the cold helium vapor is achieved by extending each No. 6 copper conductor with 204 No. 34 copper leads.

Evaporation Tests. – With each of two of the six current input positions to carry alternately 0, 100, and 200 amp, a corresponding total current input of 0, 600, and 1200 amp was simulated. In order to simplify the performance of the test, the following repetitive current cycle was employed: 0 amp (15 min), 100 amp (10 min), and 200 amp (5 min). The elevation of the liquid-helium level h was measured by a cathetometer. Figure 7.14 ("composite curve") shows the correlation of helium level and time over about 9 cycles.

The composite curve was evaluated as follows: Each phase of a cycle yields the evaporation rate

[9]Richard McFee, *Rev. Sci. Instr.* **30**(2), 98–102 (1959).

[10]Harold Sobol and J. McNichol, *Rev. Sci. Instr.* **33**(4), 473–77 (1962).

Fig. 7.12. Inside View of Test Cell for Resistance Measurements.

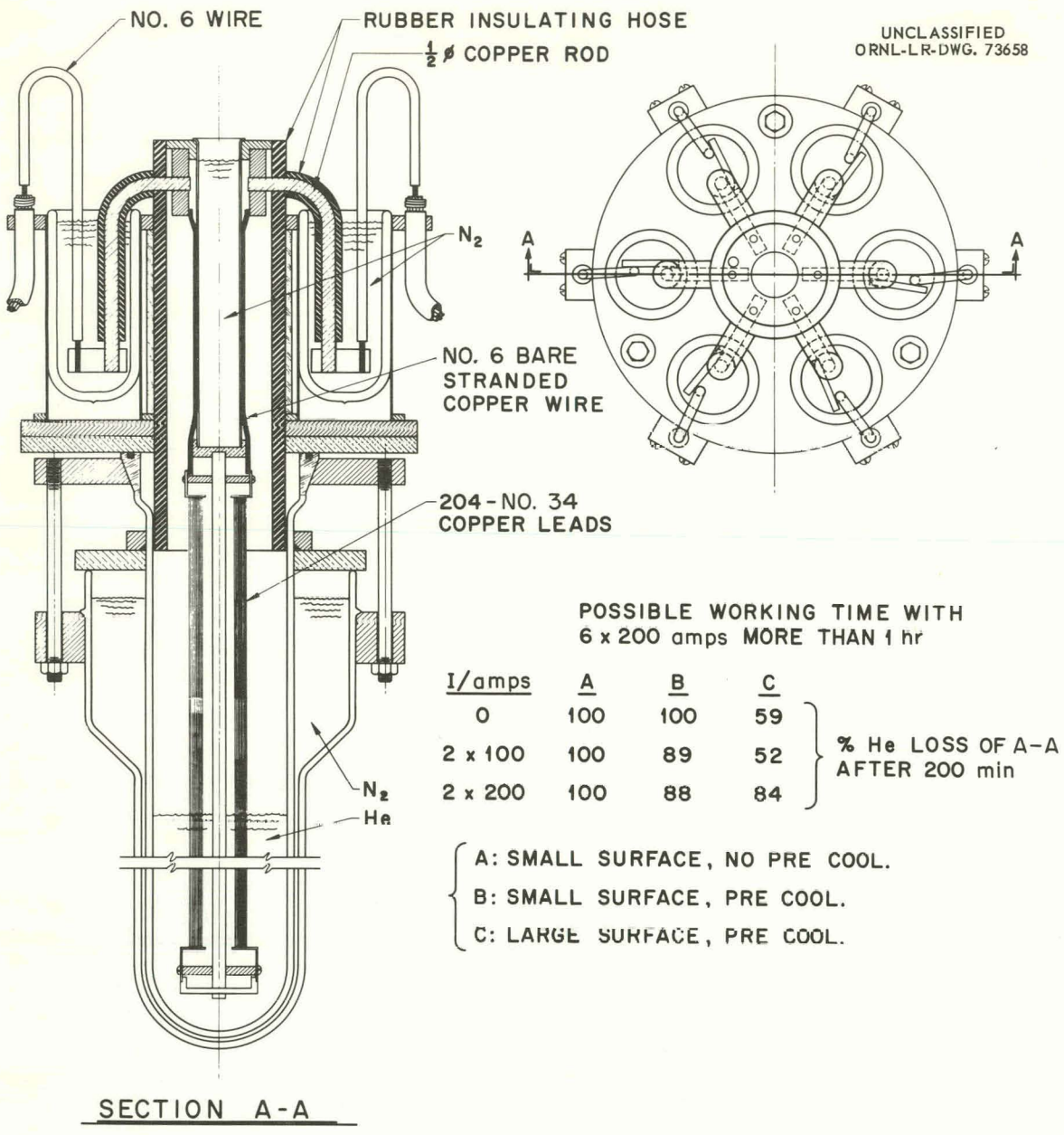

Fig. 7.13. Current Input Apparatus.

slope of the helium level–time diagram for one constant current value (0, 100, and 200 amp, respectively). Taking the slopes as functions of b, it is possible to construct from the composite curve the 0-, 100-, and 200-amp evaporation curves.

These tests were made with nitrogen precooling and enlarged conductor surface as described above (case C). Case B tests were performed with nitrogen precooling and normal conductor surface (current leads consisted of 2 No. 14 copper wires with the same total cross section as the 204 No. 34 wires). The case A test series was with the same reduced conductor surface area and without precooling.

Discussion. – The table in Fig. 7.13 shows the following test results:

1. The apparatus was approximately optimized for a current of 100 amp per lead. With this current, in case C the evaporation rate was about

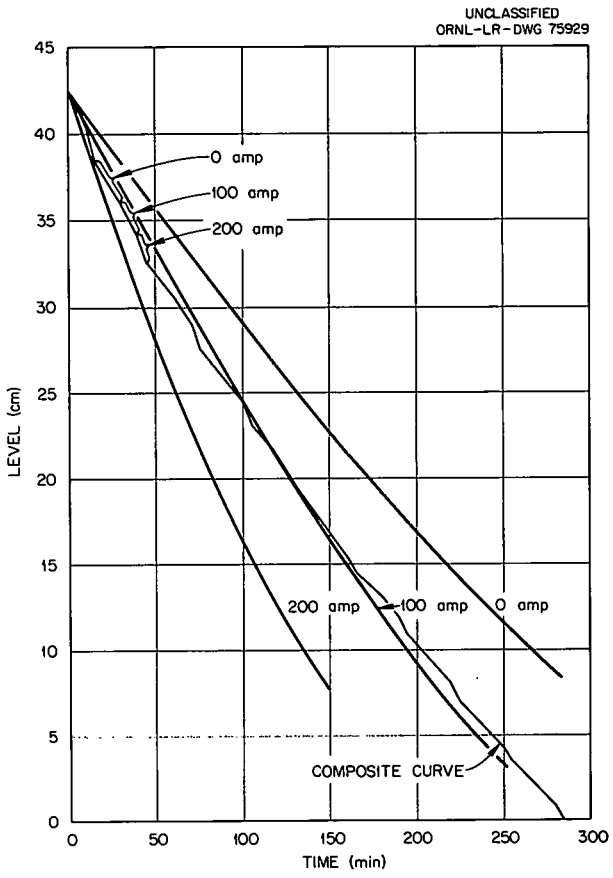

Fig. 7.14. Helium Level–Time (Case C). The composite (crooked) curve shows differing slopes determined by the current input. As the 30-min cycle is repeated, the slopes change as the helium level goes down. The slopes are then picked off the composite curve to derive the complete curves for input currents of 0, 100, and 200 amp.

one-half that measured with the usual type input (i.e., with normal surface and with no precooling, case A). Further refinement of the technique would result in a still greater savings in helium. However, the test demonstrated that the principle is sound.

2. In case C the helium savings at 0 amp is about 40%; at 2 × 200 amp it is about 15% as compared with case A.
3. The influence of the enhanced helium gas cooling due to the enlarged surface is dominant with smaller currents. Nitrogen precooling saves only up to 12% (cases B compared with cases A).
4. With the highest input current (2 × 200 amp), nitrogen precooling saves 12%, whereas the enlarged surface saved only about 4% additional.
5. Even though the design was optimized for 100 amp per conductor, it was found possible to operate at 6 × 200 amp total current for more than 1 hr without helium refilling.
6. The optimization of any design depends on the operating current and duty cycle. The described apparatus approximates the present requirements at this laboratory. Similar designs might be used for other applications. For example, by use of a metal Dewar with high-voltage insulation, the conditions for a superconducting cable can be simulated. A potential of 100 kv to ground on a metal Dewar with a total current input of 1200 amp would correspond to a transmission capacity of 120 Mw for a single dc cable.

7.4 SUPERCONDUCTOR PROXIMITY EFFECTS

W. F. Gauster J. E. Simpkins
W. B. Lacina[11] P. A. Thompson

The problem considered is that of finding the magnetic field produced by two neighboring parallel superconducting wires of arbitrary radii and separation (Fig. 7.15). If it is assumed that the radii R_1 and R_2 are much greater than the penetration depth λ ($\sim 10^{-5}$ cm) and that the surface layer of each wire is superconducting, then the inside of the wire is field-free (Meissner effect) and the external magnetic field can be determined in the same way as the corresponding electrostatic problem (i.e., of finding the electrostatic field produced by two infinitely long, charged cylinders). In both cases the potential outside the cylinders obeys the Laplace equation, and the boundary conditions are identical if potential and stream functions are interchanged.[12,13] The total

[11] Summer employee from Rensselaer Polytechnic Institute.

[12] M. von Laue and F. Moglich, "Uber das Magnetische Feld in der Umgebung von Supraleitern," *Sitzber. preuss. Akad. Wiss., Physik-Math. Kl.* (16), 544–65 (1933).

[13] D. Shoenberg, *Superconductivity*, 2d ed., p 48, Cambridge University Press, New York, 1960.

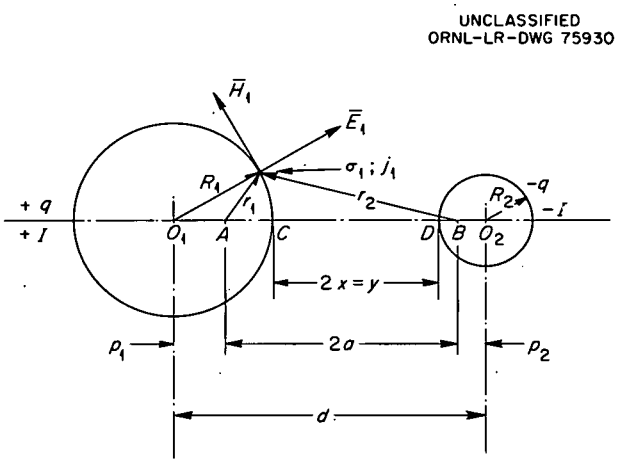

Fig. 7.15. Cross Section of Superconducting Wires (Opposite Currents).

currents carried by each of the superconducting wires correspond to the total charges, and the current densities correspond to the charge densities.

7.4.1 Arbitrary Wire Radii and Opposite Currents of Equal Strength

The simplest case is that for which the currents are equal and opposite. This corresponds to the electrostatic problem of two conducting cylinders with equal, but opposite charges. This problem is easily solved[14] by considering the field due to two line sources with charges $\pm q$ per unit length, placed at the "image points" determined by the data d, R_1, and R_2 (see Fig. 7.15). The distance between the image points is $2a$. An elementary, but lengthy, calculation yields the following results:

$$a^2 = \frac{4}{d^2}\, s(s - R_1)(s - R_2)(d - s)\,, \qquad (1)$$

$$s \equiv \frac{1}{2}(R_1 + R_2 + d)\,.$$

In the following equations, double indices will be used (e.g., $p_{1,2}$ stands for p_1 and p_2, respectively). The plus sign goes with index 1, and the minus sign goes with index 2. All equations are written in the MKS system,

$$p_{1,2} = \frac{1}{2}\left(d - 2a \pm \frac{R_1^2 - R_2^2}{d}\right). \qquad (2)$$

The values of the surface potentials are

$$\phi_{1,2} = \pm \frac{q}{2\pi\epsilon_0} \sinh^{-1} \frac{a}{R_{1,2}}\,. \qquad (3)$$

The magnitude of the electrical-field strength is

$$|\bar{E}_{1,2}| = \pm \frac{qa}{\pi\epsilon_0 r_1 r_2}\,. \qquad (4)$$

Finally, the charge density becomes

$$\sigma_{1,2} = \pm \frac{qa}{\pi r_1 r_2}\,. \qquad (5)$$

The corresponding values for the magnetic-field strengths and the current densities on the surfaces of the superconducting wires are

$$|\bar{H}_{1,2}| = j_{1,2} = \frac{aI}{\pi r_1 r_2}\,. \qquad (6)$$

It can be shown that the maximum values of the field strength occur at points C and D (Fig. 7.15).

The critical current of one single, straight, infinitely long wire made of a soft (ideal) superconductor is (MKS)

$$I_{c0} = 2\pi R H_c\,. \qquad (7)$$

The term $I_{c1,2}$ is defined as that current at which, on one of the wire surfaces, the critical field strength H_c is reached (point C or D). A calculation yields

$$\frac{I_{c1,2}}{I_{c0}} = \sqrt{1 + \frac{R_{1,2}^2}{a^2}} - \frac{R_{1,2}}{a}\,. \qquad (8)$$

The critical current I_c is the smaller of the values I_{c1} and I_{c2}.

Special Cases. – Two special cases were considered for the conditions given in Sec 7.4.1.

(*a*) For $R_1 = R_2 = R$, $I_{c1} = I_{c2} = I_m$. Equation (1) becomes

$$a = \sqrt{\frac{d^2}{4} - R^2}\,, \qquad (9)$$

[14] Ernst Weber, *Electromagnetic Fields*, vol 1, p 119, Wiley, New York, 1950.

and Eq. (8) yields

$$\frac{I_m}{I_{c0}} = \sqrt{\frac{(d/2) - R}{(d/2) + R}} = \sqrt{\frac{x}{x + 2R}} , \qquad (10)$$

where (Fig. 7.15)

$$2x = d - (R_1 + R_2) = d - 2R . \qquad (11)$$

A curve representing Eq. (10) is shown in Fig. 7.16.

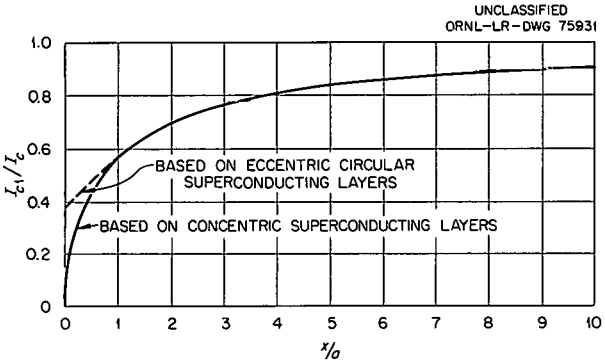

Fig. 7.16. Calculated Critical-Current Curves for Equal-Radii Wires Carrying Equal and Opposite Currents.

(*b*) If $R_2 \to \infty$ (infinite plane), Eq. (8) becomes

$$\frac{I_{c1}}{I_{c0}} = \sqrt{\frac{y}{y + 2R_1}} , \qquad (12)$$

where $y = 2x$. This equation determines the critical current of a superconducting wire with the radius R, which is parallel to a superconducting plane. The distance between wire surface and plane is y. A comparison with Eq. (10) shows that the critical current is the same as in the case of two parallel wires of equal radius R separated $2y$. This can be expected from the well-known solution of the electrostatic analog.

7.4.2 Equal Wire Radii and Equal Currents in the Same Direction

This case corresponds to the electrostatic field distribution of two equally charged cylinders. This problem has been solved by Whipple,[15] who uses the complex function[16]

$$\phi + i\psi = \frac{q}{\pi\epsilon_0} \ln \left[m \, sn \frac{k}{\pi}(u + iv) \right] , \qquad (13)$$

where

$$u + iv = i \ln \frac{z + a}{z - a} . \qquad (14)$$

The term q represents the charge per unit length on both cylinders. The transformation in Eq. (14) defines a curvilinear coordinate system (Fig. 7.17) such that

$$\phi = u , \qquad (15)$$

$$\frac{AP}{BP} = e^v . \qquad (16)$$

If the two conducting cylinders are described by $v = \pm\xi$, then the condition that u be constant over the surface $v = \pm\xi$ is

$$\frac{K'}{K} = \frac{2\xi}{\pi} , \qquad (17)$$

where

$$K = \int_0^{\pi/2} \frac{d\phi}{1 - k^2 \sin^{+2} \phi} ,$$

[15] F. J. Whipple, *Proc. Roy. Soc.* **96A**, 465–75 (1920).

[16] E. Jahnke and F. Emde, *Tables of Functions*, 4th ed., p 92, Dover, New York, 1945.

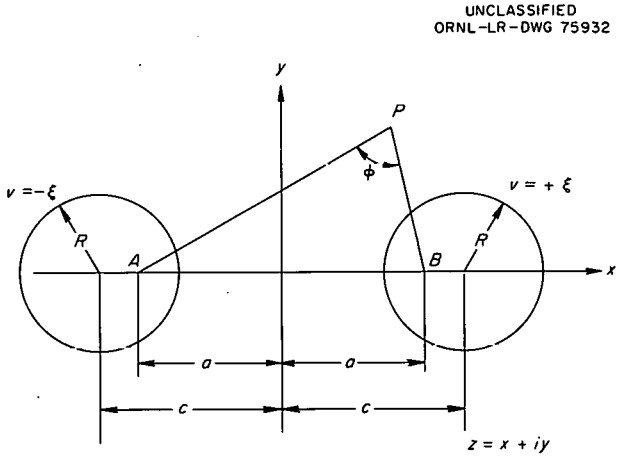

Fig. 7.17. Cross Section of Superconducting Wires (Currents in Same Direction).

and

$$K' = \int_0^{\pi/2} \frac{d\phi}{1 = (1 - k^2) \sin^2 \phi} .$$

The real and imaginary periods of the elliptic function *sn* are $4K$ and $2iK'$ respectively. It is easily shown that

$$\frac{c}{R} = \cosh \xi . \tag{18}$$

Only the results will be given here; see Whipple's paper[15] for more details. On the cylinders,

$$H = j = \frac{KI}{\pi^2 R} \left(dn \frac{2uK}{\pi} + K\, cn \frac{2uK}{\pi} \right) \times \left(\frac{\cos \xi - \cos u}{\sinh \xi} \right) . \tag{19}$$

At the nearest points, $\phi = u = \pi$, and

$$H = H_1 = \frac{KI}{\pi^2 R} (1 - K) \coth \frac{\xi}{2} . \tag{20}$$

At the far points, $\phi = u = 0$, and

$$H = H_2 = \frac{KI}{\pi^2 R} (1 + K) \tanh \frac{\xi}{2} . \tag{21}$$

Again, with $I_{c0} = 2\pi R H_c$, one can write

$$\frac{H_1}{H_c} = \left[\frac{2K}{\pi} (1 - K) \coth \frac{\xi}{2} \right] \frac{I}{I_{c0}} , \tag{22}$$

$$\frac{H_2}{H_c} = \left[\frac{2K}{\pi} (1 + K) \tanh \frac{\xi}{2} \right] \frac{I}{I_{c0}} . \tag{23}$$

Numerical values may be obtained from tables in which linear dimensions and fields are tabulated as a function of k, the modulus of the elliptic function. Since $H_2 > H_1$, the critical current I_c of this wire arrangement is obtained by making $H_2 = H_c$. This yields

$$\frac{I_c}{I_{c0}} = \frac{\pi}{2K (1 + K)} \coth \frac{\xi}{2} . \tag{24}$$

Table 7.2, adapted from Whipple's paper, gives some values for this equation.

7.4.3 General Cases

The case of equal wire radii and arbitrary currents can be solved by superposition of the solutions of Secs 7.4.1 and 7.4.2. A general solution

Table 7.2. Dependence of the Current Ratios I_c/I_{c0} from the Spacing Ratios d/R

$\sin^{-1} k$	ξ	$d/R = 2 \cosh \xi$	Opposite Currents[a]	Equal Currents[a]	One Wire with No Current[a]
0	0	0	1.000	1.000	1.000
10°	3.129	22.904	0.917	0.923	1.000
20°	2.429	11.430	0.838	0.862	0.999
30°	2.009	7.594	0.764	0.814	0.994
40°	1.705	5.686	0.692	0.775	0.985
50°	1.447	4.484	0.619	0.742	0.959
60°	1.228	3.706	0.547	0.714	0.915
70°	1.016	3.124	0.468	0.690	0.854
80°	0.789	2.654	0.371	0.669	0.729
89°	0.454	2.210	0.223	0.647	0.446
90°	0	2.000	0	0.637	0

[a] (I_c/I_{c0}).

(any radii and any currents) is given by Buchholz.[17]

7.4.4 Experiments

Experiments were made in order to investigate special case (*b*) as described in Sec 7.4.1. For these experiments tin wires about 20 mils in diameter were arranged parallel to a superconducting plane [see Eq. (12)] at a distance of about 1 to 2 mils (thickness of a mica sheet). The wire was made of 99.999% tin (Light and Co.), and the superconducting plane was represented by a 2-mil lead foil resting on a flat piece of brass. The resistance of the wire during the transition from superconducting to normal was measured by a recording instrument capable of indicating 10^{-8} v. The potential contacts were mechanical rather than soldered. The normal resistance, R_n, of the wire was measured at a helium vapor pressure of 560 torr, corresponding to 3.91°K.

The first run (R/R_n) vs I was made without the superconducting lead foil and showed a critical current of I_{c0} = 2.75 amp (Fig. 7.18, o points). After inserting the superconducting lead foil, the intermediate state started at about I_m = 1.6 amp (Fig. 7.18, Δ points), and the resistance-current curve became much flatter. Finally, a run without lead foil was repeated (for control purposes), which showed very close to the same performance as the first run (Fig. 7.18, • points).

With the dimensions used, the calculation in Eq. (12) predicts I_m between about 0.6 and 1.0 amp. When the uncertainties of the measurements are considered, it is very difficult to decide whether there is really a superconducting zone between $I = I_m$ and I = 1.6 amp or whether the immediate state curve ("with mirror plane") has actually a tail which begins at I_m.

Experiments and theoretical work will be continued, directed not only toward a more detailed understanding of the special case described, but also toward more general configurations.

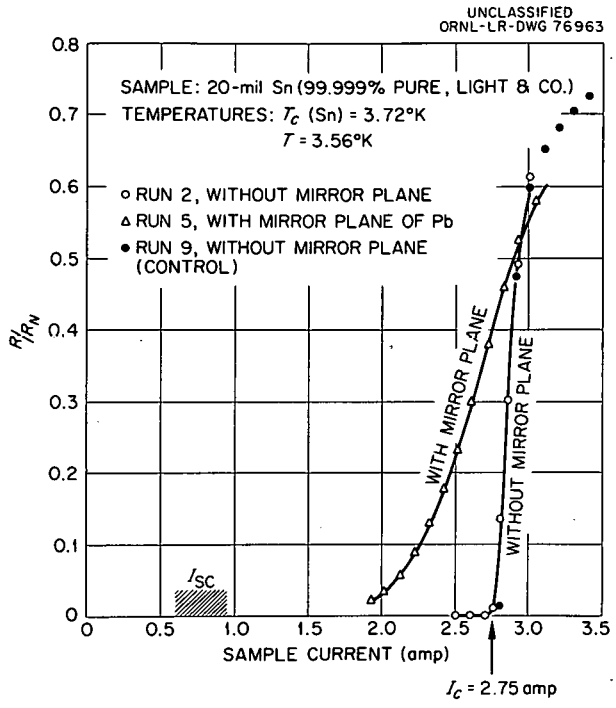

Fig. 7.18. Intermediate-State Curves for Single Wire and for Wire with Superconducting Plane.

[17] H. Buchholz, *Elektrische and Magnetische Potentialfelder*, p 11, Springer-Verlag, Berlin, 1957.

8. Vacuum Systems, Techniques, and Material Studies

R. E. Clausing[1] J. D. Redman[2] R. A. Strehlow[2]

8.1 METAL-FILM PUMPING

The data for the sticking factors of various gases on vapor-deposited titanium films have been extended to include information for water vapor and the effect of system bakeout. The apparatus has been described previously.[3] Both water-cooled (10°C) and liquid-nitrogen-cooled (−195°C) substrates were used. The inner-vacuum vessel was baked to approximately 400°C for 16 hr prior to each set of measurements. These data are summarized in Table 8.1 along with previously reported data obtained with baking the substrate.

[1]Metals and Ceramics Division.

[2]Reactor Chemistry Division.

[3]R. E. Clausing *et al.*, *Thermonuclear Div. Semiann. Progr. Rept. Apr. 30, 1962*, ORNL-3315, p 79 ff.

Table 8.1. Initial Sticking Probabilities of Various Gases on Vapor-Deposited Titanium Films

Gas	Liquid N_2 Cooling		Water Cooling	
	Baked	Unbaked	Baked	Unbaked
H_2	0.84	0.24		0.07
H_2O			0.25	0.20
D_2	0.75		0.27	(0.07 for H_2)
N_2	0.90	0.85	0.15	0.08
CO	0.98	0.95	0.38	0.38
CO_2			0.6	>0.4
O_2	0.98			

The pressures during titanium deposition were 2×10^{-8} to 2×10^{-7} torr for unbaked water-cooled substrates and 2×10^{-9} to 7×10^{-9} torr for film deposited on baked substrates. The generally higher sticking factors obtained in the baked system are not completely understood, but are probably related to the lower degree of contamination of the titanium film which is expected for films evaporated in baked systems. For hydrogen, preliminary experiments have shown that film intentionally contaminated with oxygen or nitrogen during evaporation has sticking fractions only slightly lower than those for the baked surfaces.

8.2 VACUUM INSTRUMENTATION

8.2.1 Nude-Gage Calibration

It has been observed that a nude gage operating in a vacuum system pumped by a poorly trapped oil-diffusion pump yields pressure readings inconsistent with those obtained from a tubulated gage. The results observed appear to correlate the nude and enveloped gages by a relation of the form

$$p_n = a p_{en} + p_r ,$$

where p_n is the pressure or current reading of the nude gage, p_{en} is the pressure or current reading for the enveloped standard gage, and p_r is a residual pressure, which, for the gages in the particular vacuum environment studied at this laboratory, is positive. Different gage designs and modifications have been used which, when analyzed in terms of this relation, give values for a of about

0.6; one earlier calibration system[4] showed a time-dependent decrease of a. The "residual" term, p_r, has been studied in a series of tests in which one parameter of the vacuum system was changed at a time. It was found that the value of p_r was a function of the oil used in the diffusion pump. Indeed, a test with a similar gage system in a mercury diffusion pump showed no departure from linearity down to the middle of the 10^{-8}-torr scale. Some calibration curves with four fluids are shown in Fig. 8.1. The gages for

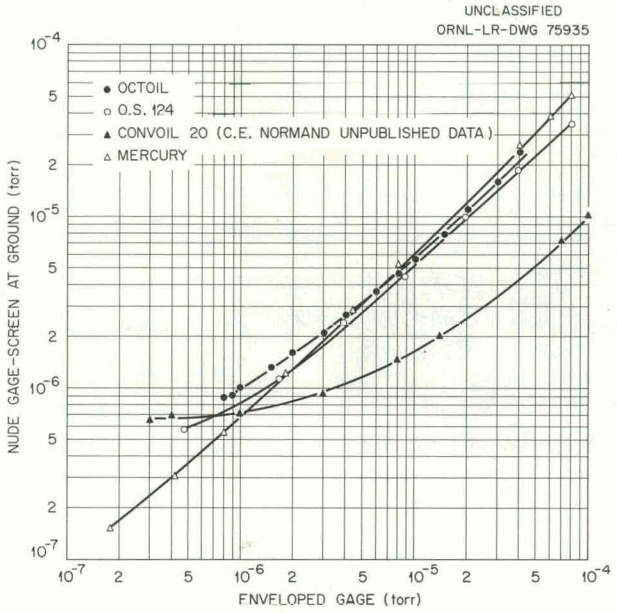

Fig. 8.1. Gage Calibration for Various Pump Fluids.

the mercury, Octoil, and OS-124 (polyphenyl ether) tests were nearly identical in construction and presumably different from the gage used for the Convoil, thus accounting for the substantial difference in calibration from the earlier work. In the region of lowest pressure, it is quite likely that the residual term will be a complex function of relative adsorption and desorption rates of the various background species, with this being noticeable in systems in which the limiting gas composition is different from that of the present work.

[4]C. E. Normand *et al., Thermonuclear Div. Semiann. Progr. Rept. Jan. 31, 1961*, ORNL-3104, p 134.

8.3 DIFFUSION-PUMP STUDIES

8.3.1 Experimental Surface-Boiling Diffusion Pump

Polyphenyl ethers, which have vapor pressures of as low as 2×10^{-9} torr at room temperature, have been shown to be significantly more stable to thermal decomposition than other common oils.[5] Comparative tests run with a vacuum system using Octoil and the five-ring polyphenyl ether show a more rapid pumpdown and a somewhat lower base pressure for the polyphenyl ether. (These results are shown in Table 8.2.) Some operating experience using the ether oil in metal pumps indicates that after a protracted period of pumping, the oil appears very dark and apparently quite contaminated. This is probably due to forepump oil contamination followed by decomposition in the diffusion pump because of the normal higher boiler temperature in the diffusion pump when using this oil.

Table 8.2. Attainable Pressures in Unmodified PMC-720 Pump with Octoil and with Polyphenyl Ether

Pumping Time (days)	Pressure (torr)	
	Octoil	Polyphenyl Ether
1	1.2×10^{-5}	1.4×10^{-6}
2	2×10^{-6}	1×10^{-6}
9	1.2×10^{-6}	8.4×10^{-7}
29	1.2×10^{-6}	7×10^{-7}
60		4×10^{-7}

An experimental diffusion pump utilizing a surface heater composed of corrugated 1-in.-wide Chromel ribbon spirally wound with silica-glass cloth tape as insulation has been constructed and studied. This pump is shown in Fig. 8.2. In this assembly the heater is segmented to allow a considerable variation of relative amounts of oil through the top jet as compared with the second and third jets of the pump. Pumping speeds for hydrogen have been found to be

[5]R. E. Clausing *et al., op. cit.*, p 84.

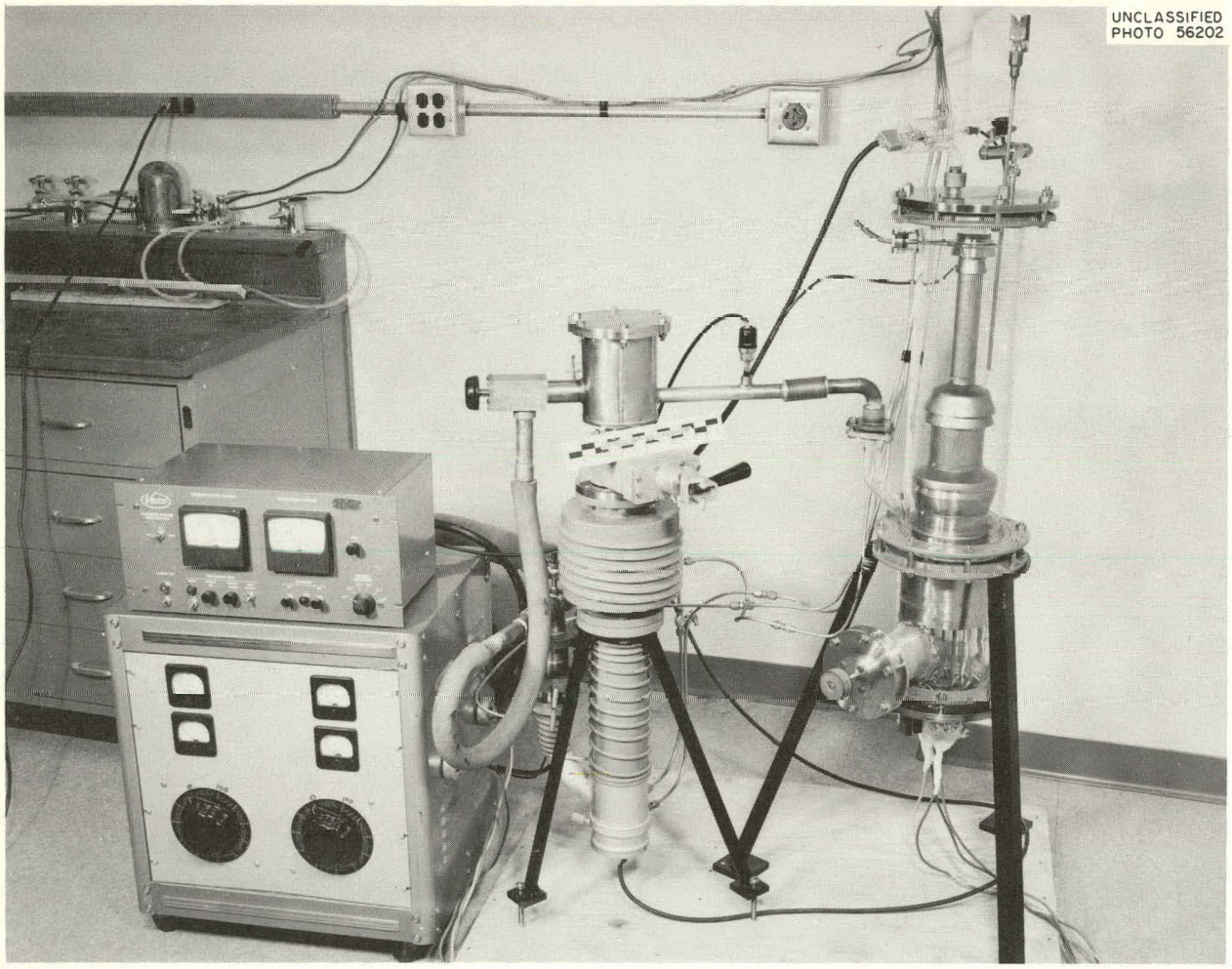

Fig. 8.2. Experimental Diffusion-Pump Assembly.

strongly dependent on oil throughput into the top jet. At a boiler temperature of 287°C the pumping speed for hydrogen was found to be 1.5 ± 0.3 times that for air. At 296°C this ratio had increased to 2.25 ± 0.4. The oil height in the boiler region has been varied with similar effects.

8.3.2 Diffusion-Pump Mechanism

The suggestion has been made that some fraction of the pumping action of a diffusion pump might be related to an adsorption of gas on the deposited oil film falling down the inner wall of the diffusion pump. Equipment was assembled which allowed this possibility to be tested. An oil circulating system was constructed in a vacuum system which consisted of a 6-in.-diam glass pipe 3 ft long. In the glass pipe was placed an 8-in.-long cylinder which had an annular conductance of a few liters per second. Oil passed through a set of small holes in a torus at the top of the glass pipe, thus generating a film of oil which flowed downward at a rate of about 8 in./sec into the lower part of the pipe, in which the oil area decreased and in which the oil could be heated to about 40°C higher than the inlet temperature. A distinct pumping action was observed at pressures of 10^{-3} to 10^{-2} torr, but not at pressures of 10^{-5} to 10^{-4} torr. This demonstrated that the suggested mechanism does not play a significant part in the pumping action of a diffusion pump.

9. Speculation on the Attainment of a High Density and a Large Circulating Current of Very Hot Protons in a Magnetic-Mirror Device

J. R. McNally, Jr.

9.1 INTRODUCTION

Some provocative speculations on the prospects and properties of a steady-state fusion plasma are under consideration.[1] The following sections consider the prospects of producing a high density ($\gtrsim 10^{12}$ protons/cm^3) of very hot protons in a magnetic-mirror device. The injection of 6-Mev molecular hydrogen ions into a 30,000-gauss field leads to very favorable Lorentz trapping with very small charge-exchange losses, perhaps permitting the attainment of multikiloamperes of circulating protons. Plasma pumping of neutral gas would be very large, the plasma approaching a black body. The exponentiation of the proton population to still higher densities and trapped currents may occur under certain conditions. It may be possible that the attainment of a large azimuthal current will lead to a natural plasma configuration in which the applied mirror magnetic field and the self-field of the proton current produce a closed toroidal magnetic bottle.

9.2 ON THE POSSIBILITY OF MULTIKILOAMPERES OF CIRCULATING IONS IN A MAGNETIC-MIRROR DEVICE

The Lorentz ($v \times H$) breakup of the molecular hydrogen ion[2] may lead to a high density of trapped protons and hence large azimuthal current in a magnetic-mirror device by the choice of very high injection energy and strong magnetic fields. If plasma exponentiation should also occur, it may be possible to enhance the containment and heating of secondary plasma through a closing of the magnetic mirror by the azimuthal proton current, thus producing an endless toroidal magnetic bottle defined by the applied mirror magnetic field and the self-field of the trapped-ion current.

The equilibrium average proton density in a very-high-energy DCX-1–like device is, for the nonexponentiating case and neglecting Coulomb scattering losses which are small,

$$\bar{n}_+ = \frac{I_{2+}\beta_L}{n_0 \sigma_{\text{loss}} v_+ V},$$

where β_L is the Lorentz breakup fraction (see Sec 9.3), I_{2+} the injection current of H_2^+ in particles/sec, n_0 the neutral background gas density, σ_{loss} the loss cross section (see Sec 9.4), v_+ the proton velocity, and V the volume occupied by the trapped protons. The peaking of the trapped-proton density in the median plane of the magnetic mirror may give significantly higher local density.

The circulating proton current is, since the trapped protons encircle the magnetic axis,

$$I_+ = \bar{n}_+ A v_+ \simeq \frac{n_+ V v_+}{l}$$

$$\simeq \frac{I_{2+}\beta_L}{n_0 \sigma_{\text{loss}} l},$$

[1] A very conjectural report, *Speculations on a Steady-State Fusion Plasma*, is in preparation.

[2] J. R. Hiskes and J. L. Uretsky, *Dissociation of H_2^+ Ions by Electric Fields*, UCRL-8255 (1958); see also, J. R. Hiskes, *Phys. Rev.* **122**, 1207 (1961).

where I_+ is the azimuthal proton current and l is the average proton orbit circumference.

DCX-1 parameters applicable to this problem, if the field is scaled upward by a factor of $\sqrt{10}$ in the case of 6-Mev H_2^+, are

1. maximum absolute containment volume, $V \cong 24{,}000\ cm^3$;
2. average proton orbit circumference, $l \cong 50$ cm;
3. minimum background gas density (hydrogen), $n_0 \cong 3 \times 10^8\ H_2^0/cm^3$.

Injection currents will be assumed to be 8-ma H_2^+ at 3 Mev into a 20,000-gauss field and 4-ma H_2^+ at 6 Mev (ref 3) into a 30,000-gauss field. Table 9.1 gives the proton density and current for these two cases.

Actually, it may be necessary to increase the background gas density to suppress plasma blowup and to reduce the plasma potential, if they are deleterious. Table 9.2 gives the dependence of trapped-proton current on neutral background gas pressure. Thus it appears that it may be possible to attain multikiloamperes of circulating protons by the Lorentz trapping process involving very high H_2^+ velocities and strong magnetic fields. Other trapping processes may permit plasma growth to still higher currents[4] and densities (see Sec 9.5).

Partial burnout and heating of cold plasma should enhance the possibility of attaining very high densities, since the chances for charge-exchange events and energy degradation losses are reduced. The burnout percentage, neglecting secondary processes, may be defined as

$$\frac{N_0 - \bar{n}_0}{N_0}(100) = \frac{100}{1 + (V_g S/4\bar{n}_+ \sigma_i v_+ V)},$$

where N_0 is the gas density external to the plasma, $\bar{n}_0$ the average gas density in the plasma, v_g the gas molecule velocity ($v_g \leq 2 \times 10^5$ cm/sec), S the plasma surface area (assumed 4800 cm^2), and σ_i the ionization cross section of H_2^0 by fast protons. At 10^{-8} torr the average burnout throughout the whole volume is ~20 and ~68 percent for 3 and 6 Mev respectively. At the symmetry orbit in the median plane of the magnetic mirror, where exponentiation should predominate, the burnout is significantly greater. Under such conditions of partial burnout it may therefore be feasible to increase the background gas pressure to reduce instabilities and plasma potential.

Table 9.2. Effect of Gas Pressure on Resulting Azimuthal Proton Current

Pressure (H_2) (torr)	I_+ (3-Mev H_2^+) (amp)	I_+ (6-Mev H_2^+) (amp)
10^{-8}	5,000	60,000
10^{-7}	500	6,000
10^{-6}	50	600

9.3 EVALUATION OF THE LORENTZ BREAKUP FRACTION

The Lorentz breakup of H_2^+ by the apparent electric field (i.e., $\xi = v \times H/c$) experienced by very-high-velocity H_2^+ injected into a high-magnetic-field region can be several orders of magnitude greater than gas breakup at low pressures. In this section we shall analyze the

[3] Radiation Dynamics, Inc., markets a 3-Mev, 10-ma accelerator and have proposed a 6-Mev, 5-ma unit. O. B. Morgan, Jr., ORNL, indicates that the efficiency for H_2^+ production in an ion source can approach 80%.

[4] The azimuthal current required to close the magnetic mirror is only about 400,000 amp.

Table 9.1. Calculated Proton Density and Current Attainable with Very-High-Energy Injection

$E(H_2^+)$ (Mev)	v_+ (cm/sec)	σ_{loss} (cm^2/H_2^0)	β_L	$\bar{n}_+$ (H^+/cm^3)	I_+ (amp)
3	$< 1.7 \times 10^9$	3.9×10^{-21}	3.6×10^{-5}	$> 4 \times 10^{10}$	5,000
6	$< 2.4 \times 10^9$	6.5×10^{-22}	1.5×10^{-4}	$> 3 \times 10^{11}$	60,000

experimental data of Riviere and Sweetman[5] since it gives the *lowest* measured breakup fractions as a function of applied electric field. Riviere and Sweetman used H_2^+ from an rf source to obtain the data but found that H_2^+ formed from H_3^+ gave about six times more Lorentz breakup. Ehler[6] observed breakup fractions about ten times larger than those used here for the direct H_2^+ dissociation. Kaplan, Paulikas, and Pyle,[7] using H_2^+ from H_3^+, obtained $v \times H$ breakup values intermediate between the two cases studied by Riviere and Sweetman. They also found no breakup of H_2^+ or H_3^+ obtained directly from their P.I.G. source, but attributed this to the method of formation and possible de-excitation in the ion source. Both Hiskes and Pyle[8] have suggested that the Riviere and Sweetman values used here are probably too conservative in terms of H^0 or H_2^+ from H_3^+ injection.

In the H_2^+ experiment of Riviere and Sweetman, the H_2^+ velocity of 1.4×10^9 cm/sec gave a dissociation time of 7×10^{-11} sec or shorter. Thus, breakup in a magnetic mirror would occur in times of this order or less for the same $\xi = v \times H/c$. Breakup involving longer τ's would permit greater magnetic-field penetration.

The data of Riviere and Sweetman for direct H_2^+ breakup can be fitted to the quadratic equation

$$B = 1.29 \times 10^{-4} - 1.11 \times 10^{-7}\xi + 2.43 \times 10^{-9}\xi^2 ,$$

where B is the breakup fraction and ξ is the electric field in kv/cm.

The injection of H_2^+ ions into a magnetic-mirror field will give Lorentz breakup along the ingoing path according to the appropriate equivalent electric field and the proper dissociation τ's. The net breakup is given by the fractional breakup, β, associated with the allowed change in magnetic field. The DCX-1 type of magnetic-mirror configuration permits trapping into absolutely contained orbits[9] for $\Delta H/H = 0.06$, where H is the magnetic field. Thus, we obtain

$$\frac{dB}{d\xi} = -1.11 \times 10^{-7} + 4.86 \times 10^{-9}\xi = \frac{\Delta B}{\Delta \xi}$$

and

$$\Delta\xi = \frac{\Delta H}{H}\xi = 0.06\,\xi .$$

Therefore,

$$\beta_L = \Delta B = -0.67 \times 10^{-8}\xi + 2.92 \times 10^{-10}\xi^2 .$$

Table 9.3 gives the predicted Lorentz breakup fraction, β_L, the background-gas breakup fraction ($\beta_G = n_0 \sigma_{Bu0} L$, where $n_0 = 3 \times 10^8$ $H_2{}^0/cm^3$, $L = 27$ cm, and σ_{Bu0} is taken from Barnett, Gauster, and Ray[10]), and the ratio of the two breakup fractions for various energies.

Table 9.3 Lorentz and H_2^0 Gas Breakup Fractions vs Energy

$E(H_2^+)$	ξ (kv/cm)	β_L	β_G	β_L/β_G
600 kev	70	1.0×10^{-6}	7×10^{-7}	1.4
1 Mev	120	3.4×10^{-6}	6×10^{-7}	6
3 Mev	360	3.6×10^{-5}	$\sim 3 \times 10^{-7}$	$\sim$120
6 Mev	720	1.5×10^{-4}	$\sim 8 \times 10^{-8}$	$\sim$1900

9.4 EVALUATION OF THE LOSS CROSS SECTION FOR ENERGETIC PROTONS IN GAS

The loss cross section, σ_{loss}, used in Sec 9.2, is arbitrarily defined as the stopping-power cross section for an energetic proton to degrade in

[5] A. C. Riviere and D. R. Sweetman, *Phys. Rev. Letters* 5, 560 (1960).

[6] A. W. Ehler, *Studies of H_2^+ Dissociation*, TID-14428 (1961).

[7] S. N. Kaplan, G. A. Paulikas, and R. V. Pyle, *Phys. Rev. Letters* 7, 96 (1961); see also, S. N. Kaplan, G. A. Paulikas, and R. V. Pyle, *Phys. Rev. Letters* 9, 347 (1962) for Lorentz dissociation of H^0.

[8] J. R. Hiskes and R. V. Pyle, oral discussions at ORNL, Oct. 2, 1962.

[9] J. L. Dunlap, *Some Calculations Involving the DCX-1 Containment Theory*, DCX-1 TM-19 (April 1962); R. J. Mackin, Jr., p 156 in *The ORNL Thermonuclear Program*, ORNL-2457 (Jan. 15, 1958). Actually, trapping will also occur r-wise for $0.06 < \Delta H/H \leq 0.5$, but the containment zones are open z-wise and gross scattering into the z direction can result in proton loss. The figure of 0.06 is probably conservative.

[10] C. F. Barnett, W. F. Gauster, and J. A. Ray, *Atomic and Molecular Collision Cross Sections of Interest in Controlled Thermonuclear Research*, ORNL-3113 (May 1961), with extrapolation to 6 Mev.

energy from E_0 to 1 Mev. It is given by $\sigma_{loss} = 1/n_0\lambda$, where $\lambda = R_{E0} - R_{1.0}$ (R is the range of the proton in the gas) and n_0 is the density in molecules/cm^3. Data for R at 15°C and 760 torr ($n_0 = 2.55 \times 10^{19}$ molecules/cm^3) are taken from Segrè.[11]

Table 9.4 lists data of interest. For comparison, the charge-exchange cross section for 1-Mev protons is 4×10^{-22} cm^2/$H_2{}^0$ and 4×10^{-20} cm^2/$N_2{}^0$.

Table 9.4. Ranges and Loss Cross Sections of Energetic Protons in Gas

Gas	E_0 (H^+) (Mev)	R_{E_0} (cm)	$R_{1.0}$ (cm)	λ (cm)	σ_{loss} (cm^2/molecule)
H_2	1.5	20	10	10	3.9×10^{-21}
H_2	3.0	70	10	60	6.5×10^{-22}
Air	1.5	4.4	2.3	2.1	1.9×10^{-20}
Air	3.0	14	2.3	12.0	3.3×10^{-21}

It should be recognized that an increase in plasma potential from zero will introduce an additional loss above that derived from stopping-power considerations alone. (The protons will also produce fewer ion pairs, at least directly in this case.) At densities consistent with exponentiation these potentials should be relatively low. However, a 3 kv plasma potential increases the energy loss rate roughly a hundredfold. Hence, these loss cross sections refer to a reasonably-well-neutralized plasma which may be possible only at background densities somewhat in excess of 3×10^8 $H_2{}^0$/cm^3.

9.5 PRIMARY EXPONENTIATION IN A VERY-HIGH-ENERGY DCX-1–LIKE DEVICE

The condition for primary exponentiation in a DCX-1–like device is that the rate of trapping protons from $H_2{}^+$ by the already trapped protons (and associated electrons) equals or exceeds the rate of loss of protons from the plasma; that is,

$$I_{2+}(n_+\sigma_{Bu+} + n_-\sigma_{Bu-})L \geq n_+ n_0 \sigma_{loss} v_+ V ,$$

where n_+, n_-, and n_0 are the proton, electron, and neutral densities, σ_{Bu} the breakup cross section, L the effective breakup path length to give protons trapped in the absolute containment volume V, I_{2+} the injection current, σ_{loss} the loss cross section (see Sec 9.4), and v_+ the mean proton velocity.

We shall take σ_{Bu-} as one-half the cross section for ionizing $H_2{}^0$ to $H_2{}^+$ at the velocity of the $H_2{}^+$ relative to resting electrons and obtain $\sigma_{Bu-} \tilde{=} 1.7 \times 10^{-17}$ cm^2 for 3-Mev $H_2{}^+$ and 0.9×10^{-17} cm^2 for 6-Mev $H_2{}^+$. The value of σ_{Bu+} is taken from Gerjuoy[12] for the charge-transfer process

$$H_2{}^+ + H^+ \rightarrow 2H^+ + H^0$$

at a relative velocity of about 10^9 cm/sec ($\sigma_{Bu+} \tilde{=} 1.7 \times 10^{-17}$ cm^2), and after making a rough correction for center-of-mass motion we obtain $\sigma_{Bu+} = 0.9 \times 10^{-17}$ cm^2 (actually as a result of the very fast Lorentz trapping the relative velocity of $H_2{}^+$ and the H^+ may be lower and σ_{Bu+} possibly larger for breakup on recently trapped protons). Thus, using $n_+ = n_-$, we obtain

$$\sigma_{Bu+} + \sigma_{Bu-} = \begin{cases} 2.6 \times 10^{-17} \text{ cm}^2 \text{ for 3-Mev } H_2{}^+ \\ 1.8 \times 10^{-17} \text{ cm}^2 \text{ for 6-Mev } H_2{}^+ . \end{cases}$$

The value of V/L will be taken to be the *maximum* allowable based on the largest absolute containment volume; that is, $V/L = 900$ for $V = 24{,}000$ cm^3 and $L = 27$ cm. The density n_0 will be taken to be 3×10^8 $H_2{}^0$/cm^3, and the mean velocity v_+ of trapped protons is 1.5×10^9 cm/sec for 3-Mev $H_2{}^+$ and 1.9×10^9 cm/sec for 6-Mev $H_2{}^+$. The loss cross sections are taken from Table 9.4 and are 3.9×10^{-21} cm^2 and 6.5×10^{-22} cm^2 for 3- and 6-Mev $H_2{}^+$ injection into $H_2{}^0$ gas respectively. The critical current for exponentiation is therefore

$$I_{2+} \geq \begin{cases} 10.2 \text{ ma for 3-Mev } H_2{}^+ \\ 3.1 \text{ ma for 6-Mev } H_2{}^+ . \end{cases}$$

Lorentz trapping should reduce these figures somewhat because of (1) density peaking of recently trapped protons on the median plane,

[11] E. Segre, *Experimental Nuclear Physics*, vol I, Wiley, New York, 1952.

[12] E. Gerjuoy, *Dissociation and Ionization of $H_2{}^+$ by Fast Protons*, NP-7170 (1960).

(2) increased Gerjuoy breakup with lower relative velocity of the recently trapped protons, and (3) partial burnout of the gas background near the symmetry orbit where exponentiation commences.[13] If localized fast trapping is significant, V/L may be 300 (or smaller) and the critical currents are reduced to 3.4 ma and 1.0 ma (or smaller respectively.

It is possible that somewhat higher H_2^+ currents may be required for exponentiation if the plasma potential, gas density, and plasma volume are incompatible with the above suggested critical currents.

[13] Lorentz trapping of 6-Mev H_2^+ with its accompanying partial burnout gives a theoretical S curve having a critical current for exponentiation of only 800 μa; inclusion of plasma pumping in addition indicates that only 300 μa may be needed to attain a Coulomb-scattering-limited density.

9.6 GENERAL COMMENTS

The use of such high-energy protons automatically introduces radiation hazards due to x rays and energetic-proton reactions with wall materials; in addition, the possible uniqueness of plasma configuration properties brought about by a very large circulating ion current and ion temperature of possibly ten billion degrees suggests that appropriate precautionary procedures be introduced.

9.7 ACKNOWLEDGMENT

Acknowledgment is made to E. D. Shipley for many stimulating and fruitful discussions.

10. Design and Engineering — Service Report

J. F. Potts, Jr.

Design activities of the Engineering Services Group are summarized as follows:

Jobs on hand May 1, 1962, on which work had not started	20
New jobs received	200
Total jobs	220
Jobs completed	208
Jobs in progress	9
Backlog of jobs Oct. 31, 1962	3
Total drawings completed for period (does not include report and slide drawings)	303
Overtime (draftsmen, man-days)	3

Although the flow of work, in numbers of jobs and drawings, increased during this interval, the average complexity of jobs has been less than in previous periods. This reflects the fact that the engineering effort has been on modification or extension of existing facilities with relatively little effort on new systems. The reduced design work load has allowed some time for members of the group to work closely with various research teams for short intervals. This opportunity is yielding the expected dividends of: (1) understanding true working conditions, (2) learning how criteria for design jobs materialize, and (3) seeing the results of design in action.

Shop fabrication for the period is summarized as follows:

Jobs requiring 16 man-hours or less	218
Jobs requiring up to 1200 man-hours	343
Jobs requiring up to 2000 man-hours	3
Miscellaneous jobs in plating, carpenter, electrical, and millwright shops	97
Jobs by outside contractors	0
Average manpower (per week)	33.2

Publications and Papers

PUBLICATIONS

OPEN LITERATURE

Author(s)	Title of Article	Journal
Igor Alexeff, R. V. Neidigh, and E. D. Shipley	Experiments Concerning the Magnetic Confinement of a Cold Plasma	*J. Nucl. Energy: Pt C* **4**, 263 (1962)
Igor Alexeff and R. V. Neidigh	Experimental Observation of Plasma Electron Pressure	*Phys. Rev.* **127**, 1 (1962)
Igor Alexeff and R. V. Neidigh	Observation of Ionic Sound Waves in Gaseous Discharge Tubes	*Proc. Intern. Conf. Ionization Phenomena in Gases, 5th, Munich, 1961*, **2**, 1523 (1962)
M. C. Becker, R. A. Dandl, H. O. Eason, A. C. England, R. J. Kerr, and W. B. Ard	An Investigation of Electron Heating at the Cyclotron Frequency	*Nucl. Fusion: 1962 Suppl, Pt 1*, 345
J. L. Dunlap, C. F. Barnett, R. A. Dandl, and Herman Postma	Radiation and Ion Energy Distributions of the DCX-1 Plasma	*Nucl. Fusion: 1962 Suppl, Pt. 1*, 233
P. R. Bell, G. G. Kelley, N. H. Lazar, and R. J. Mackin, Jr.	The DCX-2 Program of Plasma Accumulation by High-Energy Injection	*Nucl. Fusion: 1962 Suppl, Pt 1*, 251
W. F. Gauster, G. G. Kelley, R. J. Mackin, Jr., and G. R. North	Calculation of Ion Trajectories and Magnetic Fields for the Magnetic Trapping of High-Energy Particles	*Nucl. Fusion: 1962 Suppl, Pt 1*, 239
R. A. Gibbons and R. J. Mackin, Jr.	Development and Study of a Highly Ionized Steady-State Deuterium Plasma	*Proc. Intern. Conf. Ionization Phenomena in Gases, 5th, Munich, 1961*, **2**, 1769 (1962)

J. F. Potts, Jr., and D. L. McElroy[1]	The Effects of Cold Working, Heat Treatment, and Oxidation on the Thermal emf of Nickel-Base Thermoelements	*Temperature, Its Measurement and Control in Science and Industry* (ed. by A. I. Dahl), vol 3, Pt. 2, pp 243–64, Reinhold, New York, 1962
W. L. Stirling	Experimental Investigation of Ion Beam Neutralization by Coaxially Injected Electrons	*J. Am. Rocket Soc.* **32**, 929 (1962)
O. C. Yonts and R. A. Strehlow[2]	Effect of Bombardment of Titanium by Energetic Deuterium Ions	*J. Appl. Phys.* **33**, 2903 (1962)

ORNL REPORTS

Author(s)	Title	Number	Date
C. J. Barton[2] and R. A. Strehlow[2]	Blankets for Thermonuclear Reactors	ORNL-3258	6-27-62
M. W. Garrett[3]	Computer Programs Using Zonal Harmonics for Magnetic Properties of Current Systems with Special Reference to the IBM 7090	ORNL-3318	11-19-62
Joseph Lewin	"Life" Tests on Internally Water-Cooled Hollow Copper Conductors	ORNL TM-294	7-18-62

PAPERS PRESENTED AT SCIENTIFIC AND TECHNICAL MEETINGS

Annual AEC Theoretical Plasma Physics Meeting, New York, Apr. 30–May 1, 1962

T. K. Fowler, "Secondary Plasma Growth."

American Nuclear Society, Boston, June 18–21, 1962

R. J. Mackin, Jr., "Status of the DCX-2 Program."

American Physical Society, Evanston, Ill., June 19–21, 1962

Igor Alexeff, R. V. Neidigh, and E. D. Shipley, "Random Injection into a Mirror Geometry."

T. K. Fowler, "Plasma Stability and Constants of Motion."

---

[1]Instrumentation and Controls Division.

[2]Reactor Chemistry Division.

[3]Consultant, Swarthmore College

American Physical Society, Seattle, Wash., Aug. 27–29, 1962

Igor Alexeff, A. M. Veach,[4] and O. C. Yonts, "Ionic Sound Waves in an Electromagnetic Isotope Separator."

Tenth International Congress of Radiology, Montreal, Aug. 26–Sept. 1, 1962

C. C. Harris, "Collimators for Radioisotope Scanning."

Culham Study Group on Plasma Instabilities, United Kingdom Atomic Energy Research Establishment, Harwell, England, Sept. 17–22, 1962

T. K. Fowler, "Non-Linear Stability."

New England Section of the Society for Applied Spectroscopy, Boston, Oct. 9, 1962

P. M. Griffin, "The Spectroscopy of High-Temperature Plasmas."

Symposium on Space Phenomena and Measurement, Detroit, Oct. 15–17, 1962

R. J. Kerr, "Plasma Density Measurements by Molecular Beams."

---

[4]Isotopes Division.

THIS PAGE

WAS INTENTIONALLY

LEFT BLANK

ORNL-3392
UC-20 – Controlled Thermonuclear Processes
TID-4500 (18th ed.)

INTERNAL DISTRIBUTION

1. I. Alexeff
2. R. G. Alsmiller
3. W. B. Ard
4. C. F. Barnett
5. C. O. Beasley
6. M. C. Becker
7-12. P. R. Bell
13. D. S. Billington
14. E. P. Blizard
15. C. W. Blue
16. G. E. Boyd
17. R. L. Brown
18. R. E. Clausing
19. D. L. Coffey
20. F. L. Culler
21. J. S. Culver
22. S. Cuperman
23. R. A. Dandl
24. R. C. Davis
25. S. M. DeCamp
26. J. L. Dunlap
27. H. O. Eason, Jr.
28. R. S. Edwards
29. A. C. England
30. J. C. Ezell
31. J. L. Fowler
32. T. K. Fowler
33. J. E. Francis, Jr.
34. J. H. Frye, Jr.
35. W. F. Gauster
36. R. A. Gibbons
37. H. W. Graben
38. P. M. Griffin
39. W. R. Grimes
40. E. Guth
41. C. C. Harris
42. G. R. Haste
43. R. E. Hill
44. A. S. Householder
45. H. C. Hoy
46. R. P. Jernigan, Jr.
47. G. G. Kelley
48. M. T. Kelley
49. R. J. Kerr
50. R. L. Knight
51. J. A. Lane
52. C. E. Larson (K-25)
53. N. H. Lazar
54. G. F. Leichsenring
55. J. Lewin
56. R. S. Livingston
57. J. N. Luton, Jr.
58. J. R. McNally, Jr.
59. R. J. Mackin, Jr.
60. W. D. Manly
61. O. D. Matlock
62. K. Z. Morgan
63. O. B. Morgan
64. R. V. Neidigh
65. M. L. Nelson
66. J. Neufeld
67. C. E. Parker
68. W. F. Peed
69. H. Postma
70. J. F. Potts
71. M. Rankin
72. J. A. Ray
73. R. G. Reinhardt
74. P. W. Rueff
75. W. K. Russell
76. H. E. Seagren
77. Y. Shima
78. E. D. Shipley
79. M. R. Skidmore
80. M. J. Skinner
81-90. A. H. Snell
91. W. L. Stirling
92. R. F. Stratton, Jr.
93. R. A. Strehlow
94. J. A. Swartout
95. E. H. Taylor
96. P. A. Thompson
97. R. M. Warner
98. H. L. Watts
99. A. M. Weinberg
100. E. R. Wells
101. T. A. Welton
102. G. K. Werner
103. W. L. Wright
104. A. J. Wyrick
105. O. C. Yonts
106. W. P. Allis (consultant)

107. W. H. Bostick (consultant)
108. F. E. Dunnam (consultant)
109. J. W. Flowers (consultant)
110. M. W. Garrett (consultant)
111. E. G. Harris (consultant)
112. D. E. Harrison (consultant)
113. W. Heckrotte (consultant)
114. R. Hefferlin (consultant)
115. G. W. Hoffman (consultant)
116. V. W. Hughes (consultant)
117. R. K. Jaggi (consultant)
118. D. W. Kerst (consultant)
119. E. W. McDaniel (consultant)
120. M. R. C. McDowell (consultant)
121. D. R. Montgomery (consultant)
122. J. E. Mott (consultant)
123. C. E. Nielsen (consultant)
124. W. B. Pardo (consultant)
125. J. M. Reynolds (consultant)
126. F. F. Rieke (consultant)
127. H. S. Robertson (consultant)
128. D. J. Rose (consultant)
129. L. P. Smith (consultant)
130. P. M. Stier (consultant)
131. C. H. Weaver (consultant)
132. J. D. Tillman (consultant)
133-162. Thermonuclear Division Library
163. Reactor Division Library
164. Biology Library
165-166. Central Research Library
167. Laboratory Shift Supervisor
168-192. Laboratory Records Department
193. Laboratory Records, ORNL RC
194-195. ORNL – Y-12 Technical Library Document Reference Section

EXTERNAL DISTRIBUTION

196. S. C. Brown, Massachusetts Institute of Technology
197. M. B. Gottlieb, Princeton University
198. H. Grad, New York University
199. J. M. B. Kellogg, Los Alamos Scientific Laboratory
200. A. C. Kolb, Naval Research Laboratory
201. J. A. Phillips, Los Alamos Scientific Laboratory
202. R. F. Post, University of California, Lawrence Radiation Laboratory
203. A. Simon, General Atomic, San Diego, California
204. L. Spitzer, Princeton University
205. E. Teller, University of California, Lawrence Radiation Laboratory
206. C. M. Van Atta, University of California, Lawrence Radiation Laboratory
207. R. W. McNamee, Union Carbide Corporation
208-209. Research and Development Division, AEC, ORO (1 copy each to H. M. Roth and R. B. Martin)
210-211. Controlled Thermonuclear Branch, AEC, Washington (A. E. Ruark)
212. L. D. Smullin, Massachusetts Institute of Technology
213-816. Given distribution as shown in TID-4500 (18th ed.) under Controlled Thermonuclear Processes category (75 copies – OTS)